University of Alberta

A Study of Hydrogen Enrichment at Pits and Other Surface Discontinuities in Mild Steel and the Contribution to Near-Neutral pH Stress Corrosion Cracking

by

Laura Wall

A thesis submitted to the Faculty of Graduate Studies and Research in partial fulfillment of the requirements for the degree of Master of Science

in

Materials Engineering

Department of Chemical and Materials Engineering

Edmonton, Alberta

Spring 2007

Library and Archives Canada

Published Heritage Branch

395 Wellington Street
Ottawa ON K1A 0N4
Canada

Bibliothèque et Archives Canada

Direction du Patrimoine de l'édition

395, rue Wellington
Ottawa ON K1A 0N4
Canada

Your file Votre référence
ISBN: 978-0-494-30036-7
Our file Notre référence
ISBN: 978-0-494-30036-7

NOTICE:
The author has granted a non-exclusive license allowing Library and Archives Canada to reproduce, publish, archive, preserve, conserve, communicate to the public by telecommunication or on the Internet, loan, distribute and sell theses worldwide, for commercial or non-commercial purposes, in microform, paper, electronic and/or any other formats.

The author retains copyright ownership and moral rights in this thesis. Neither the thesis nor substantial extracts from it may be printed or otherwise reproduced without the author's permission.

AVIS:
L'auteur a accordé une licence non exclusive permettant à la Bibliothèque et Archives Canada de reproduire, publier, archiver, sauvegarder, conserver, transmettre au public par télécommunication ou par l'Internet, prêter, distribuer et vendre des thèses partout dans le monde, à des fins commerciales ou autres, sur support microforme, papier, électronique et/ou autres formats.

L'auteur conserve la propriété du droit d'auteur et des droits moraux qui protège cette thèse. Ni la thèse ni des extraits substantiels de celle-ci ne doivent être imprimés ou autrement reproduits sans son autorisation.

In compliance with the Canadian Privacy Act some supporting forms may have been removed from this thesis.

While these forms may be included in the document page count, their removal does not represent any loss of content from the thesis.

Conformément à la loi canadienne sur la protection de la vie privée, quelques formulaires secondaires ont été enlevés de cette thèse.

Bien que ces formulaires aient inclus dans la pagination, il n'y aura aucun contenu manquant.

Canada

Dedicated in memory of the fourteen women
killed at École Polytechnique on December 6, 1989 and
in honour of their spirit and dedication to their chosen fields.

Geneviève Bergeron

Hélène Colgan

Nathalie Croteau

Barbara Daigneault

Anne-Marie Edward

Maud Haviernick

Maryse Laganière

Maryse Leclair

Anne-Marie Lemay

Sonia Pelletier

Michèle Richard

Annie St-Arneault

Annie Turcotte

Barbara Klucznik-Widajewicz

ABSTRACT

The role of hydrogen in the initiation of near-neutral pH stress corrosion cracks was studied. Hydrogen content was measured for X-52 steel in various conditions. The effect of elevated hydrogen concentrations on room temperature creep behaviour of X-52 pipeline steel was investigated experimentally. Extensive finite element modelling of the concentrations and locations of hydrogen around corrosion pits on pressurized line pipe in near-neutral pH solution was completed. The effects of stress and geometry on equilibrium hydrogen concentration were studied. A material model simulating the effects of hydrogen enhanced localized plasticity was used to investigate the role of hydrogen in crack initiation. Throughout the modelling, two distinct hydrogen trapping models were used and compared. In steels, the majority of hydrogen is found to reside in traps at cementite interfaces and grain boundaries, yet related work has found that NNpHSCC proceeds transgranularly through ferrite. Implications for understanding NNpHSCC crack initiation are discussed.

ACKNOWLEDGEMENT

I am sincerely grateful to Dr. Reg Eadie and Dr. Weixing Chen for their supervision, guidance and encouragement throughout the course of my thesis work. I admire their passion for research, outstanding technical knowledge and excellent motivational skills. Their acknowledgment of my goals in undertaking this project and the overarching support of Dr. Eadie have been essential.

Other members of the NNpHSCC research group during my time at the University of Alberta have provided helpful discussion and practical assistance. I would like to thank my colleagues Bingyan Fang, John Hiebert, Feng Wang and Haishan Wang.

I would like to thank professors Jingli Luo and Walid Moussa both of whom I have drawn upon for help with my research.

The technical support and advice provided by Bob Scott, Tina Barker, James Mckinnon and Walter Boddez during the completion of this project has been valued.

I am grateful for the financial support provided by the University of Alberta, NSERC, INCO and the Canadian Engineering Memorial Foundation for this research.

TABLE OF CONTENTS

1. INTRODUCTION 1

2. LITERATURE REVIEW 2

2.1. Brief History and Significance of SCC 2

2.2. General Overview of Near-Neutral pH SCC 3

2.2.1. Distinction from High pH SCC 7
2.2.2. Environmental Factors affecting Near-Neutral pH SCC 8
2.2.3. Stressing Factors affecting Near-Neutral pH SCC 24
2.2.4. Metallurgical Factors affecting Near-Neutral pH SCC 37
2.2.5. Mechanisms of Near-Neutral pH SCC 45
2.2.6. Near-Neutral pH SCC Investigation Methods 64

2.3. Pits and Crack Initiation 69

2.3.1. Pits as Crack Initiation Sites 69
2.3.2. Existing Criteria for Pit-to-Crack Transitions 70
2.3.3. The Role of Stress in Crack Initiation 70
2.3.4. The Role of Hydrogen in Crack Initiation 72

2.4. Description of Equilibrium Hydrogen Concentration Model 79

2.4.1. Unstressed Lattice Hydrogen Concentration 80
2.4.2. Lattice Hydrogen as a Function of Stress 83
2.4.3. Hydrogen Trapping 85

2.5. Motivation for research 90

3. MODELLING AND EXPERIMENTAL METHODS 91

3.1. Description of Finite Element Model 91

3.1.1. Three Dimensional Geometries 91
3.1.2. Two Dimensional Geometries 93
3.1.3. Mesh Convergence 94
3.1.4. Material Properties 96
3.1.5. Stresses Applied 102
3.1.6. Coupling of Hydrogen Concentrations and Material Softening 102

3.2. Constant Load Extension Test Methods 105

3.3. Hydrogen Content Determination Test Methods 107

3.3.1. "Air" samples 107
3.3.2. "C2" samples 107
3.3.3. "C2 plus poison" samples 107
3.3.4. "C2, no stress" samples 108
3.3.5. "C2, no stress, previous strain" samples 108

3.3.6. LECO RH-402 operation 109

4. CONSTANT LOAD EXTENSION TEST RESULTS 112

5. HYDROGEN CONTENT DETERMINATION RESULTS 114

6. FINITE ELEMENT MODEL RESULTS 116

6.1. Initial Hydrogen Concentration 116

6.1.1. Effect of C_L° Using Pure Iron Trap Densities 116
6.1.2. Effect of C_L° Using Pipeline Steel Trap Densities 117

6.2. Uniaxial vs. Biaxial Loading 119

6.3. Sensitivity to Pit Geometry 123

6.3.1. Three Dimensional Geometries 123
6.3.2. Two Dimensional Geometries 125
6.3.3. Comparison of Semi-circular Notch and Hemispherical Pit 129

6.4. Hydrogen Concentrations in Model 130

6.4.1. Hydrogen Concentrations without HELP 130
6.4.2. Use of Hydrogen-Dependent HELP Material Property Model 133

6.5. Cyclic Loading and Trap Density Effects 137

7. DISCUSSION 140

7.1. Constant Load Extension 140

7.2. Hydrogen Content Determination 140

7.3. Finite Element Model 146

7.3.1. Uniaxial vs. Biaxial Loading 146
7.3.2. Sensitivity to Pit Geometry 148
7.3.3. Hydrogen Concentrations in Model 151
7.3.4. Cyclic Loading and Trap Density Effects 156
7.3.5. Application of Model to Actual Pits 157

7.4. Implications for Crack Initiation 162

8. CONCLUSIONS 165

8.1. Main Conclusions 165

8.2. Suggestions for Future Work 168

8.2.1. Localized Hydrogen Dependent Stress-Strain Behaviour 168
8.2.2. Pipeline Steel Trap Densities 169
8.2.3. 3D Modelling with Systematic Variations in Pit Geometry 169

9. REFERENCES 170

APPENDIX A 183

APPENDIX B 185

LIST OF TABLES

Table 1 – Colonies of NNpHSCC Detected on Canadian Pipelines, August 2000 [Source: CEPA 2000] 4

Table 2 – Sources of Circumferential and Longitudinal Stresses in Gas and Liquids Pipelines 5

Table 3 – Comparison of Near-Neutral and High-pH SCC 8

Table 4 – Compositions of common near-neutral pH test solutions 14

Table 5 – Dormancy of Sparse and Dense Crack Colonies 47

Table 6 – Common Mechanical and Electrochemical NNpHSCC Laboratory Test Techniques 66

Table 7 – Summary of tests giving unstressed lattice hydrogen concentrations . 82

Table 8 – Mean Number of Hydrogen Traps (10^{25} / m^3) with Standard Deviation in Brackets for Three Pipeline Steels Exposed to NS4 Solution at Different pH [Source: Parkins and Beavers 2003] 89

Table 9 – Chemical composition (wt%) of X-52 pipeline steel 96

Table 10 – Stress - strain data used for X-52 in finite element model 98

Table 11 – Stress - strain data for hydrogen dependent material properties, 0.5 softening parameter 101

Table 12 – Thermal conductivity of gases at STP 109

Table 13 – Samples tested in LECO RH-402 hydrogen analyzer 112

Table 14 – Mechanical properties of tested X-52 steel 112

Table 15 – Results of Hydrogen Content Tests using LECO RH-402 Hydrogen Analyzer 115

Table 16 – Average and local maximum stresses for uniaxial and biaxial loading 122

Table 17 – Stress and strain results for two dimensional notch finite element models 126

Table 18 – Stress and strain results for 2D and 3D models of a hemispherical pit under 100% SMYS uniaxial loading 129

Table 19 – Hydrogen concentrations in models without HELP effects 131

Table 20 – Finite element models using hydrogen dependent material properties 133

Table 21 – Hydrogen concentrations in models with HELP effects 134

Table 22 – Hydrogen concentrations with trap density multiplication 138

Table 23 – Changes in maximum stresses and strains due to the use of hypothetical hydrogen-dependent material properties 154

LIST OF FIGURES

Figure 1 - Tenting of polyethylene tape coating [Source: Baker 2005] 9

Figure 2- Stress-strain curves of X-52 in air and at different values of imposed electrochemical potential in NS4 solution [Source: Delafosse and Magnin 2001] 18

Figure 3 - The effect of hydrogen pre-charging and solution exposure on SSRT stress-strain curves for X-52 steel tested at 1x10-6 / sec in air and in NS4 [Source: Yu, 1997] 19

Figure 4 - "Bathtub" model of four stage crack growth process [Source: Baker 2005] 45

Figure 5 - Crack in a near-neutral pH SCC colony that developed in service on a liquid pipeline 70

Figure 6 - Schematic of stress corrosion crack initiation from hydrogen ingress at a surface defect [Source: Delafosse and Magnin, 2001] 73

Figure 7 – Replicas showing (a) dimples formed at high K (stress intensity factor) and (b) intergranular tear ridges formed at low K on fracture surface of 0.28% C steel specimen. [Source: Beachem 1972] 76

Figure 8 - Hydrogen concentrations for X-52 in NS4 as a function of potential and pH [Source: Parkins and Beavers 2003] 81

Figure 9 – Unstressed lattice hydrogen concentrations in pipeline steels 82

Figure 10 - Trap Density and Equivalent Plastic Strain for Pure Iron [Source: Sofronis and McMeeking 1989] 87

Figure 11 - Equations to determine lattice and trapped hydrogen concentrations from hydrostatic stresses and plastic strains 90

Figure 12 - Maximum hydrostatic stress near pit as a function of pit size 92

Figure 13 - Orientation of quarter-pit model with pit base dissolution 93

Figure 14 – Categories of notch geometries used in two dimensional analysis ... 94

Figure 15 - Convergence of stress results with mesh refinement 95

Figure 16 - Change in stress results from previous to current mesh refinement step 95

Figure 17 - Stress-strain curves for X-52 in air 97

Figure 18 - Engineering and true stress - strain curves used for X-52 in finite element model 98

Figure 19 - Hydrogen dependent material properties, 0.5 softening parameter . 101

Figure 20 - Iterative analysis of coupled hydrogen concentration and hydrogen enhanced localized plasticity problem 105

Figure 21 - Dimensions of cylindrical samples used for constant load extension tests 106
Figure 22 - Flow chart of hydrogen analyzer operation 110
Figure 23 - Estimate of hydrogen diffusion distance possible while transferring specimen from test solution to liquid nitrogen 111
Figure 24 - Results of tensile tests on cylindrical X-52 samples 113
Figure 25- Strain vs. time for constant load tests in air and in C2 solution 114
Figure 26 - Creep strains for constant load tests in air and in C2 solution 114
Figure 27 – Effect of initial hydrogen concentration on resulting calculated trapped and lattice hydrogen concentrations (pure iron trapping model) 117
Figure 28 – Effect of initial hydrogen concentration on resulting calculated trapped and lattice hydrogen concentrations (pipeline steel trapping model) 118
Figure 29 - Hydrostatic stresses from biaxial loading for pits: 124
Figure 30 - Comparison of stresses resulting from uniaxial and biaxial loading for various geometries without any modelling of effects of hydrogen... 125
Figure 31 - Linear relationship between maximum equivalent plastic strain and 2D notch depth 127
Figure 32 - Relationship between maximum hydrostatic stress and 2D notch depth 127
Figure 33 - Relationship between maximum von Mises stress and 2D notch depth 128
Figure 34 - Power relationship between maximum equivalent plastic strain and notch tip radius 128
Figure 35 - Quadratic relationships between maximum stresses and notch tip radius 129
Figure 36 – Contributions of lattice and trapped hydrogen to maximum local concentration, using pure iron trap density model 132
Figure 37 – Contributions of lattice and trapped hydrogen to maximum local concentration, using pipeline steel trap density value 132
Figure 38 – Comparison of maximum stresses in hemispherical and base dissolution models, with and without hydrogen dependent material property model 135
Figure 39 – Comparison of maximum strains in hemispherical and base dissolution models, with and without hydrogen dependent material property model 136

Figure 40 – Stress profiles (a,b) and temperature profile (c) used in the application of a hydrogen-dependent material property model and the resulting stress profiles (d, e) 137

Figure 41 – Total hydrogen concentrations for (a) original trap density formula (b) maximum trap densities multiplied by ten (c) maximum trap densities multiplied by thirty 139

Figure 42 – Measured Hydrogen Concentrations in Five Types of Test Samples 141

Figure 43 – Average and Range of Measured Hydrogen Concentrations in Five Types of Test Samples 142

Figure 44 – Comparison of Measured Hydrogen Concentrations in Previously Stressed Samples Stored in Liquid Nitrogen or Allowed to Reach Room Temperature 143

Figure 45 – Comparison of unstressed hydrogen concentrations reported in the literature to the present hydrogen determination results 145

Figure 46 – Decrease in fractional trap occupancy at high temperature for both dislocation traps and carbide interface traps 152

Figure 47 – Maximum lattice and trapped hydrogen concentrations as a function of trap density 153

Figure 48 – Hydrostatic stress contour plot for hemispherical pit under uniaxial loading with no hydrogen dependence of stress-strain behaviour 155

Figure 49– Pit-to crack transition on X-52 tensile sample in near-neutral solution 158

Figure 50 – Points used in the creation of a two-dimensional finite element model of actual corrosion pit 159

Figure 51 – Von Mises stress contour plot for two-dimensional model of actual pit, with tensile load of 60% SMYS 159

Figure 52 – Total strain contour plot for two-dimensional model of actual pit, with tensile load of 60% SMYS 160

Figure 53 – Surface of an X-52 sample, previously polished as for metallography without etching, then exposed to NS4 solution with pH = 6.3 for 3 days, x1000 [Source: Parkins and Beavers 2003] 164

LIST OF SYMBOLS, NOMENCLATURE AND ABBREVIATIONS

α	number of hydrogen atoms occupying a trap site
β	number of available interstitial lattice sites per solvent atom
δ	crack tip opening displacement
ε_o	yield strain in the absence of hydrogen
ε_p	plastic strain
$\varepsilon_{p,eq}$	equivalent plastic strain
$\varepsilon_{p\ max}$	maximum plastic strain
ε^P	true strain under uniaxial tension
θ_L	fractional occupancy of interstitial lattice sites
θ_T	fractional occupancy of trap sites
μ_L	chemical potential of hydrogen in iron
μ_L^o	chemical potential of hydrogen in iron at reference temperature and pressure
ξ	hydrogen induced softening parameter
ρ	notch tip radius
$\Delta\sigma$	stress amplitude
σ	stress
σ_1	first principal stress
σ_2	second principal stress
σ_3	third principal stress
σ_h	hydrostatic stress
σ_{max}	maximum stress
σ_{min}	minimum stress
$\sigma_o(C)$	yield stress in the presence of hydrogen
$\sigma_o(0)$	yield stress in the absence of hydrogen
σ_{vm}	von Mises stress
σ_{ys}	yield strength
a	crack length
APB	acid producing bacteria
API	American Petroleum Institute

B	fracture toughness specimen thickness
bcc	body centered cubic
C	total hydrogen concentration
C2	a laboratory electrolyte for NNpHSCC studies
CANMET-MTL	Canada Centre for Mineral and Energy Technology - Materials Technology Laboratory
CEPA	Canadian Energy Pipeline Association
CERT	constant extension rate test
C_f	crack propagation fatigue coefficient
CGHAZ	coarse grained heat affected zone
C_L	concentration of hydrogen in interstitial lattice sites
C_L^o	unstressed lattice hydrogen concentration
C_L^σ	concentration of hydrogen in interstitial lattice sites under hydrostatic stress
CP	cathodic protection
CR	controlled rolling
CSA	Canadian Standards Association
CT	compact tensile
C_T	concentration of hydrogen in trap sites
CTOD	crack tip opening displacement
D	diffusion coefficient for solute
da/dN	crack growth rate with respect to loading cycles
da/dt	crack growth rate with respect to time
D_b	effective diffusion coefficient
DCPD	direct current potential drop
D_L	lattice diffusion coefficient
d_n	constant relating $d\delta/dt$ and $\Delta J/\Delta t$
DSAW	double submerged-arc weld
E	Young's modulus
EAC	environmentally assisted cracking
E_{corr}	corrosion potential

ERW	electric-resistance weld
F	Faraday's constant
f	frequency
f(a/w)	crack geometry factor
fcc	face centered cubic
HAZ	heat affected zone
ΔH_B	trap binding energy
hcp	hexagonal close packed
HE	hydrogen embrittlement
HEDE	hydrogen enhanced decohesion
HELP	hydrogen enhanced localized plasticity
HIC	hydrogen induced cracking
i_{corr}	corrosion current density
IGSCC	intergranular stress corrosion cracking
J	J-integral, work required to grow a unit area of crack
J_{el}	elastic component of J-integral
J_{pl}	plastic component of J-integral
ΔK	stress intensity factor range
K	stress intensity factor
K_θ	equilibrium constant for lattice and trap occupancies
K_{ISCC}	threshold stress intensity factor
K_{max}	maximum stress intensity factor
m	crack propagation fatigue exponent
N	work hardening exponent
n	valence of the metal ions produced from dissolution
N_A	Avogadro's number
NEB	National Energy Board
N_L	number of lattice sites per unit volume
NNpHSCC	near-neutral pH stress corrosion cracking
NOVATW	NOVA trapped water, a laboratory electrolyte
NS4	a common laboratory electrolyte for NNpHSCC studies

OCP	open circuit potential
PE	polyethylene
QT	quenched and tempered
%RA	percent reduction in area
R	universal gas constant
R.T.	room temperature
SCC	stress corrosion cracking
SCE	saturated calomel electrode
SEM	scanning electron microscope
SMYS	specified minimum yield strength
SRB	sulfate reducing bacteria
SSRT	slow strain rate test
STP	standard temperature and pressure
T	absolute temperature
t	time
TCPL	TransCanada PipeLines
TEM	transmission electron microscope
TGSCC	transgranular stress corrosion cracking
TMCP	thermomechanical-controlled processing
TTT	tapered tensile test
U	energy under load-displacement curve
v	displacement of applied force on fracture toughness specimen
V_H	partial molar volume of hydrogen
V_M	molar volume of lattice
WOL	wedge-opening load
x	distance over which solute diffuses
y	maximum out-of-alignment distance between cracks that will allow for coalescence
YS	yield strength

1. INTRODUCTION

Near-neutral pH stress corrosion cracking (NNpHSCC) was first encountered on Canadian pipelines in 1982. Today, it still poses a significant threat to steel pipelines in Canada, the United States and other countries around the world. While pipeline integrity management programs have significantly reduced the incidence of leaks or ruptures due to NNpHSCC (Parkins 1994), there remains much technical uncertainty surrounding the causes and prediction of this form of cracking. A 2005 report by Michael Baker Jr. Inc., which was commissioned by the Department of Transportation, Office of Pipeline Safety in the United States reviews the available information related to stress corrosion cracking and states that much technical uncertainty remains with respect to the causal factors and mechanisms involved in SCC. (Baker 2005)

NNpHSCC requires the simultaneous existence of a potent cracking environment, a susceptible pipe surface, and a sustained tensile stress. (NEB 1996) It is generally agreed that NNpHSCC occurs by the combined actions of anodic dissolution and hydrogen attack. Both of these mechanisms require the contact of a solution, typically groundwater, with the surface of the pipe. Evidence of dissolution consists primarily of corrosion on the crack walls and corrosion products within the crack. The involvement of hydrogen in the cracking process is evidenced by quasi-cleavage on the crack faces near the tip, before corrosion has an opportunity to obscure these features.

The propagation of existing near-neutral pH stress corrosion cracks has been extensively studied and a general understanding of this process is beginning to develop. Much less is currently known about the initiation and very early growth of these cracks. The role of hydrogen may be critical in the initiation of NNpHSCC. For more than a century, it has been known that hydrogen reduces the toughness and bulk ductility of steels, an effect commonly called hydrogen embrittlement (HE). (Oriani 1970, Beachem 1972) Hydrogen embrittlement has

received intense study over several decades, (Troiano 1960; Oriani 1970; Johnson and Lin 1981; Hirth 1980; Tyson 1979) but is still not well understood. The present work seeks to investigate the possibility that hydrogen-induced changes to mechanical properties of line pipe steels have a significant effect on the initiation of stress corrosion cracks which are frequently observed at surface corrosion pits.

In this thesis, a literature review is provided to describe the history, characteristics and proposed mechanisms of near-neutral pH stress corrosion cracking. This section is followed by the details of a finite element model constructed to study the proposed crack initiation event and the experimental methods for two test programs that were carried out. The results of the constant load extension tests, the hydrogen content determination tests and the finite element model are given in that order, and are followed by discussion of these results and the connections between them. The thesis closes with conclusions from this work and suggestions for future work.

2. LITERATURE REVIEW

2.1. Brief History and Significance of SCC

The first pipeline failures due to NNpHSCC were recognized in 1985. In that year, three ruptures occurred on pipelines in Ontario operated by TransCanada Pipelines (TCPL). Examination of these failed pipe sections indicated that the failures had been the result of stress corrosion cracking (SCC). This SCC exhibited different characteristics than the typical high-pH SCC that had been studied since the 1960s. This new form of SCC was called near-neutral pH stress corrosion cracking. It was later determined that NNpHSCC had been detected on other pipelines during the 1970s and had been responsible for a failure on a NOVA operated pipeline in 1975. (NEB 1996)

In response to the failures in 1985, TCPL introduced a program of improved inspection and detection methods combined with research into the initiation and

growth of NNpHSCC. Four further pipeline ruptures between 1991 and 1993 led the National Energy Board (NEB) to conduct an inquiry into stress corrosion cracking in early 1993. The result of this inquiry was the general conclusion that the problem of NNpHSCC was being managed appropriately by pipeline operating companies. (Baker 2005) However, another four pipeline ruptures occurred in 1994 and 1995, drawing more attention and concern to the issue of pipeline safety. A much wider ranging public inquiry into NNpHSCC was initiated by the NEB in 1995. This inquiry involved input from pipeline operators, research scientists and experts, industry associations and people living near pipelines. In 1996, the NEB published *Report of the Inquiry: Stress Corrosion Cracking on Canadian Oil and Gas Pipelines*. Even a decade later, this document remains one of the most comprehensive and readable documents addressing this topic. It offered 27 recommendations to prevent pipeline leaks or ruptures, and required that every pipeline company under NEB jurisdiction develop and implement an SCC management program by June 1997.

The cost of pipeline integrity management programs intended to prevent SCC-related failures is significant. Between 1985 and 1996, even before such a program was a regulated requirement, TransCanada Pipelines alone spent $202 million on its SCC management program (NEB 1996)

2.2. General Overview of Near-Neutral pH SCC

Near-neutral pH stress corrosion cracking (NNpHSCC) is the less common form of SCC. It has only been recognized as a threat to pipeline integrity in the last two decades. First found in Canada in 1982, NNpHSCC has also been found in France (LeFriant et al. 1999), Italy (Arrigoni and Sinigaglia 1997) and Russia (Ott et al. 1992; Surkov et al. 1994)

Many kilometers of Canadian pipelines are susceptible to near-neutral pH stress corrosion cracking. As of 2005, more than 750,000 kilometers of pipelines in Canada were subject to the requirements of Canadian Standards Association

standard *CSA Z662-03 Oil and Gas Pipeline Systems*. (Baker 2005) These pipelines range in size from 1-inch diameter plastic gas distribution lines to 48-inch oil and gas transmission pipelines. TCPL's natural gas pipeline system consists of more than 11,000 kilometers of large-diameter pipe. (Delanty and O'Beirne 1992)

Between 1977 and 1996, SCC has caused 12 ruptures and 10 leaks on Canadian natural gas and liquids pipelines. (NEB 1996) Most SCC failures have occurred on pipes that have been in service for more than ten years, with no failures having occurred on pipes that are less than five years old. (Parkins 1996B) In the United States, SCC failures occur more frequently on natural gas pipelines than on hazardous liquid pipelines. (Baker 2005)

The severity of an SCC colony is described by the maximum crack depth, the maximum crack length, the average colony size and the number or colonies detected on a section of pipe. (Delanty and O'Beirne 1992) Table 1 summarizes the SCC inspection data in the Canadian Energy Pipeline Association (CEPA) SCC Database as given in the Trending Report of August 2000. (CEPA 2000) While many colonies of SCC have been found during inspection of oil and gas pipelines, the large majority of these colonies are either dormant or are tending towards a stage of dormancy when they are found. Only a small percentage of these colonies continue to grow to a stage in which they would pose a threat to pipeline integrity.

Table 1 – Colonies of NNpHSCC Detected on Canadian Pipelines, August 2000 [Source: CEPA 2000]

Fluid	Length Inspected (m)	No. of SCC Colonies Detected
Gas	125,855	17,925
Liquid	20,532	366
Total	146,387	18,291

Three conditions must exist simultaneously in order for SCC to develop: a potent environment, a susceptible pipe surface, and a sustained tensile stress. Thus, the

controlling parameters for SCC are electrochemical, mechanical and metallurgical. (Parkins and Fessler 1986)

Stress corrosion cracks occur in an orientation perpendicular to the maximum principal stress in the material. Pipelines experience both longitudinal and circumferential stresses. Typically, the circumferential stresses dominate, giving longitudinal cracking. In some cases, high longitudinal (axial) stresses have caused the occurrence of circumferential NNpHSCC. (Arrigoni and Sinigaglia 1997) Sources of circumferential and longitudinal stresses are listed in Table 2, adapted from the 1996 NEB Report of the Inquiry.

Table 2 – Sources of Circumferential and Longitudinal Stresses in Gas and Liquids Pipelines

Sources of circumferential stresses	Sources of longitudinal stresses
Hoop stress due to internal operating pressure	Longitudinal stress due to internal pressure (½ to ⅓ of hoop stress)
Bending stress when an out-of-round pipe is subjected to internal pressure	Bending stresses from soil settlement or landslides
Thermal stresses from temperature differences through wall thickness	Thermal stresses from temperature differences along pipe axial direction
Local stresses at gouges, weld toes, corrosion pits and other stress concentrations	
Residual stress from pipe manufacture	

The maximum operating stress permitted in pipeline walls is governed by CSA Z662 standard and classified as Class 1, 2, or 3. Class 1 locations are in areas with zero or low population density, and pipe hoop stresses in these regions are not to exceed 80% of the line pipe specified minimum yield strength (SMYS). Class 2 and 3 locations are more densely populated or are near environmentally sensitive areas. In these regions, more people would be affected by pipeline safety risks, and the allowable pipe stress is lower. This condition of lower allowable

stresses is generally met by using a pipe with a thicker wall, which also increases the critical crack size that will lead to a leak or rupture. (Delanty and O'Beirne 1992) In response to three in-service line failures in 1986 on TCPL line, a six-year study of NNpHSCC was conducted by Delanty and O'Beirne (1992). In this work it was found that all failures in service or during hydrotesting that took place during the study had occurred in Class 1 locations where operating pressures are highest and the surrounding population density is low.

For high-pH SCC environments, a static tensile stress can lead to the initiation and propagation of cracks, but for NNpHSCC, laboratory experience has demonstrated that a cyclic component to the tensile stress is needed for cracking to occur. (Parkins 1998A)

This requirement of a fluctuating tensile stress for the development and growth of SCC raises the question of the difference between NNpHSCC and corrosion fatigue. The classical definition is that SCC occurs under tension loads while corrosion fatigue occurs under cyclic loading, but this distinction was made in relation to high-pH SCC. In the case of NNpHSCC, research is beginning to support the theory that corrosion fatigue may actually be a driving mechanism of crack growth. Appendix A of the Baker Report, published in 2005 to outline the current state of knowledge with respect to near-neutral pH SCC, indicates several research areas where the difference between corrosion fatigue and NNpHSCC was difficult to distinguish. (Baker 2005)

The complexity of near-neutral pH stress corrosion cracking is reflected in the diversity and the inter-relation of parameters that are understood to influence its development. Furthermore, the difficulties that researchers have encountered in obtaining field-relevant reproducible data underscore the complexity of the problem and the need for a better understanding of its underlying causes and mechanisms. (Beavers and Harle 1996; Leis and Colwell 1997)

2.2.1. Distinction from High pH SCC

The conditions under which NNpHSCC and high-pH SCC develop are markedly different. High-pH SCC occurs in carbonate-bicarbonate groundwater solutions with pH between 8 and 11. The solution may develop as a result of interaction between hydroxyl ions (produced by cathodic polarization) and CO_2 in the soil. In contrast, as described above, NNpHSCC occurs in dilute groundwater with dissolved CO_2, with a pH between 5.5 and 7. Effective cathodic protection prevents the development of this type of environment. One of the reasons that high pH SCC is more common than NNpHSCC is because most pipelines are exposed to effective cathodic protection. (Parkins 1998A)

High pH SCC typically develops at service temperatures above 100°F, while no correlation between temperature and NNpHSCC has been established.

Near-neutral pH stress corrosion cracks are wider than high-pH stress corrosion cracks, due to the corrosion of the side faces of the crack that occurs in near-neutral conditions and the passivation of the crack flanks that is typically observed in high-pH SCC. The main corrosion product formed in high-pH SCC is magnetite (a dark and dense oxidized material that occupies roughly seven times more volume than the metal from which it forms) while that for NNpHSCC is iron carbonate (a white porous product that does not form a barrier between the metal surface and the surrounding environment). The mouths of high-pH SCC cracks generally have a dark coating of oxidized material while the last portion of the wall to crack has a shiny silver colour.

High-pH SCC is also referred to sometimes as intergranular SCC (IGSCC), while NNpHSCC can be called transgranular SCC (TGSCC). IGSCC follows a path along grain boundaries and small branches develop off of the main crack path, while TGSCC usually propagates in a relatively straight line, directly through grains and their boundaries.

The appearances of the fracture surfaces for both types of SCC are similar, but the morphology implies that different fracture mechanisms are responsible. A threshold stress exists for high-pH SCC but has not been established for NNpHSCC. (Baker 2005) Below this high-pH SCC threshold stress level, cracks will not initiate or grow to a size that could cause failure.

Table 3 – Comparison of Near-Neutral and High-pH SCC

Near-Neutral pH SCC	Both	High pH SCC
-pH 5.5-7.5 -Wider cracks with side wall corrosion -cathodic protection (CP) not reaching metal -Higher chance of SCC near longitudinal weld	-Colonies of multiple cracks aligned perpendicular to stress -Tend to coalesce, can reach critical depth/length and cause rupture	-Temperature sensitivity -pH 8-11 -Narrower, sharper cracks -CP reaching metal -Higher chance of SCC on bottom half of pipe - SCC not more frequent near weld

Adapted from: (Baker 2005, Parkins 1996B)

The concentrated carbonate-bicarbonate electrolyte associated with high pH SCC has been found during excavations of TCPL lines, but no SCC or pitting was been found in these locations. (Delanty and O'Beirne 1992)

The lower potential ranges for near neutral than high pH SCC implies that different cracking mechanisms are operating in the two cases, and thus that a discontinuity exists between the two forms of cracking. (Parkins 2000)

2.2.2. Environmental Factors affecting Near-Neutral pH SCC

Environmental parameters known to influence stress corrosion cracking include: contact between metal and groundwater, pipe internal pressure, solute species and concentrations, electrolyte pH, electrochemical potential, solution viscosity, and stirring or mixing. (Jones and Ricker 1992)

2.2.2.1. Coatings

A number of different types of pipe coating systems have been used on pipelines installed in Canada. The purpose of coating a pipe before it is buried is to isolate the exterior surface of the steel from the groundwater environment.

Polyethylene (PE) tape is a coating that is wrapped around the pipe. It can be applied either in the mill or in the field and was the most common coating type on Canadian pipelines installed between the early 1960s and the early 1980s. Most Canadian NNpHSCC failures have occurred on PE tape wrapped pipelines that were installed between 1968 and 1973. (NEB 1996) Tape tenting can occur in the area near the longitudinal weld and this area can serve as a trap for groundwater next to the pipe surface. Figure 1 illustrates how PE tape tenting occurs. When the adhesive holding the tape to the pipe fails, the PE tape can disbond, allowing the surrounding environment to contact the pipe. Disbonded PE tape shields the pipe surface from any applied cathodic protection, rendering the protection ineffective in preventing NNpHSCC. Near neutral-pH stress corrosion cracks are often observed to be concentrated along tape tenting regions near longitudinal weld toes. (Parkins 1996B)

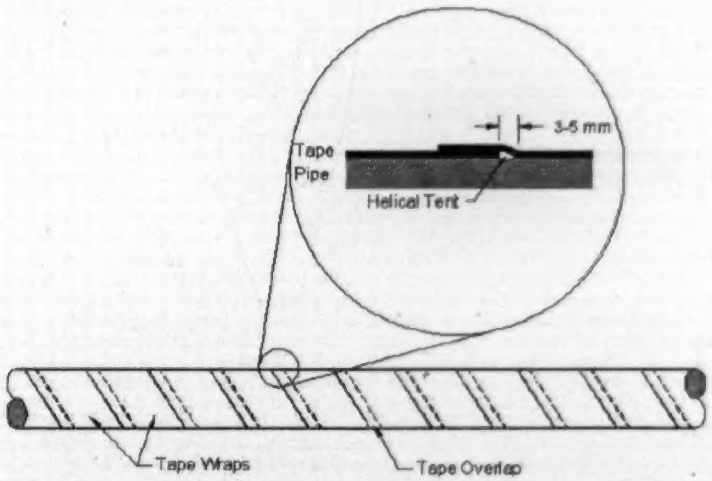

Figure 1 - Tenting of polyethylene tape coating [Source: Baker 2005]

Since the mid 1980s, the system of tape-wrapped coatings has been improved so that the tapes are less likely to disbond, and in the case of disbondment, the tape separates from the adhesive so that the adhesive continues to protect the pipe surface. (NEB 1996)

Coal tar and asphalt coatings were used mainly during the 1950s and 60s. They are typically applied to pipes in the field over the ditch, and minimal surface preparation was done before the application of the coating. Thus, millscale and corrosion products are frequently found on pipe surfaces under coal tar and asphalt coatings. These coatings can disbond from the pipe surface, but are not electrically shielding. NNpHSCC develops under failed coal tar and asphalt coatings mainly in very dry terrains in which the soil has a high resistivity and cathodic protection cannot reach the pipe. (Baker 2005)

NNpHSCC is ten times more likely to develop on PE tape-coated pipelines than on asphalt or coal tar coated lines. (Delanty and O'Beirne 1992, Beavers et al. 1998A)

Other types of coatings used include mill-applied fusion bonded epoxy and extruded polyethylene. Fusion bonded epoxy coatings were introduced in the 1970s and are now the most commonly used coating type. (NEB 1996) NNpHSCC has not been identified on pipes with these coatings, but since they are relatively recent technologies, it is generally agreed that further observation is needed before stating that stress corrosion cracking will not occur on pipelines with these types of coatings.

Any type of coating can have holidays, which are holes or interruptions in the coating. These are typically introduced by mechanical damage, such as from rocks that scrape the coating during pipe installation. Under effective cathodic protection, these regions of exposed pipe are not generally an SCC concern, but without cathodic conditions, these areas preferentially corrode, and this process is

accelerated by a large cathode-small anode effect. Thus, care should be taken to prevent the creation of coating holidays during the production, shipping and installation of new lines and during excavations of existing pipelines.

2.2.2.2. Soil Conditions and Topography

For the more than 450 excavations carried out on the TransCanada PipeLines system to inspect for NNpHSCC, no correlation was made between the occurrence of NNpHSCC and terrain type, soil type or soil chemistry. However, there was a tendency for SCC to develop in imperfectly/poorly drained soils in which anaerobic and seasonally reducing environmental conditions exist. (Delanty and O'Beirne 1992) SCC has been located mainly in level or slightly sloped areas, where ground water moves laterally towards and along the pipeline. SCC has rarely been located in areas with stagnant water conditions. (Delanty and O'Beirne 1992)

For asphalt-coated lines, NNpHSCC is more likely in dry areas with high soil resistivity because cathodic protection cannot penetrate the soil in these locations to reach the pipe surface. (Delanty and O'Beirne 1992)

NNpHSCC develops in soil conditions with pH ranging from 5.5 to 7.5. The peak occurrence is seen at pH 6.5. (Parkins et al. 1994) The bicarbonate level in the soil is important in determining the risk of SCC, as it affects the pH that will exist when CO_2 is introduced to the electrolyte. (Zheng et al. 1998)

Clays and silts tend to be poorly drained soils in comparison to sands and gravels, and NNpHSCC has occurred more often in these soil types. (Parkins 1994, Parkins 1996B) A study was conducted to evaluate specific soil environments that were understood from field experience to significantly promote NNpHSCC. (Beavers et al. 2001) This work found that all the soils tested exhibited anodic polarization curves that were similar to that for the commonly used laboratory

electrolyte NS4. The soils with clay had unusual peaks in their hydrogen permeation behaviour. Soils with lower corrosion currents (i_{corr}) and lower corrosion potentials, created higher crack propagation velocities on the API 5L X-65 steel test samples, which indicates that more reducing environments are more potent cracking environments.

A NNpHSCC severity rating model was developed by Delanty and Marr based on soil type, drainage and topography. (Delanty and Marr 1992) Another model for rating soil severity has been developed by Jack, Wilmott and Chen based on the soil's reduction of the open circuit potential (OCP), the generation of diffusible hydrogen, and the reduction in area (%RA) from slow strain rate tests (SSRT) in the soil solution. (Jack et al. 1999) As the latter model requires laboratory testing of the soils in order to evaluate the SCC risk, it is not as widely applicable for use by pipeline companies wanting to prioritize pipeline regions for SCC inspection.

Circumferential NNpHSCC is driven by bending stresses acting on the pipeline rather than by hoop stresses generated from internal pipeline pressure. CEPA has reported that this form of NNpHSCC is associated with undulating terrain where pipeline loading can be caused by soil creep or local bending.

2.2.2.3. Temperature

No relation between temperature and the occurrence of near-neutral SCC has been established. (Parkins 1996B) A higher incidence of colonies has been noted in the pipe joints just downstream of compressor stations, but lab investigations indicate that this is an effect of higher operating stresses rather than higher temperatures. A higher incidence of coating degradation may also exist on sections of pipeline operated at higher temperatures, but this has not been experimentally confirmed. In slow-strain rate tests (a test method that is described in Section 2.2.6.2) in representative near-neutral pH electrolytes, no dependence of temperature on percent reduction of area (%RA) achieved by test samples has been established. (Parkins et al. 1994)

2.2.2.4. Electrolytes

The composition and concentration of the electrolyte are integral factors in determining the probability and severity of near-neutral pH stress corrosion cracking.

The largest electrolyte-related influence on NNpHSCC is the concentration of carbon dioxide. The source of CO_2 in ground water is the decay of organic matter in the soil. (Beavers and Worthingham 2002) Crack velocity is directly related to carbon dioxide concentration, with higher CO_2 levels creating higher crack propagation velocities. (Zheng et al. 1998, Parkins 1999A, Chen and Zheng 2005) While the effect of increasing CO_2 is positive on crack propagation (Beavers et al. 2001, Johnson et al. 2000) it may act to decrease crack initiation as it will increase general corrosion rate, promoting crack blunting and discouraging the development of pits, which are understood to provide sites for crack initiation. (Wang et al. 1999)

The effect of carbon dioxide is investigated in laboratory experiments using sparging gases with different compositions. When a solution is described as being purged with 5% CO_2, balance N_2, this means that a gas with 5% carbon dioxide and 95% nitrogen gas is constantly bubbled through the electrolyte to maintain a constant gas concentration in the test. Increasing the CO_2 concentration in an electrolyte (by using a different sparging gas composition) lowers its pH and increases hydrogen permeation rates, which creates a more aggressive electrolyte. (Johnson et al. 2000, Chen et al. 2002A) Carbon dioxide affects both anodic and cathodic corrosion reactions, but by very different mechanisms. For the anodic reaction, CO_2 has been shown to accelerate steel dissolution by destabilizing oxide films on the surface of the metal. (Linter and Burstein 1999)

The most common solution used in laboratory investigations of near-neutral pH stress corrosion cracking is an NS4 solution bubbled with 5% CO_2. This solution has been developed to be similar to ground water that is found trapped under

disbonded polyethylene tape near NNpHSCC colonies. NS4 solution produces relatively slow cracking; many other very dilute solutions give more rapid cracking. For example, C series solutions are significantly more dilute than NS4 and have been observed to be more effective in creating stress corrosion cracks in experimental work. There is a lower concentration of Cl^- ions in C series solutions than in NS4, which may support crack initiation and prevent crack blunting. (King et al. 2001) This proposed effect is not certain, since work has been published by Gu et al. which found that the concentration of Cl^- does not affect the intensity of NNpHSCC. (Gu et al. 1999A) The concentration of $CaCO_3$ increases in the C series solutions from C1 to C4. Higher $CaCO_3$ concentrations in these solutions give higher pH levels. The compositions of NS4 and C series solutions are given in Table 4.

Table 4 – Compositions of common near-neutral pH test solutions

	g/L KCl	g/L $NaHCO_3$	g/L $CaCl_2 \cdot 2H_2O$	g/L $MgSO_4 \cdot 7H_2O$	g/L $CaCO_3$	pH (with 5% CO_2, 95% N_2)
NS4	0.122	0.483	0.181	0.131	0	6.3
C1	0.0035	0.0195	0.0255	0.0274	0.0061	5.89
C2	0.0035	0.0195	0.0255	0.0274	0.0606	6.29
C3	0.0035	0.0195	0.0255	0.0274	0.2422	6.83
C4	0.0035	0.0195	0.0255	0.0274	0.4845	7.19

The presence and concentration of certain ions may have a significant effect on the tendency of an electrolyte to promote NNpHSCC. Several of these ions and their proposed effects are described here.

It is well established that sulfur promotes the ingress of hydrogen to steel. (Parkins 1998A) Sulfides present in the bulk environment or those evolved from the dissolution of manganese sulfide (MnS) inclusions in the line pipe can support the propagation of stress corrosion cracks in steel. (Van Der Sluys et al. 1998)

The addition of 1% H_2S to a dilute near-neutral pH solution with 10% CO_2 has been shown to dramatically increase cracking rate per cycle (by a factor of about six). While the effect of H_2S in the crack tip on the growth of existing cracks has been demonstrated through experimental research, the ability of sulfides to initiate transgranular stress corrosion cracking requires further research. (Van Der Sluys et al. 1998) Soils typically contain sulfates which can produce sulfides via sulfate reducing bacteria (SRB). (Eadie et al. 2005C) A key indication of the involvement of sulfides in the NNpHSCC process is the presence of iron sulfide corrosion products near the crack site. (Jack et al. 2000)

Adding dilute concentrations of Ca^{2+} and CO^{3-} ions to NS4 electrolyte causes the generation of more hydrogen at the system's OCP. (He et al. 2004) When sufficient calcium is present, it prevents effective cathodic protection. It tends to cause a drop in pH of the solution as it precipitates on the surface as a calcium-carbonate film, counteracting the pH increasing effect that is intended by cathodic protection. (He et al. 2004, Zhang 2003)

The electrolyte pH in regions under disbonded coating increases during tests simulating cathodic protection only when the test electrolyte contains sodium ions. (Zhang 2003)

The ratio of soluble cations (sodium and potassium) to insoluble cations (calcium and magnesium) in electrolytes at SCC and non-SCC sites was investigated by Beavers and Worthingham (2002). The ratio [Na + K]/[Ca + Mg] is lower for near-neutral pH conditions than high-pH conditions, and within the near-neutral pH conditions examined, the ratio was found to be higher at sites were SCC had occurred than at sites without SCC. This relationship was found to have a 93% confidence level by statistical analysis.

Differences in the corrosivity of electrolytes may not be measurable in short-term tests, but such differences have been shown to exist from results of longer-term

tests. When weight loss coupons of X-65 pipeline steel, which has been characterized as very susceptible to NNpHSCC, were exposed to various soil electrolytes including C-series, NS4 and NOVATW, differences in corrosion rates were significant only after extended test times, longer than 10 days. (Chen et al. 2004)

Some corrosion problems can be controlled by the use of inhibitors that change the ionic nature or electrochemical potential of the solution in contact with the metal surface. Unfortunately, there are not any leachable inhibitors available that have been shown to reduce the occurrence of NNpHSCC. (Parkins 1996B)

2.2.2.5. Effect of Applied Potential and Cathodic Protection

As discussed earlier, the pH at which NNpHSCC occurs will only be present in the absence of cathodic current. (Parkins 1999A) Cathodic protection can be prevented from reaching the pipe surface by disbonded tape coatings or dry high-resistivity soils.

Limited general corrosion can be an indication either of passivation or of adequate cathodic protection reaching the pipe surface. However, many NNpHSCC colonies have been found where there is little general corrosion.

In NNpHSCC, steels do not exhibit either passivation or an active/passive transition as is used to explain crack propagation in high pH SCC. Potentiodynamic polarization curves suggest that active corrosion occurs in a NNpHSCC system. (Beavers and Harle 1996, Beavers et al. 1998A)

Tests at more corrosive (anodic) potentials may exhibit a lower incidence of NNpHSCC. As discussed in relation to carbon dioxide concentrations, a more corrosive environment acts to discourage SCC initiation because of higher general corrosion rates. In laboratory work using potentiodynamic polarization tests,

higher cracking rates have been correlated with low corrosion current (i_{corr}) values. (Beavers et al. 2001)

For concentrations of 0 and 0.5% CO_2 in electrolyte sparging gas, the pH of the solution increases in response to cathodic polarization, while for higher CO_2 concentrations (10% and 100% of sparging gas), cathodic polarization has been observed to decrease the pH of the electrolyte. (Beavers et al. 1998A) This finding indicates that higher cathodic current densities are needed in order to maintain cathodic protection on pipelines when CO_2 levels in ground water increase.

When 100mV of cathodic polarization is applied to test specimens in NS4 with a constant 5%CO_2/N_2 sparging gas, the rate of hydrogen permeation has been found to increase by a factor of two. (Beavers et al. 2002) This appears to indicate that this amount of cathodic protection could act to promote NNpHSCC. (Beavers and Garrity 2001) However, this is an effect of the experimental design, in which gas is constantly bubbled through the test cell. The constant supply of CO_2, which acts to keep the pH of the electrolyte in the near-neutral range, allows increased hydrogen permeation and faster SCC rates. In realistic field conditions, there is a very low supply of carbon dioxide in the groundwater and cathodic protection has been shown to raise the pH of the electrolyte sufficiently that NNpHSCC is not a concern. (Chen et al. 2002A)

2.2.2.6. Hydrogen

The empirical observation of the presence of hydrogen in electrolytes is addressed here. Further discussion of the proposed roles of hydrogen in the SCC mechanism can be found in Sections 2.2.5.2.3 and 2.3.4.

Using coupon tests, Beavers et al. (2001) did not find a correlation between hydrogen permeation and crack growth rates. A number of tests using hydrogen pre-charging of metal specimens have compared behaviour including stress-strain

curves, existing crack growth and crack initiation in air and near-neutral pH electrolytes. These tests have demonstrated that hydrogen pre-charging facilitates SCC. (Gu et al. 1999A)

Using SSRT, Jack et al. (1999) were able to correlate crack growth with hydrogen concentration in the test electrolyte. In this work, higher hydrogen concentrations were found to be associated with high bicarbonate levels instead of with low pH, suggesting that the source of the hydrogen for cracking related mechanisms must be bicarbonate, not H^+ ions.

Hydrogen charging reduces the ductility of steel, causing it to fracture at a lower total strain. (Tyson 1979) Results from work by Delafosse and Magnin (2001) are shown below which illustrate that as a more negative cathodic potential is imposed on a SSRT specimen so that more hydrogen is present in the steel, it exhibits failure at decreasing elongations.

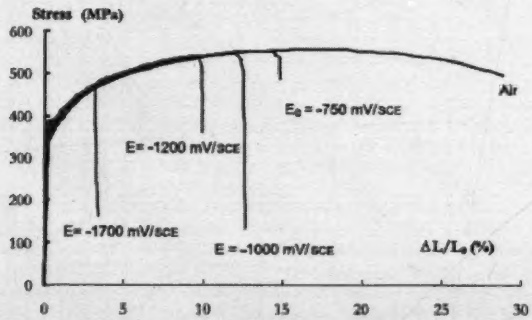

Figure 2- Stress-strain curves of X-52 in air and at different values of imposed electrochemical potential in NS4 solution [Source: Delafosse and Magnin 2001]

The reduced ductility of pipeline steels with hydrogen ingress requires an ongoing supply of hydrogen during the deformation process. (Parkins 1998A) SSRT tests of uncharged and pre-charged specimens in air, and pre-charged specimens in near-neutral solution show that when specimens are pre-charged with hydrogen, but then stressed in air, the alloy exhibits very similar ductility to the specimens that have not undergone hydrogen charging, while those strained in solution exhibit a marked reduction in ductility. Figure 3 clearly illustrates this effect and

also shows that when straining is done on specimens in solution that have not had time to reach equilibrium with the hydrogen in solution, these tests give similar results to tests in air. (Yu 1997)

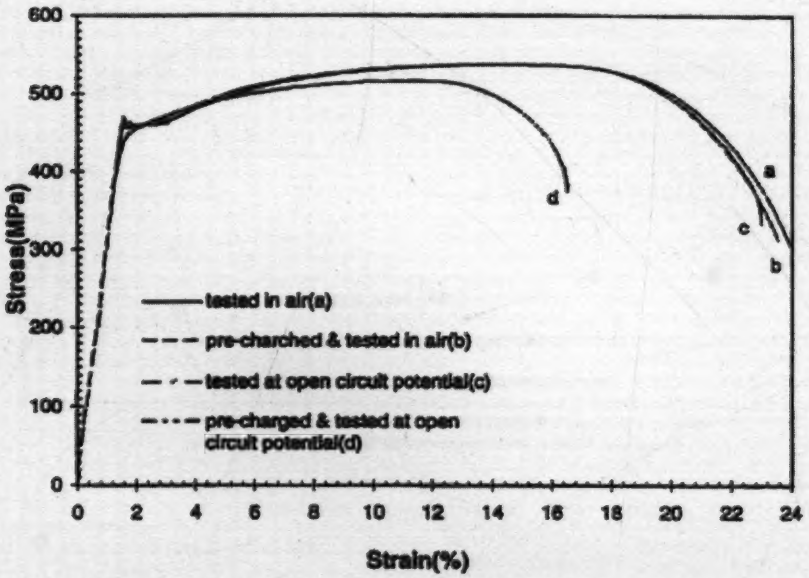

Figure 3 - The effect of hydrogen pre-charging and solution exposure on SSRT stress-strain curves for X-52 steel tested at 1x10-6 / sec in air and in NS4 [Source: Yu, 1997]

2.2.2.7. Bacteria

Sulfates are naturally present in soil. Sulfate reducing bacteria (SRB) can create sulfides from these sulfates, and sulfides are understood to support stress corrosion crack growth rate. (Eadie et al. 2005C) However, microbial reduction of sulfate to sulfide is not a widely observed phenomenon in NNpHSCC. The main effect of sulfides is to poison the recombination of hydrogen so that higher amounts of hydrogen enter the steel. Trace levels of sulfide may support cracking by altering the anion ratio in the electrolyte. (King et al. 2000) Field and laboratory work has investigated the nature and importance of this relationship.

Another type of bacteria that has been investigated in relation to NNpHSCC is acid producing bacteria (APB). APB creates organic acids from the organic constituents in soil and it is thought that these acids may promote NNpHSCC by

maintaining a low electrolyte pH, and by providing H^+ ions for the crack propagation mechanism, which is understood to be hydrogen related.

Field excavations of PE tape-wrapped pipelines have found SRB and APB present in varying concentrations. Comparison of bacterial concentrations with the severity of identified SCC colonies suggests that higher bacteria counts are associated with areas of more severe SCC. (Delanty and O'Beirne 1992) This could be due to the CO_2, H_2S and organic acids produced by the bacteria, since these compounds have been shown to increase SCC even without the presence of bacteria.

In tests to characterize the effect of SRB on environmentally enhanced fatigue cracking, fatigue crack propagation in a deaerated bacteriological solution containing SRB was compared with that in a 3% sodium chloride solution. The presence of SRB was found to increase fatigue crack propagation rates significantly, with cracks propagating in the aqueous bacterial environment up to 1000 times faster than in a vacuum and 40 times faster than in a 3% NaCl solution. (Gangloff and Kelly 1994)

The growth of SCC cracks is associated with a decline in the sulfate concentration of the electrolyte. This observation could indicate an active involvement of SRB species in the propagation of stress corrosion cracks. (Wilmott et al. 1996)

It should be noted, however, that the effect of bacterial populations on NNpHSCC is not yet confirmed or fully understood. For example, the data from full scale tests of 48 cracks in 3 soil boxes carried out at CANMET-MTL did not correlate crack growth with microbial populations of APB or SRB. (Zheng et al. 1996B)

2.2.2.8. Seasonal Variations

The conditions at the pipeline surface vary significantly throughout the year. Variations in temperature, dissolved carbon dioxide and oxygen concentrations,

carbonic acid, electrolyte pH and soil drainage can be observed. There are indications that some of these changes may play a role in the development and progression of NNpHSCC in the field.

Carbon dioxide concentration in the groundwater has been identified as the most important electrolyte-related factor influencing NNpHSCC. CO_2 concentrations in the soil adjacent to pipeline surface have been measured to vary from a minimum of 4% in the winter to a maximum level of 23% CO_2 during the spring. (Delanty and O'Beirne 1992) However, this study was based on samples taken at three locations along one valve section of pipe that had been identified as highly susceptible, so while the trend of seasonally varying CO_2 concentrations is generally accepted, the wider applicability of these concentration values to describe CO_2 conditions near pipeline surfaces has not been confirmed.

Related to the CO_2 concentration, the level of carbonic acid, H_2CO_3, measured in the soil can be more than 20 times higher in the winter (when CO_2 concentration is at a minimum). This seasonal change in soil acidity means that the pipe is exposed to a lower pH electrolyte during the colder months. (Delanty and O'Beirne 1992)

Environmental changes such as reduced CO_2 levels may cause crack dormancy. By comparing measured soil electrolyte conditions with results of laboratory crack investigations in a range of electrolyte conditions, it is reasonable to propose that crack growth may occur only during the fall and winter months when the soil electrolyte is most acidic and concentrated and that dormant or near-dormant crack conditions may develop during the spring and summer. (Beavers and Harle 1996)

It is also possible that the repeated interruptions in acidic conditions during the spring and summer months may accelerate the cracking that does occur under the fall/winter conditions that promote NNpHSCC. As a parallel example, higher

overall crack growth was observed in cyclic loading tests that were interrupted and removed from the test solution at several stages to allow for interim measurement of cracks than in tests in the same research work that were conducted without interruptions. (Rebak et al. 1996)

It is usually assumed that NNpHSCC occurs under anaerobic conditions without effective cathodic protection. A NOVA field study measured soil aeration levels using a redox probe and NNpHSCC was correlated with anaerobic conditions. (Wilmott et al. 1995, Zheng et al. 1996A)

While NNpHSCC appears to occur in electrolytes lacking dissolved oxygen, it is unlikely that a pipe surface only two meters below ground level would never be exposed to aerated conditions. Thus, characterization of the effect of oxygen on NNpHSCC is important in developing a better understanding of this cracking mechanism.

The presence of oxygen in the electrolyte provides another possible reduction reaction (1) thereby increasing the corrosion potential and reducing the rates of the reaction that generates hydrogen, (2). Oxygen may react to form a surface corrosion product that acts to block hydrogen entry into the material.

$$O_2 + 2H_20 + 4e^- \rightarrow 4OH^- \quad (1)$$

$$2H^+ + 2e^- \rightarrow H_{2(g)} \quad (2)$$

In laboratory work, the presence or concentration of oxygen in the electrolyte does not affect the rate of general corrosion in the system, but has been shown to decrease hydrogen permeation and increase crack growth rates. 10 or 20% O_2 in the sparging gas has been shown to increase crack growth, while 1% O_2 actually decreased crack growth. (Johnson et al. 2000) The effect of oxygen concentration on OCP was small (about 20mV) in both cases. The increase in crack growth rates in the presence of oxygen is surprising because of the expected and observed decrease in hydrogen absorption. This effect makes it clear that the

crack growth mechanism involved in near-neutral pH stress corrosion cracking is more complicated than a simple hydrogen embrittlement process. The effect of O_2 on crack initiation was not investigated in this work. Oxygen exposure has been demonstrated to have a detrimental effect on steel ductility in near-neutral environments. Slow strain rate testing at E_{corr} was done both in NS4 solutions exposed to air and in NS4 solutions that were purged with 100% N_2. The air-exposed solution gave test results with lower %RA values than those from the nitrogen-purged solution. These results suggest that O_2 may assist in SCC, possibly by reducing the ductility of pipeline steel in groundwater. (Gu et al. 1999A)

A number of factors and their proposed effects on NNpHSCC have been outlined here. None of these seasonal effects is well understood and it is generally agreed that more research is required into the effects of seasonal variations in environment on NNpHSCC. (Parkins 1999A, Eadie et al. 2005B)

2.2.2.9. Summary of Environmental Factors

The most significant environmental factors leading to NNpHSCC are pipe coatings, groundwater composition, pH and carbon dioxide content. Polyethylene tape coated line pipe is most susceptible to NNpHSCC because disbonded coating shields the pipe from cathodic protection. When cathodic protection is effective, NNpHSCC will not occur because the pH of the groundwater will be raised out of the susceptible range. The composition of the groundwater surrounding the pipe is very important; more dilute solutions with bicarbonates are more aggressive. Dissolved CO_2 in the groundwater enhances NNpHSCC by lowering the pH and providing bicarbonate ions. Sulfides have been found to promote propagation of existing cracks.

NNpHSCC is more likely in poorly drained soils where anaerobic conditions exist. These soil conditions typically exist in sloped areas where groundwater is flowing rather than stagnant. No relation has been established between

temperature and the occurrence of near-neutral pH stress corrosion cracking. It is possible that SRB and APB may contribute by providing hydrogen and promoting its ingress, but this requires further study. Seasonal changes in groundwater pH may cause dormancy in the spring and summer months, and accelerate cracking in the fall and winter months.

2.2.3. Stressing Factors affecting Near-Neutral pH SCC

Oil and gas pipelines are subjected to a variety of stresses. Operational conditions require the pipelines to sustain internal pressure, which creates both circumferential (hoop) and axial stresses in the material. Internal pipeline pressures vary over time; as a result, pipes experience variations in hoop and axial stress over time. Secondary stresses acting on a pipe can be caused by localized bending or by axial tension. These types of stresses are typically created during the installation of the pipeline or by changes in the support offered by the soil. For example, heavy rains or flooding can cause a washout of some of the soil near a pipeline, and the pipeline may then experience localized bending if it sags where the soil has been removed. The level of secondary stress can be very high and may exceed operational stresses. Significant localized bending stress or axial tensile stress can result in the circumferential cracking of a pipeline. (Zheng et al. 2000)

SCC susceptibility and severity are dependent on pipeline operating pressure. In Class 2 and 3 pipeline locations with lower operating stresses, significant NNpHSCC has not been reported. (NEB 1996) On one line inspected, a section operating at 75% SMYS was found to have a linear density of SCC colonies that was more than 25 times higher than another section of the line operating at 67% SMYS. (Baker 2005)

2.2.3.1. Cyclic Loading Effects

The general description of stress corrosion cracking states that it requires the simultaneous existence of a potent environment, a susceptible pipe surface, and a sustained tensile stress. For high-pH SCC environments, a static tensile stress can

lead to the initiation and propagation of cracks, but for NNpHSCC, researchers have experienced much difficulty in generating cracks by static loading. (Beavers and Harle 1996, Zheng et al. 1996B, Wilmott and Sutherby 1998, Meyer and Pontremoli 2001)

Cyclic loading is necessary in order to generate NNpHSCC in the laboratory. The loading factors which control cracking are the maximum stress applied, the amplitude of the stress variation, and the amplitude of the stress intensity factor range (ΔK) at a crack. The most commonly used stress profiles in laboratory simulations of NNpHSCC are a triangular waveform (also called a saw tooth wave), and a trapezoidal stress waveform.

The maximum stress applied is generally stated in terms of the yield strength, either as the percentage of the specified minimum yield strength (%SMYS) or as the percentage of the actual yield strength (%YS). The actual yield strength can be from 10% to 30% higher than the SMYS stated by the manufacturer. (NEB 1996)

The applied stress is varied over time, either in a repeating cyclic pattern in laboratory work, or along a more random path for in-service pipelines. The amplitude of this variation is generally stated as an R-value, defined as the ratio of the minimum stress to the maximum stress.

$$R = \frac{\sigma_{min}}{\sigma_{max}} \tag{3}$$

The stress intensity factor, K, is a calculated value often used in linear elastic fracture mechanics to describe the stress conditions at a crack tip. For linear elastic fracture mechanics to be applicable, the crack size must be much larger than the plastic zone size. (West 1982) A subscript is used to denote the mode of crack opening. For pipeline surface cracks, the opening mode is Mode I, and the

stress intensity factor is K_I. The simplest case that can be applied to SCC testing is for a through thickness edge crack on a flat specimen.

$$K_I = 1.12\sigma\sqrt{\pi a}\, f(a/w) \quad (4)$$

where

σ is the stress

a is the crack length

f(a/w) is a geometry factor

The stress intensity factor range is simply the difference between K_I at the maximum and minimum stress conditions, σ_{max} and σ_{min}.

A study of actual oil and gas line pressure variations was conducted by CEPA in order to provide researchers with guidelines for realistic cyclic loading conditions experienced by in-service pipelines. (Sutherby et al. 2000) A low R-cycle was defined as R<0.5. This study found that liquid pipelines average 2500 low R cycles annually while gas pipelines undergo fewer than 10 of these large amplitude cycles per year. The average time for a stress cycle was also evaluated. The pressure changes in liquid-carrying lines occur much more quickly than those in gas lines. An oil pipeline can drop from a maximum pressure to a minimum pressure in only 15 minutes, while this takes about 24 hours in gas lines. This difference is due to the low compressibility of the fluids carried in liquid pipelines. Liquid pipelines experience a larger proportion of higher amplitude stress cycles than gas pipelines; 90% of the pressure data recorded for liquid pipelines in the CEPA study involved cycles above R = 0.7, but for gas pipelines, 90% of the pressure cycle data was above R = 0.9. To impose realistic field loading conditions in laboratory experiments, it is suggested that the appropriate rate for very low R cycles for liquid pipelines is 50 cycles/day and 0.5 cycles/day for gas pipelines. (Sutherby et al. 2000)

Using hundreds of thousands of load cycles with low R-values, researchers at CANMET were able to produce colonies of cracks that looked much like

NNpHSCC. (Wang et al. 1999) Such a high number of cycles could possibly occur in oil pipelines but is very unlikely in gas pipelines. Thus, a different loading scheme must be responsible for stress corrosion cracking on gas pipelines. Other tests conducted with realistic loading conditions based on field-collected pressure data were able to produce only microcracks, which tended to reach a dormant state within the test period. (Van Boven 2003, Chu et al. 2003, Chen et al. 2003)

The R-value used in experiments has a very significant impact on crack growth. In tests conducted by Beavers and Hagerdorn (1996), when the R-value imposed on test specimens was decreased from 0.9 to 0.6, without changes to other loading factors, the crack growth rate was measured to increase by a factor of two.

It is important to be able to distinguish between loading conditions that cause true NNpHSCC and those that drive cracking solely by mechanical means. When the R-value is lowered (and the ΔK increases correspondingly), there is a transition in cracking mechanism from stress corrosion cracking to corrosion fatigue as the dominant propagation mechanism. This distinction is not easy to make, since NNpHSCC involves the interaction of a number of factors that must exist in the correct balance.

For example, short-term crack growth rates measured in lab simulations have not been correlated to soil chemistry. However, one study has shown that this lack of correlation may be caused by the high stress amplitudes used in the majority of simulations. This investigation by Chen and Sutherby (2004) showed that crack growth rate was sensitive to soil conditions only in the low ΔK regime. Additionally, specimens stressed with a low ΔK value showed greater amounts of dissolution at the crack tip while specimens subjected to high ΔK generally had sharper crack tips. It is understood from this work that when high ΔK values are used in testing, cracks are mainly advanced by mechanical driving forces instead of dissolution, but a clear delineation of loading conditions that produce

NNpHSCC has not been established, and may prove impossible to define because of the complexity of the interacting factors.

While the magnitude of the stress intensity factor range, ΔK, is often used as a descriptor of the variation of the stress state at propagating crack tips and is correlated to crack growth rates, it is necessary to recognize that plastic deformation does occur in the region of the crack during the stress cycle. The stress intensity factor is only valid for predominantly elastic conditions. For elastic-plastic behaviour, a fracture mechanics value known as the J-integral can be used to quantify the stress conditions surrounding the growing crack. This technique is discussed further in Section 2.2.5.3.4, but is included here to highlight that the correlation between ΔK and crack velocity is an approximation based on the assumption of elastic material behaviour. Plastic zone effects introduce an error in the crack growth that is estimated to occur during load increases on the specimen. (Beavers and Jaske 1998)

The effect of loading frequency on NNpHSCC is still unclear. Tests were conducted by Beavers and Jaske at a constant ΔK value which indicated that higher frequencies give higher crack-opening rates during re-loading. (Beavers and Jaske 2000) This could be extended to a prediction that higher frequencies would promote faster crack propagation rates. Crack propagation rates can be quantified as crack growth per unit of time (da/dt) or per loading cycle (da/dN). In 1996, the NEB inquiry stated that lower frequencies give higher crack propagation rates per loading cycle (da/dN). Eadie et al. quantified this relation in 2004 with the observation that a decrease in the frequency of loading by an order of magnitude increased da/dN by a factor of $\sqrt{10}$. Framing the cracking rate differently, Been et al. (2001) stated that increased frequencies give higher rates of crack propagation per time (da/dt), and furthermore suggested that frequency affects crack rate more than strain rate does. Care must be taken when expressing the effect of loading frequency on cracking rate, as a lower frequency can cause

more crack growth per load cycle (da/dN) yet still decrease the crack growth rate over time (da/dt).

Circumferential cracks depend mainly on residual stresses and bending stresses acting on pipe, pressure variations affect longitudinal stress only about ½ to 1/3 as much as they affect circumferential tensile stresses in pipes. Longitudinal cracking has a higher chance of leading to large failures than circumferential cracking, as the crack can rapidly propagate down the line during rupture. (Arrigoni and Sinigaglia 1997)

For high pH SCC, a threshold stress intensity factor, denoted K_{ISCC}, exists below which cracking will not occur. A similar threshold for near-neutral pH SCC may exist, but has not yet been confirmed. For high pH SCC, this threshold is not a material property. Instead, it is dependent on environmental factors and the metallurgical conditions of the material. If a near-neutral pH K_{ISCC} is established, similar dependencies are expected. Surkov et al. have identified a 5 MPa$\sqrt{m}$ threshold K value below which near-neutral pH stress corrosion crack initiation is not anticipated. (Surkov et al. 1994) Further support for the possibility of threshold stress intensity factor comes from findings by Beavers and Jaske (2000) that cracks tended to dormancy when exposed to ΔK values of less than 10MPa$\sqrt{m}$.

The loading history experienced by pipeline steel before its exposure to a near-neutral environment has been shown to be another significant factor in NNpHSCC. In experimental work by Beavers and Jaske (1998), the prior loading history on test specimens was shown to be the primary controlling factor in determining the crack velocity. Work by Chen et al. (2003) found that cyclic loading prior to corrosion exposure either reduced or increased the crack initiation and growth, depending on the magnitude of the stress cycles. The largest reduction in crack initiation was observed for a maximum precyclic stress of 80% of the yield stress. This effect may be related to alteration of the substructures or

residual stresses. Cyclic loading in the absence of a corrosive environment can cause the development of persistent slip bands, which have been identified as initiation sites for NNpHSCC. A better understanding of precyclic loading could provide a means to reduce the likelihood of SCC on existing pipelines that have not yet suffered from coating disbondment or been exposed to a near-neutral pH environment. A strong dependence of microcrack initiation on precyclic loading was observed in work by Chen et al. (2003). Depending on the maximum stress level, precyclic loading was able to prevent the formation of microcracks. It is thought that this reduction in microcrack initiation is a result of an alteration of the existing internal (residual) stresses in the steel.

A large number of other observations about the effect of stress conditions on NNpHSCC have been made. The stress range ($\Delta\sigma$) is said to be more important than the absolute stress (σ_{max}) in determining crack propagation rates. (Beavers and Jaske 2000) As addressed in the section on hydrostatic testing, crack growth is understood to occur much faster during transient loading events, such as unloading experienced during pipeline shutdowns, than growth rates during normal steady state stress cycling.(Beavers and Jaske 1998)

2.2.3.2. Strain Rate Effects

As indicated by the difficulty encountered by researchers in trying to reproduce NNpHSCC at constant stress levels, dynamic straining at the crack tip is a prerequisite for NNpHSCC crack growth. (Zheng et al. 1996B)

Crack growth rates increase with increased strain rate. Crack tip strain rate is a function of the R-value and loading frequency of the cyclic stressing. Crack velocity has been correlated reasonably well with crack tip strain rate over a range of loading conditions. (Beavers 2004) The effect of strain rate is most pronounced at intermediate values. If it is too high, simple ductile fracture will occur before corrosion or hydrogen permeation takes place. (Gu et al. 1999B) Decreasing the frequency of load cycles allows more time for hydrogen to diffuse

into the metal. (Eadie et al. 2005C) Even without the presence of hydrogen, strain was shown to increase corrosion rates by an order of magnitude suggesting that localized microplasticity, or some other hydrogen independent strain effect, contributes to the propagation of SCC. (Lichter et al. 2001)

In the CEPA study of actual oil and gas line pressure variations that was discussed earlier, no significant difference was observed between the strain rates of pipelines during loading and unloading. The majority of the measured strain rates were within an order of magnitude of each other with twenty of the twenty-three collected pressure histories showing average strain rates of less than 10^{-8} s^{-1}. In this data group, a strain rate of 10^{-6} s^{-1} would represent an exceptional value. (Sutherby et al. 2000)

More research is needed into the effect of time delay between cycles, as normally occurs in the operating pipelines. Gas lines experience major pressure fluctuations only a few times per day. The dissolution and repassivation reactions occurring in the cracks between these events are probably the key processes controlling crack shape and tip sharpness. (Zheng et al. 1996B) Several effects could tend to slow cracking including corrosion blunting of the crack tip or room-temperature creep causing crack-tip blunting. Chen and Sutherby (2004) have observed crack tip blunting at 0.0025 Hz and attributed the effect to room-temperature creep at the crack tip.

Stress-strain curves of pipeline steels are typically strain-rate dependent. These steels exhibit higher strengths when loaded at a higher strain rate. Higher strain rates also have been documented to cause larger room-temperature creep deformation during a constant stress hold period after the loading ramp-up. (Wang and Chen 2001) Since room temperature creep is thought to contribute to NNpHSCC (Eadie et al. 2005B), this correlation between strain rates and room-temperature creep may be a reason that higher strain rates produce higher crack growth rates.

2.2.3.3. Hydrostatic Testing

Hydrostatic testing is an integral component of most integrity management programs for gas pipelines. It is used to detect cracks or leaks and create a known safety factor for operating pressures for some time that is estimated based on general or pipeline-specific crack growth rates. The implementation of systematic hydrostatic testing has reduced the occurrence of in-service pipeline failures in North America. (Parkins 1994)

In this type of test, pipelines are cleared of the gas that they usually transport and are filled with water, which can be pressurized according to test procedures. A typical hydrostatic test consists of a short duration high-pressure spike (100-110% of SMYS for 1 hour) to remove flaws capable of producing a rupture, followed by a long duration low-pressure test (90% of SMYS for 24 hours) to locate leaks in the pipeline. (Brongers et al. 2000) Hydrostatic test ruptures do not propagate a long way because water is incompressible and the stress exerted on the pipeline drops off quickly after a rupture occurs. (Baker 2005)

Research findings indicate that hydrostatic testing does not shorten the life of pipelines. The high pressures used in hydrostatic testing have been observed to cause crack blunting, which can slow subsequent crack growth. Thus, the test procedure may cause cracks to grow during the over-pressurization period, but crack growth rates are typically depressed for some time afterwards so that the net effect of the hydrostatic test is usually no change in the predicted life of the pipeline, or possibly even an increased life. Hydrostatic testing above the SMYS has the potential to be used to inhibit crack initiation by increasing the stress level at which cracks will initiate. (Harle et al. 1995)

Near-critical imperfections in low toughness steel respond faster to testing than similar imperfections in high toughness steel, a factor that should be kept in mind during the design of hydrostatic tests as part of a pipeline integrity management program.

Overall, hydrostatic testing is no more harmful to a pipeline than depressurization. (Beavers and Hagerdorn 1996) In fact, the unload-reload transients associated with depressurization of a pipeline can accelerate or re-initiate cracking and may be more detrimental to pipeline integrity than over-pressurization. (Beavers 2004)

Ductile tearing is a main concern for the damage of steels during hydrostatic testing. Laboratory investigations have determined that the extent of ductile tearing occurring under typical hydrostatic test conditions is small, but increases for longer and deeper flaws, and varies directly with the J-integral. (Brongers et al. 2000) In laboratory simulations, the DCPD technique is frequently used to measure crack growth rates, but has been shown to overestimate the extent of ductile tearing. An alternate method, such as metallographic examination of tested and untested cracks, is needed for assessing the ductile tearing damage caused during a hydrostatic test. (Brongers et al. 2000)

2.2.3.4. Stress Raisers

Of the eleven ruptures reviewed in the1996 National Energy Board inquiry, all were associated with a stress raiser. Five occurred near the long seam weld on the pipe, five were associated with linear general corrosion and one failure initiated from a gouge on the pipe surface.

Pipelines are operated in a stress range well below the yield point of the material. Depending on the location of the pipeline section in relation to population density or environmentally sensitive areas, a pipelines maximum operating stress is between 72 and 80% of SMYS. Laboratory tests of pipeline samples at this stress level have encountered significant difficulty in creating NNpHSCC without stress amplitudes higher than those typically experienced by in-service pipelines. (Zheng et al. 1996B, Elboujdaini et al. 2000)

Localized areas of high stress can be created by geometrical stress raisers. The stress concentrations caused by longitudinal weld toes, corrosion pits and gouges have been shown to create local stresses much higher than the material yield strength, even when the average stress in the pipe is 80% of SMYS. (Eadie et al. 2002) For example, the geometry of several longitudinal weld toes have been modeled using elastic finite element analysis and the stress concentration factors at these locations were found to range from 1.2 to 2.8. (Eadie et al. 2002) At these higher stress levels, NNpHSCC is much more likely to develop and propagate. Thus, stress raisers play an important role in the phenomenon of NNpHSCC on pipelines.

2.2.3.5. Residual Stresses

A strong correlation between residual stresses and the presence of NNpHSCC colonies has been shown in work by Beavers et al. (2000). In areas near SCC colonies that developed on in-service pipelines, mean residual stresses were found to be twice as high as in unaffected areas (216 MPa vs. 108 MPa). This relationship was calculated to have a 99.98% confidence level. Laboratory work has shown that formation of micro-pits and microcracks occurs preferentially in areas where the tensile residual stresses were about 200 MPa. (Van Boven 2003)

There are two main sources of residual stresses during the manufacture of line pipe: the forming process to shape flat steel plate into round pipes and the welding along the pipe seam. (Beavers et al. 2000) When plate is bent into a round shape to form pipe and welded along the seam, this creates elastic and plastic deformation in the material. The typical result of this forming process is tensile residual stresses in the pipe. These stresses can be reduced by hydrostatic test pressurization of the pipe. In the body of the pipe, residual stresses are typically tensile and have been measured between 0 and 29% of yield strength. (Roy et al. 1993) Tensile residual stresses of these levels can contribute significantly to NNpHSCC.

Welding during pipe manufacture creates very localized residual stresses by the different cooling rates and creation of different microstructures in the heat affected zone (HAZ) surrounding the weld. Uneven cooling processes can introduce both tensile and compressive stresses in the HAZ. In the longitudinal weld region, residual stresses have been measured to vary from compressive stresses that are 77% of the yield strength to tensile stresses that are 10% of the yield strength. (Roy et al. 1993) Residual stresses at girth welds may produce a resultant tensile axial load within a pipe, increasing chances of circumferential SCC. (Baker 2005) The longitudinal weld toe, in addition to being a region of high compressive residual stresses, acts as a geometrical stress raiser, magnifying the effect of operating hoop stresses in this region. (Eadie et al. 2002)

Residual stresses can also be introduced during pipeline installation or settling. Circumferential SCC is frequently a result of residual stresses or bending stresses caused by the soil or pipeline configuration. Over half the cases of circumferential SCC detected in Alberta have shown denting or buckling in the pipe, which are indications of secondary stresses. (Sutherby 1998)

The effects of residual stresses can be mitigated in a few ways. The residual stresses in a pipe can be relieved by heat treatment. The probability of pitting or general corrosion on surfaces with compressive residual stresses is lower than that on surfaces under tensile stress. (Van Boven, 2003) Compressive residual stresses introduced to the surface of the material by shot peening or grit blasting improve SCC resistance. Grit blasted surfaces have been shown to be more resistant to high pH SCC because the blasting imparts a compressive residual stress at the surface and removes mill scale. These beneficial effects likely apply to near-neutral pH SCC initiation as well. (Beavers et al. 1993, Beavers et al. 1993B) However in using this approach, care should be taken to select an appropriate blasting grit. Lower quality commercial blasts may actually reduce SCC resistance by imbedding mill scale particles into the surface of the metal.

2.2.3.6. Crack Velocities

Knowledge of the rate at which stress corrosion cracks grow is very useful in estimating the remaining life of a pipeline that has existing crack colonies. However, a broad range of crack velocities have been measured and no reproducible correlation of these rates to environmental, stressing or metallurgical factors is available. Crack rates can be expressed with respect to time (da/dt) or loading cycles (da/dN).

Beavers and Hagerdorn (1996) described typical crack rates as those between $1x10^{-8}$ and $2x10^{-8}$ mm/s. Crack growth rates observed in experimental work by Eadie et al. (2005C) ranged from $1.2x10^{-5}$ to $1.7x10^{-2}$ mm/cycle or from $4.8x10^{-6}$ to $3.0x10^{-3}$ mm/s, under conditions that were representative of the pressure variations in a high pressure gas pipeline but at a much accelerated frequency (0.04 Hz) which could be more directly compared to the cyclic loading frequency experienced in liquid pipelines. (Eadie et al. 2005C) As discussed earlier, cyclic loading prior to corrosion exposure is understood to have a significant effect on crack growth. (Beavers and Hagerdorn 1996) Crack velocity is also dependent on many other conditions; it is lower for tests with lower frequencies, higher R-values and lower CO_2 concentrations. (Beavers 2004)

Many near-neutral pH stress corrosion cracks reach a state where they cease to propagate or do so slowly enough as to be undetectable. Crack dormancy has been defined as $2x10^{-9}$ mm/s by two different methods: as the rate that will not threaten the pipeline integrity over its anticipated service life, and as a crack rate that is equal to the general corrosion rate of the steel in the underground environment. (Beavers 2004)

2.2.3.7. Summary of Stressing Factors

Important stressing factors related to near neutral pH stress corrosion cracking are maximum stress, cyclic stress amplitude, strain rate and prior loading history. Higher internal pressures are known to cause more SCC colonies. The current

understanding of NNpHSCC is that cyclic loading is required for cracking to occur. Liquids pipelines experience many more large amplitude stress cycles than gas pipelines, and these cycles also take place more quickly. Laboratory testing using realistic gas pipeline stressing conditions have not produced cracks similar to those leading to field failures. Instead, the cracks generated tend towards dormancy. (Beavers et al. 2001, Beavers 2004)

Thresholds of R-value, ΔK and operating pressure, below which cracks will not initiate or grow, have all been proposed and supported with experimental data, but none of these thresholds have been conclusively defined or proven. Loading that occurs before a pipe is exposed to the environment through failure of the coating may either prevent or support the initiation of NNpHSCC. A better understanding of these effects is needed. In laboratory tests, intermediate strain rates have been shown to create the highest crack growth rates. If the strain rate is too slow, crack tip blunting can occur by dissolution and room temperature creep. If the strain rate is too high, such as in severe slow strain rate tests, simple ductile failure can occur in place of NNpHSCC.

The temporary elevated pressures during hydrostatic testing may slow the growth of existing cracks. A pipeline depressurization may accelerate or re-initiate cracking. Geometrical stress raisers and residual stresses created during pipe manufacture contribute significantly to the effective stress at locations that are observed to have a high occurrence of SCC colonies.

2.2.4. Metallurgical Factors affecting Near-Neutral pH SCC

A susceptible material is the third key requirement for stress corrosion cracking. Much work has been done to understand the factors that make a pipeline steel susceptible to NNpHSCC. Variables that have been investigated include mechanical properties such as strength and toughness, and physical properties such as microstructure, inclusions, surface condition, and millscale, and other factors such as weldments and manufacturing processes.

2.2.4.1. Steel Surface Condition

Original pipe surfaces have consistently been shown to initiate NNpHSCC more readily than polished surfaces. (Parkins et al. 1994, Wang et al. 1999) This higher initiation susceptibility could be due to surface roughness, the presence of mill scale, residual stresses or minor scratches on the original surface.

A correlation between pipe surface roughness and SCC has been demonstrated by researchers. In work to investigate this relation by examination of pipe sections that had developed NNpHSCC while in service, Beavers et al. found a higher average roughness near SCC colonies than in unaffected areas of the same pipe, with a confidence level of 87%. (Beavers et al. 2000) Laboratory work has shown that polished surfaces require lower R-value (higher amplitude) stressing to initiate cracking than required for initiation on rougher surfaces. (Elboujdaini et al. 2000) Investigating this relation in connection with corrosion potential, He et al. (2000) applied different surface roughnesses to specimen surfaces by using 240- and 600-grit sandpapers, and concluded that the effect of roughness on SCC susceptibility is minor at OCP (the conditions under which NNpHSCC occurs) but becomes significant at cathodic potentials, with rougher surfaces having a higher occurrence of stress corrosion cracks.

King et al. (2000) have observed that localized dissolution occurs near scratch marks in near-neutral environments with potentials 100 – 200 mV more negative than open circuit potential. NNpHSCC initiation was significantly increased by artificial scratches introduced orthogonal to the stress axis. In the same work, scratches applied parallel or at 45° to the stress axis had little effect on the development of cracks. (He et al. 2000)

2.2.4.2. Mechanical Properties

No correlation between pipe grade and SCC detection frequency has been evidenced. (CEPA 2000) Much of the NNpHSCC detected to date has been on X-52 and X-65 pipeline steel; however, the majority of pipeline installed with PE

tape coating during the 1960s and 1970s was made with these types of steel. (Parkins 1994) Laboratory comparisons of a number of pipe grades in relation to SCC resistance have established no correlation. (Baker 2005)

Steels with higher toughness values, while not necessarily more resistant to SCC, may be less likely to experience ruptures in service than lower toughness materials because higher toughness values increase the critical size of cracks that can result in sudden failure by fracture. (Baker 2005)

In addition, no correlation has been demonstrated between the chemical composition of steel and its SCC susceptibility. (Beavers et al. 2000)

2.2.4.3. Microstructure

More uniform microstructures such as bainite or bainitic ferrite appear to be less susceptible to NNpHSCC than banded structures and pearlite colonies. (Meyer and Pontremoli 2001, Chu et al. 2003, Chen et al. 2003, Kushida et al. 2001) Kushida et al. concluded that a homogeneous microstructure is important to NNpHSCC resistance. In this work, five steels were ranked on their resistance to SCC. The steels tested were X-65 TMCP and X-80 TMCP (thermomechanical-controlled processing), X-65 QT (quenched and tempered), X-65 CR (controlled rolling) and 5LB. These steels had microstructures of bainitic ferrite, bainite, bainitic ferrite, ferrite-pearlite and ferrite-pearlite respectively. In order from best to worst NNpHSCC resistance, the steels were ranked: X65QT, X65TMCP, X80TMCP, X65CR, and 5L B. The differences in SCC resistance were explained by microstructure, and were not related to the strength of the steel.

Initiation of microcracks leading to stress corrosion cracks has been observed by Chen et al. to occur by selective attack at grain boundaries, pearlite and microstructural bands. Unlike the intergranular mechanism associated with high pH SCC, the corrosion attack at surface grain boundaries that was studied in this

work did not continue along grain boundaries into depth and propagated transgranularly instead. (Chen et al. 2003)

In pipeline steels, banded structures will generally exist parallel to the pipe surface as a result of manufacturing processes. Therefore, these banded structures are less likely to serve as initiation locations for cracks on pipelines than on laboratory specimens, but are still confirmed as regions of higher SCC susceptibility in a more general sense. (Chu et al. 2003)

The effects of cathodic polarization in preventing NNpHSCC are dependent upon crack tip microstructure. In ferrite-pearlite structures, a cathodic potential of 100mV slows crack growth considerably but increasing that potential to 200 mV restores crack growth rates to the same levels as observed at open circuit potential. In the electric-resistance welded (ERW) zone, an applied cathodic potential of 100 mV accelerates crack growth significantly. Interestingly, for this microstructural region, an applied anodic potential of 140 mV has been observed to slow crack growth by an order of magnitude. (Zheng et al. 1998)

2.2.4.4. Surface Discontinuities, Inclusions and Millscale

Artificial scratches have been shown to promote SCC initiation only when oriented perpendicularly to the stress axis. (Kushida et al. 2001) No increased susceptibility to SCC initiation has been observed at other types of physical discontinuities, such as notches or dents, which are mechanically introduced to the surface of steel test specimens. (Chu et al. 2003)

Using field data, long, sulfur-containing non-metallic inclusions have been shown to increase NNpHSCC susceptibility and crack initiation. (Arrigoni and Sinigaglia 1997, Ott et al. 1992, Surkov et al. 1994) Modern line pipe steels usually have much lower levels of sulfur and other impurities. Since the mid-70s, inclusion shape has been controlled during manufacturing. Other improvements include

reduction of grain size, increased strength and toughness, and replacement of ferrite-pearlite structures by ferrite and bainitic ferrite. (Baker 2005)

Millscaled pipe surfaces are electrochemically active and were found to be catalytic towards the cathodic reduction of oxygen or water, increasing the rate of anodic dissolution at the bottom of oxide cracks. (Been et al. 2004, Qin et al. 2004) The role of millscale in SCC has been divided into three phases by Qin et al.. Initially, a positive E_{corr} potential is observed, indicating that the electrolyte is only in contact with the millscale surface and not the steel below. The reduction of water occurred an order of magnitude faster on millscale covered electrodes than on polished and cleaned electrodes. This cathode reaction was also accelerated when the cathode was a polished pre-oxidized electrode. (Kushida et al. 2001) The E_{corr} then decreases, as the steel dissolution is coupled to the reductive dissolution of millscale. The rate at which this change happens is dependent upon the CO_2 concentration of the electrolyte. Finally, the E_{corr} reaches a steady potential, as the reaction occurs between the exposed areas of steel and the electrolyte, with the millscale no longer being reduced. (Qin et al. 2004) Once the crack is deep enough, the millscale provides cathodic current to the crack tip. In other words, millscale initially acts as a cathode to help initiate cracks, and later can act as an anode to increase the cracking rate. (Been et al. 2004)

Using specimens with one side as received and the other polished to 320 grit, Kushida et al. (2001) found that cracks were more likely to initiate from machined notches on the polished side than on the millscale side. This appears to contradict the general findings that millscale accelerates the initiation and propagation of SCC, but the explanation offered by the authors is that the millscale acts to change the localized potential at the bottom of the notches. Connections can be drawn between these findings and findings by Bouaeshi et al. (2005) that after having reached a depth of about 0.5 mm, cracks tend to grow length-wise faster

than depth-wise, a phenomenon that may be due to a change in the crack environment once it exceeds a certain distance from the millscale.

2.2.4.5. Weldments

Crack colonies commonly appear near the longitudinal weld of the pipe, with one report quantifying the higher risk area as being within 100-250 mm of the weld. (Ott et al. 1992) The area near the weld differs from the bulk pipe material in both its microstructure and its residual stresses. Uneven cooling processes can introduce both tensile and compressive stresses in the heat affected zone. The different rates of cooling at locations near the weld also lead to several distinct microstructures. The differences between these microstructures can cause the evolution of microgalvanic cells promoting localized corrosion of the heat affected zone.

Of the microstructures developed near the weld, the coarse grained heat affected zone (CGHAZ) is understood to have an increased SCC susceptibility. This region has higher yield strength and hardness values than the parent material. Crack velocity in the CGHAZ has been observed to be up to twice as high as in base material under same conditions. (Harle et al. 1995) The higher susceptibility of the CGHAZ supports the observation that the occurrence of hydrogen embrittlement is higher for steels with higher yield strength and hardness. (Beavers et al. 1998A) Residual stresses in the weld region can be sufficiently relieved by shot peening to reduce, but not eliminate, the overall SCC susceptibility of this area. (Eadie et al. 2002)

The toe of the weld acts as a geometrical stress raiser, and has been shown in laboratory work and from field experience to contribute significantly to SCC failure. Hydrostatic expansion of line pipe during the manufacturing process can create compressive stresses at the weld toe, which help to mitigate the effects of the geometrical stress concentration. (Eadie et al. 2002) For weld toe cracking, stress is the key determinant and has been shown in laboratory work by Eadie et

al. (2002) to be more significant than electrochemical factors. However, the microstructural differences of the CGHAZ, as outlined above, may also support SCC in this area. (Beavers 2004)

The geometry of the weld toe has also been documented to increase the probability of NNpHSCC on PE tape wrapped pipelines because the tape frequently fails to bond to the pipe in this area, a phenomenon known as tenting. This space between the pipe surface and the tape can contain trapped groundwater and create an electrolyte environment that supports NNpHSCC. (Parkins et al. 1994)

Under both static and cyclic loading tests, material within 6 mm of the toe of the long seam weld in an X-65 line pipe steel exhibited significantly less room temperature creep than the pipe body. (Chen et al. 2001)

2.2.4.6. Manufacturing Processes

Most line pipe is either formed seamlessly by piercing hot bars of steel, or by cold forming of plate and welding a longitudinal seam by either electric-resistance welding (ERW) or double submerged-arc welding (DSAW). Most large diameter line pipe is manufactured by one of the seam welding processes. (Baker 2005)

NNpHSCC has not been correlated with a specific manufacturing process. However, there is one type of pipe that is known to exhibit a higher probability for SCC failures. That pipe is ERW longitudinal seam pipe manufactured by Youngstown Sheet and Tube during the 1950s. (NEB 1996) The weld area in this type of pipe has exhibited a higher occurrence of NNpHSCC than the base metal and than the weld regions in other pipes. Significant amounts of martensite exist in the longitudinal HAZ of this pipe and the presence of this undesirable microstructure is responsible for the increased susceptibility to cracking. Companies operating pipelines containing Youngstown pipe include special

provisions for more frequent testing and inspection of these pipe sections as part of their pipeline integrity management program.

Larger diameter pipes have exhibited a higher tendency to develop SCC colonies than smaller pipelines. (CEPA 2000) From failures, it has been observed that crack growth rates are an order of magnitude faster on large diameter lines than smaller lines, even though the lines are designed to operate at the same stresses. The reasons for this observation are not yet understood.

2.2.4.7. Summary of Metallurgical Factors

A susceptible metallurgy is one of the three necessary constituents for the development of NNpHSCC. Factors that can affect this susceptibility are microstructure, mechanical properties and surface condition.

Banded microstructures (such as pearlite) are more susceptible to NNpHSCC initiation than more uniform microstructures such as bainite or bainitic ferrite. Original millscaled surfaces initiate cracks more easily than polished surfaces. This effect could be mechanical (surface stress concentration due to roughness) or chemical (enhanced dissolution due to local strain or due to millscale chemistry). The heat affected zone surrounding a weldment on line pipe has a higher susceptibility to cracking due to residual stresses and the increased yield strength and hardness in the CGHAZ.

No correlation has been demonstrated between pipe grade or steel composition and NNpHSCC susceptibility. NNpHSCC occurrence has not been correlated with the manufacturing or welding processes used.

Surface scratches only promote SCC initiation when they are perpendicular to the largest principal stress. Long non-metallic inclusions (often manganese sulfide) on the surface of the steel and the pits created by their preferential dissolution act

as sites for crack initiation and increase the susceptibility of the steel to NNpHSCC.

2.2.5. Mechanisms of Near-Neutral pH SCC

Near-neutral pH stress corrosion cracking is described as occurring in a four stage crack growth process:

1. Development of conditions conducive to SCC
2. Initiation of cracks
3. Growth and coalescence of nearby collinear cracks
4. Coalescence of large cracks and failure, with tearing and fatigue as the dominant crack propagation mechanisms

The SCC process can be described using a schematic referred to as the "bathtub" failure model. (Wilmott and Sutherby 1998, Baker 2005)

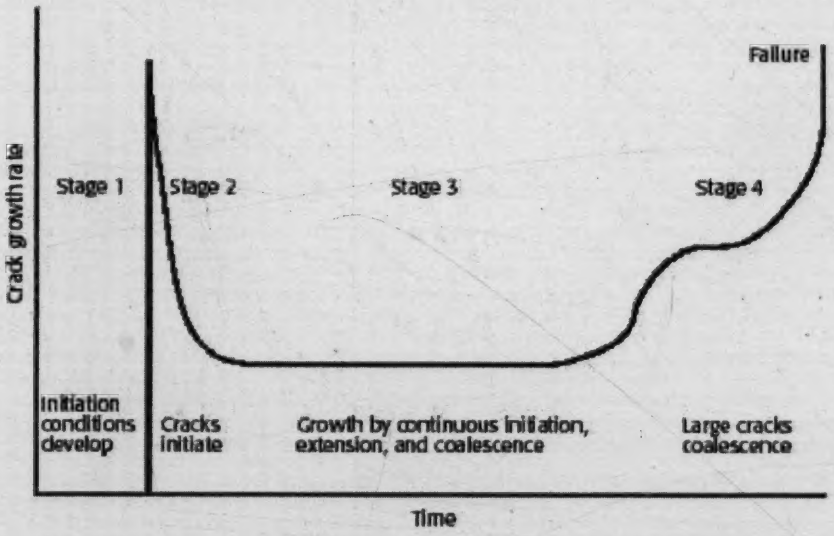

Figure 4 - "Bathtub" model of four stage crack growth process [Source: Baker 2005]

2.2.5.1. Initiation

The first stage of cracking is the initiation of microcracks. The initiation of SCC cracks depends both on the stochastic events such as the random formation of corrosion pits and on deterministic events such as the plastic strain resulting from loading conditions, and surface discontinuities. (Meyer and Pontremoli 2001)

Five early indications of likely NNpHSCC initiation are: inclusions, aligned defects, pre-existing surface defects, persistent slip bands from mechanical pre-treatment of the steel, and coating disbondment. (King et al. 2001) The first four indications in this list are all locations at which microcracks have been shown to preferentially initiate, so the presence of any of these surface characteristics may be a sign that SCC is more likely to initiate. The last item on the list, coating disbondment, is a requirement for cracks to initiate on a pipeline, because coating disbondment allows the corrosive near-neutral pH environment to contact the metal surface.

In the early stages of laboratory tests, cracks preferentially initiate at pits or inclusions. However, these cracks may tend to dormancy, and cracks formed at a later stage of the testing can become the dominant cracks which coalesce and lead to rupture. (Elboujdaini et al. 2000) The mechanism by which cracks initiate at corrosion pits is not understood, and the factors that may cause such cracks to propagate or become dormant require further research. The distinction between "pit cracks" and "non-pit cracks" in relation to probability of dormancy is important for field inspections of pipelines, but has not been explained by a cracking mechanism and hold promise for further research to improve industry's ability to identify which cracks pose a higher failure risk.

As suggested earlier, a threshold stress may exist below which NNpHSCC will not occur or continue. The stochastic nature of pitting on pipe surfaces is understood to influence the effective threshold for NNpHSCC. Cracks are more easily initiated on millscaled surfaces than on polished surfaces, a difference that is attributed to the presence of a variety of sizes and shapes of pits. However, the variation in pit characteristics necessitates a probabilistic approach to prediction of crack initiation and growth. (Parkins 1994) In a test on X65 pipeline steel, the majority of embryonic cracks stop growing before reaching a depth of 20 μm, this

may be related to the maximum pearlite band spacing measured in this metal, which is also 20 μm. (Parkins 1998A)

Stress levels are directly related to crack initiation. Higher stresses in steel specimens are associated with higher density colonies of cracks and with faster initiation rates. (Elboujdaini et al. 2000, Lu et al. 2002) The density of cracks within a colony affects the tendency of the colony to grow or become dormant. Colonies of stress corrosion cracks can be classified as dense or sparse. Dense colonies have spacing between cracks that is less than 20% of the pipe wall thickness, and sparse colonies are those with greater crack spacing. (Leis and Colwell 1997) Although most cracks become dormant before growing to a critical size for failure, sparse colonies have been shown to have a greater tendency than dense colonies to avoid dormancy and grow to failure. Additionally, nearby sparse patches can reactivate cracking in a dormant sparse patch. (Leis and Colwell 1997)

Table 5 – Dormancy of Sparse and Dense Crack Colonies

Density of Colony	Dense	Sparse
Depth of cracks	Shallow	Deep
Crack growth	Tend to dormancy	Grow to failure

These observations suggest that while a higher stress acts to initiate cracks more quickly and in denser groups, the higher stress level may actually result in a decreased chance of pipe failure. Most research into the effects of stress on NNpHSCC without evaluating colony density has produced contradictory conclusions to this work. That is, a higher stress increases the probability of cracks growing to rupture. However, it is widely agreed that the amplitude of the stress variation is more important to crack propagation than the magnitude of the maximum stress.

2.2.5.1.1. Pre-cyclic Fatigue

As discussed in Section 2.2.3.1, crack initiation is greatly aided by fatigue prior to corrosion exposure. This "pre-cyclic loading" would be likely to occur in pipes that serve for years before coating failure occurs. (Chen et al. 2003, Wang et al.

2000) In this section, the proposed mechanism by which pre-cyclic loading promotes initiation is described.

Cyclic loading or other processes that accumulate dislocations along a line have been shown to produce mechanically small cracks that are appropriate for use as starter cracks for laboratory investigations. (King et al. 2001, Elboujdaini et al. 2000) At least one study has specified that cathodic conditions of -790 mV SCE were required in order to observe this micro crack initiation as a result of prior cyclic loading, and that when the tests were performed at open circuit potential, no micro crack formation was observed during the 10 day test period. (Wang et al. 2000)

Although crack initiation is generally understood to be a continuous process, a sharp increase in the number of cracks on a surface can occur after a certain number of load cycles. (Wang et al. 1999) Further research is needed to provide an understanding of this behaviour.

2.2.5.1.2. Localized Surface Plasticity

SCC initiation of microcracks is sometimes observed on {111} slip planes. This has been proposed to be explained by a combination of plastic slip, film rupture, anodic dissolution at film rupture sites and localized surface plasticity. (Jones 1996)

2.2.5.1.3. Corrosion Pits and Surface Discontinuities

The dilute ground water solution associated with near neutral pH stress corrosion cracking does not enable the metal to form a passive film. In this environment, corrosion pits form on the metal surface, and some pits initiate cracks. Since passivation does not occur, corrosion of the crack walls also occurs. For a crack to propagate, it is proposed that the rate of crack growth must be several times faster than the rate of pit growth, and that the rate of growth at the crack tip must be significantly faster than the rate of dissolution along the crack walls.

The stress concentrations at corrosion pits and surface discontinuities are said to help achieve the necessary conditions for crack initiation. Pits develop a localized electrolyte environment that is typically more corrosive than the bulk solution. The coexistence of corrosion pitting and NNpHSCC does not necessarily indicate that dissolution is the mechanism of SCC propagation. It is not yet well understood if pits advance SCC by allowing changes to the local electrolyte environment (Parkins 1982) or if pits accelerate SCC primarily by a stress raising action.(Surkov et al. 1994, Zheng 2001) Precise determination of the environment within a corrosion pits and micro-cracks would provide further insight into the mechanism by which pits can lead to SCC initiation. (Meyer et al. 2003)

In work by Lu et al., a categorization of cracks as pit or non-pit cracks was proposed. Non-metallic inclusions are more anodic than the metal surface, and corrode readily to form pits. For surfaces with a low density of non-metallic inclusions, the majority of cracks that initiate are non-pit cracks. (Lu et al. 2002)

2.2.5.2. Propagation

The propagation of near-neutral pH stress corrosion cracks has been studied much more extensively than the initiation of these cracks, yet the mechanism of propagation is not yet fully understood either.

Laboratory work has made it clear that the initial cracking stage of NNpHSCC is driven by a dissolution mechanism and is independent of applied stress level.(Lu et al. 2002, Chen et al. 2002B) The current understanding is that another mechanism is operative after the initial dissolution process. Both field experience and the results of laboratory studies provide evidence that this mechanism is hydrogen-based, but its details are not well understood. (King et al. 2000)

In the final stage of crack propagation, a hydrogen-enhanced form of corrosion fatigue is credited as the active mechanism. However, this transition from the initial cracking stage, driven by dissolution, to the final cracking stage, driven by corrosion fatigue, is unclear. There must be a mechanism other than corrosion fatigue to grow SCC cracks to a critical size beyond which corrosion fatigue can occur as the dominant propagation mechanism. (Eadie et al. 2005C)

NNpHSCC resembles corrosion fatigue of high strength steels in some ways. The features of short individual near neutral pH stress corrosion cracks suggest a mixed mechanism of stress corrosion and corrosion fatigue. (Meyer et al. 2003) In corrosion fatigue there is a ΔK threshold below which cracks do not propagate, and a similar threshold stress intensity has been identified in some NNpHSCC research. (Beavers 2004)

2.2.5.2.1. Dormancy

More than 95% of cracks in SCC colonies found in the field are dormant (Delanty and O'Beirne 1992) with a blunt tip and are less than 1 mm in depth. (Fessler and Krist 2000) Dormant cracks are those that are not growing or are growing very slowly (10^{-9} mm/s). However, a crack that is growing at a rate slow enough to be considered dormant can still pose a threat to long-term pipeline integrity. A crack growing at $5x10^{-9}$ mm/s would reach ⅓ of the wall thickness in roughly 20 years. (Chen et al. 2002B)

It has proven difficult to grow cracks in the laboratory using stressing that is representative of field service conditions. Lab simulations with realistic loading often generate only "microstructurally short cracks" which become dormant before they become "mechanically short cracks" to which fracture mechanics analysis can be applied. (Van Boven 2003, Elboujdaini et al. 2000)

Dormancy is a complicated issue involving factors including stress transients, electrolyte composition, and crack tip strain rate (which is dependent upon R-

value and frequency). (Beavers 2004) The variation of cracking with chemistry of the environment is important in understanding whether cracks go dormant. (Eadie et al. 2005C)

In dormant cracks, walls are typically corroded and the crack tip is blunted. A dormant crack can continue to corrode along its flanks, causing further blunting and decreasing the probability of re-activation. (Beavers 2004)

Unload-reload transients can accelerate or re-initiate cracking; this phenomenon merits further study. In a similar vein, it appears from examination of circumferential crack surfaces that these cracks experience periods of growth separated by periods of dormancy. (Beavers 2004)

It was previously thought that crack coalescence was important in relation to dormancy. An active crack can coalesce with a dormant crack and cause it to resume propagation. However, recent work has found that coalesced cracks tend to stop growing in the depth direction. (Chen et al. 2002B) Linked cracks are less likely to grow to failure than are independent cracks. (Bouaeshi et al. 2005)

A possible relationship between stressing ratio and the onset of dormancy has been investigated. At high frequencies (10^{-2} Hz), the R-value does not appreciably affect the time to dormancy as calculated in work by Beavers, but at lower frequencies (10^{-5} Hz), higher R-values were observed to decrease the time to dormancy. (Beavers 2004)

2.2.5.2.2. Dissolution

While anodic dissolution is known to play a role in NNpHSCC, the cracking cannot be attributed to dissolution alone. Rates of crack propagation measured in laboratory tests are too high to be explained by the rate of dissolution alone, as calculated using Faraday's law (Section 2.2.5.3.1).

Several mechanisms used to explain high pH SCC rely on dissolution models. These include the active path mechanism and the film rupture mechanism. Since a passive film does not form on the metal surface in near-neutral pH conditions, the film rupture mechanism cannot be proposed to explain NNpHSCC. The active path mechanism proposes that there are pre-existing paths in a metal that will be preferentially corroded, thereby directing and supporting the propagation of the stress corrosion cracks. This mechanism relies on the lower electrochemical potential of grain boundaries, pile-ups of dislocations and segregated second phases (including weld HAZs) and cannot be used to explain the transgranular nature of NNpHSCC.

2.2.5.2.3. Hydrogen

As stated above, it is believed that NNpHSCC propagates in three stages: an initial mode driven by dissolution, a transition that is not well understood, and a final mode driven by corrosion fatigue. There is evidence that hydrogen plays a role in all three stages of cracking. During NNpHSCC, evolution of atomic hydrogen occurs by the cathodic reaction and this hydrogen can diffuse into the steel around a crack. (Gu et al. 1999B) Hydrogen diffuses more easily into stressed metal and also migrates to areas of higher hydrostatic stress within the steel. Chen et al. showed that the hydrogen permeability of X-70 steel increased when loaded to more than two-thirds of its yield strength. (Been et al. 2004)

The main indicators of the involvement of hydrogen in stress corrosion cracking are quasi-cleavage crack appearance and hydrogen permeation tests in groundwater solutions.(Zheng et al. 1996A, Been et al. 2004) The quasi cleavage fracture surfaces indicate the involvement of a decohesion mechanism in the growth of stress corrosion cracks.(Parkins 1999B) The Griffith equation can be used to illustrate the decohesion model of hydrogen induced cracking (HIC). (Parkins 1998A)

SSRT tests, as described in Section 2.2.6.2, are frequently used to evaluate a material's resistance to environmentally assisted cracking (EAC) as reflected by the %RA upon failure. A decrease in the %RA upon failure has been definitively linked to the rate of hydrogen absorption into the steel. Experiments involving pre-charging a specimen with hydrogen prior to SSRT have provided valuable information about the role of hydrogen in NNpHSCC. Tests of hydrogen pre-charged steel in air did not show the same loss of ductility as the tests conducted in a hydrogen-charging electrolyte such as NS4 with CO_2 sparging gas. (Parkins 1999B) Hydrogen pre-charging has also been observed to increase the anodic dissolution rate and thereby promote NNpHSCC.(Gu et al. 1999A, Gu et al. 1999B) Hydrogen pre-charged specimens tested in the near-neutral electrolyte displayed increased severity of the resulting SCC, providing convincing evidence that hydrogen plays a role in NNpHSCC, by reducing ductility, accelerating dissolution or both. (Fessler and Krist 2000, Parkins et al. 1994)

SSRT results have shown that hydrogen in the metal decreases its ductility significantly but does not affect its strength. Tests carried out in "heavy water", D_2O, have been used investigate the role of hydrogen diffusion in NNpHSCC. The atomic deuterium that enters the metal has a much lower diffusivity than the atomic hydrogen that exists in tests carried out in regular water. The SSRT results in D_2O showed a lower influence of environmentally assisted cracking (EAC) in the failure of the specimens. These findings support the assertion that the diffusion of hydrogen to the cracking area may be responsible for loss of ductility in the steel. (Been et al. 2004)

Cyclic loading experiments conducted in an NS4 solution made with heavy water showed that crack growth rates were lower in D_2O than in H_2O, suggesting that the presence of hydrogen affects crack growth over the entire regime of test conditions. (Been et al. 2004)

Blistering of trapped hydrogen has been established as a failure mechanism in other forms of EAC, but has been ruled out as a mechanism for NNpHSCC. At a typical cathodic potential, the concentration of diffusible hydrogen in various soil environments is only ~10% of the minimum required for blistering. (Chen et al. 2000) Similarly, in Devanathan cell hydrogen permeation tests performed by Kushida et al., the measured hydrogen content in the steel was much lower than the threshold for hydrogen embrittlement, which requires at least 0.1 ppm hydrogen. (Kushida et al. 2001) These results may suggest that the initiation of cracks by hydrogen would involve different HE mechanisms such as hydrogen-induced localized plasticity or reduction of lattice cohesive strength.

The presence of carbon dioxide in the test solution has a strong effect on the environment pH. In tests of API X-52, X-60 and X-65 pipeline steels, the sub-surface hydrogen concentration was affected more by variations in the carbon dioxide content of the electrolyte than by any differences between the steels tested. (Parkins 1999B) Higher CO_2 concentrations have been demonstrated to promote the entry of hydrogen into the steel.

Tests investigating the role of hydrogen in NNpHSCC have been carried out at a range of potentials. At potentials near E_{corr}, the cracking is thought to be dominated by a hydrogen enhanced anodic dissolution mechanism, but below a certain cathodic potential, cracking appears to by driven by hydrogen induced cracking. (Gu et al. 1999B)

While the modelling of crack tip chemistry, stress, diffusion and hydrogen concentrations have progressed to a level of sophistication that enables quantitative comparison of different proposed SCC mechanisms, the validation of an applicable failure criterion for the stress corrosion brittle fracture of ductile materials lags behind. (Delafosse and Magnin 2001)

It has been proposed that the propensity of a metal to HIC depends on the density of trap sites. However, experimental SSRT data from work carried out by Parkins, indicates that fracture is not dependent on the presence or concentration of hydrogen in irreversible traps. (Parkins 1998A) Specimens that were charged with hydrogen and then stored for 6 days so that only irreversibly trapped hydrogen would be present exhibited the same reduction in area during SSRT in air as specimens that had not been charged. Yet, in this same work, hydrogen permeation tests on samples of pipeline steel that had been in service found no evidence of trap filling between successive tests, indicating that the traps were already filled in the as-received steel. Thus, the relation between trap density and NNpHSCC is uncertain.

2.2.5.2.4. Room Temperature Creep

Pipeline steels normally exhibit about 1% static room temperature creep in air when subjected to stresses below the yield point. This creep is exhausted within hours. However, when steels are cyclically loaded at R = 0.1, room temperature creep is restored and strain can be increased to the range of 2%. (Wang and Chen 2002, Chen and Wang 2002)

Cyclic loading does not always produce enhanced room temperature creep; the sequence of loading events is important. When cyclic loads are applied after static creep is exhausted, the resulting creep is limited. On the other hand, when static loads are applied after cyclic creep loading, a burst of creep deformation is observed after an incubation time that is dependent on the number of prior load cycles. (Chen and Wang 2002) The amount of creep strain that occurs in this burst increases with the number of prior load cycles up to a peak at 1000 cycles, after which point, the magnitude of the creep burst declines. (Wang and Chen 2002)

This behaviour could be used to explain the large effect that previous fatigue loading can have on SCC initiation, and could affect crack propagation as well.

(Wang and Chen 2002) As a preventative or mitigative measure for in-service pipelines, room temperature creep could be used to cause crack tip blunting. By exhausting creep at stresses just above operating levels, the crack tip stresses and residual internal stresses would be relaxed and crack progression would be expected to slow for some period. This understanding of room temperature creep could also be used in new pipelines to relieve residual stresses before putting them into service. (Chen and Wang 2002)

2.2.5.3. Crack Growth Models

The method of crack growth in NNpHSCC is understood to be complex. Many proposed mechanisms of propagation are still being studied. While the mechanism of crack growth is not yet understood, it is known that a critical balance of environmental corrosivity and mechanical loading must be maintained for crack growth to exist and continue. (Wang et al. 1999) A number of models, both empirical and theoretical, have been formulated to describe the behaviour of NNpHSCC. Several of these models are introduced here.

2.2.5.3.1. Faraday's Law

Faraday's Law quantifies the rate of material corrosion in terms of the measured corrosion current.

$$Corrosion\ rate = \frac{i_{corr}}{nF} \tag{5}$$

where i_{corr} = the corrosion current density [A/m^2]

n = the valence of the metal ions produced from dissolution

F = Faraday's constant, 96,490 C/mole e^-

Many tests have measured the corrosion current density in a NNpHSCC system, and found that Faraday's law cannot be used to predict crack growth rates observed in laboratory tests or field experience. (Parkins 1998A, Parkins 2000) Observed crack velocities are significantly higher than predicted by this model.

The role of hydrogen in NNpHSCC may account for the difference between growth rates calculated using Faraday's law and those observed in field and laboratory work. (Parkins 1999B)

2.2.5.3.2. Paris Model

Some researchers have adopted a corrosion fatigue approach in their analysis of SCC test data, reflecting the perception of the role of cyclic loading in the propagation of cracks. (Zhang et al. 1999, Shipilov 2002) It is currently thought that the final stage of crack propagation is driven by a hydrogen-enhanced form of corrosion fatigue, particularly in oil pipelines, which experience larger amplitude stress cycles.

The Paris model is used to describe fatigue crack propagation. It relates the rate of subcritical crack growth to the amplitude of the stress intensity factor under a fatigue stress regime. (Paris and Erdogan 1963)

$$\frac{da}{dN} = C_f \cdot \Delta K^m \tag{6}$$

where da/dN = the crack growth per stress cycle

ΔK = the amplitude of the stress intensity factor over the stressing cycle

C_f = the crack propagation fatigue coefficient, a material property

m = the crack propagation fatigue exponent, a material property

Researchers have had limited success in fitting the Paris model to NNpHSCC behaviour. The stress intensity factor, K, is only valid for elastic conditions. Significant plasticity at the crack tip makes the stress intensity factor an inappropriate mechanical descriptor of the fracture conditions. (Zheng et al. 1996B)

In one investigation, an indication was found that critical values of K_{max} and da/dN may exist and affect crack growth rates. (Shipilov 2002) When K_{max} and

da/dN were above critical values, cathodic polarization was observed to accelerate crack growth rates. The same cathodic polarization would either slow down or have no effect on crack growth rates when K_{max} and da/dN were not above the critical values. Fractographic examination suggests that the accelerated crack growth was due to hydrogen induced cracking.

2.2.5.3.3. Superposition

It has been proposed that crack growth can be modeled as the superposition of fatigue crack growth in air and SCC crack growth at constant load. (Zhang et al. 1999, Lambert and Sutherby 1998, Lambert et al. 2000A, Lambert et al. 2000B)

$$\frac{da}{dN}(total) = \frac{da}{dN}(fatigue) + \frac{1}{f}\frac{da}{dt}(scc) \quad (7)$$

The value for SCC crack growth at constant load, $da/dt_{(scc)}$, is difficult to accurately identify, as it is based on a number or parameters, many of which are not yet fully understood. Laboratory investigations of NNpHSCC have encountered significant difficulty in creating SCC under static loading conditions. In a series of tests using samples of line pipe steels with starter cracks, carried out in soil boxes with NS4 solution, crack growth rates between $1.5x10^{-9}$ mm/s to $2.94 x10^{-8}$ mm/s have been measured. (Wilmott and Sutherby 1998) From data fitting, a reasonable value for da/dt has been estimated as $3x10^{-9}$ mm/s for near-neutral pH conditions. Present understanding of NNpHSCC growth suggests that the crack growth observed in these tests was dominated by anodic dissolution of blunt starter cracks. Significantly different crack growth behaviour is observed for short, starter cracks than for long cracks. Starter cracks can be observed to grow under constant loading and at faster crack growth rates than typical of longer cracks.

To evaluate the validity of the superposition model, it has been compared to experimental results. Data from laboratory tests conducted at University of Waterloo and CC Technologies were compared to the proposed superposition

model (Lambert et al. 2000A), and were found to be consistent with the model although there was considerable scatter in the data. It has been suggested by other researchers that the extent of the scatter in experimental data makes it hard to judge the validity of the proposed correlation. (Beavers and Jaske 2000)

The test performed at Waterloo used edge notch bending specimens while those at CC Technologies used compact tensile (CT) specimens. The CT specimens were measured to have growth rates from the static SCC component of the superposition model that were an order of magnitude faster than those calculated for the edge notch bending specimens. This difference could be attributed in part to differing measurement techniques used to track crack growth (photomicrographs and direct current potential drop method (DCPD) at Waterloo and CC Technologies respectively). The remaining differences in crack growth may have been due to differences in crack orientation, with the bending specimen type growing through thickness cracks and the CT specimen creating crack growth primarily along the surface of the metal.

Beavers and Jaske (2000) modified the proposed NNpHSCC superposition model equation by replacing the term representing fatigue crack advance with a term representing corrosion fatigue and saw an improved fit of the experimental data to the model.

Models for proximity, stress shielding and crack coalescence have been incorporated in work done to evaluate the superposition model and have resulted in reasonable, if simplified, predictions of crack colony behaviour.(Lambert and Sutherby 1998, Lambert et al. 2000B, Lambert 2000) Further work to improve this model is proposed to include sensitivity analyses of the constants empirically fitted to the equations, and incorporation of residual stresses in the pipe material. (Lambert 2000) The representation of the SCC component of crack growth rate as a time-constant value over a number of years of the numerical simulations is

another factor in this model that has potential for improvement and refinement. (Lambert and Sutherby 1998)

2.2.5.3.4. J- Integral

Many attempts have been made to relate the crack growth rate with engineering parameters. As already addressed, the stress intensity factor, K, is a simplified representation of the stress condition at the crack tip that assumes linear elastic material behaviour. To attempt to include plastic effects in the fracture mechanics analysis of the stress corrosion cracks, the J-integral has been used in modelling crack growth.

The J integral is a fracture mechanics parameter used in elastic-plastic materials such as line pipe steels to describe the driving force for crack propagation. (Beavers and Jaske 1998) It can be defined using the rate of energy absorption during crack growth. (Harle et al. 1995)

$$J = \frac{1}{B}\frac{dU}{da}\bigg|_{v=constant} \quad (8)$$

where J = the work required to grow a unit area of crack

B = specimen thickness

U = energy under the load-displacement curve

a = crack length

v = displacement of the applied force

At any point on the load-displacement curve, the J-integral can be calculated as the sum of its elastic and plastic components, J_{el} and J_{pl}. The elastic component is proportional to K^2/E where K is the stress intensity factor used in linear elastic fracture mechanics and E is the Young's modulus of the material. The plastic component, J_{pl}, is proportional to the plastic area under the load-displacement curve. (Beavers and Jaske 1998)

Under steady state cyclic loading, Beavers and Jaske (1998) observed no correlation between the applied J-integral and the cracking velocity. Another research effort in this area has correlated crack velocities with the time rate of the J-integral. (Wilmott et al. 1996, Beavers and Hagerdorn 1996) A full-scale SCC test at CANMET showed clearly that a crack in a near-neutral pH environment would become dormant if the pressure fluctuations were stopped. This study also found a linear relationship between crack growth rates and $\Delta J/\Delta t$ on a log-log scale. (Zheng et al. 1996A, Zheng et al. 1996B) A quantitative expression for this relationship is (Zheng 20-01):

$$\log(\frac{\Delta a}{\Delta t}) = k \log(\frac{\Delta J}{\Delta t}) + c \tag{9}$$

Another full-scale test for the Corrosion Committee of PRCI limited analysis to the LEFM level, so that K and ΔK were the crack tip stress descriptors. (Zheng et al. 1998) In the linear-elastic region, the J-integral and stress intensity factor can be related by the material's modulus of elasticity.

$$\Delta J = \frac{(\Delta K)^2}{E'} \tag{10}$$

$$\frac{\Delta J}{\Delta t} = \frac{(\Delta K)^2}{E' \Delta t} \tag{11}$$

A linear trend was found between ΔK and crack velocity at low stresses, but for larger stress intensity levels causing excessive plastic deformation the data shifts away from linear behaviour. The physical significance of this relationship is that the growth rate depends on the rate of increase in crack tip opening displacement (CTOD, or δ). For most J-integral values, crack rates decrease as displacement rates decrease, but at J-values typical of field data, crack rates have been measured to be independent of displacement rates. (Harle et al. 1995)

The CTOD time rate, $d\delta/dt$, is a mechanical parameter to describe the crack propagation. It is useful in the assessment of critical flaw sizes and stress. (Zheng

et al. 1996A) The dependence of SCC on crack tip opening rates is due to the impact on dissolution rate, film rupture strain rate and crack tip strain rate. (Zheng et al. 1996B) The CTOD rate has been related to the J-integral time rate.

$$\dot{\delta} = \frac{d\delta}{dt} = \frac{d_n}{\sigma_{ys}} \frac{\Delta J}{\Delta t} \tag{12}$$

where δ = the crack tip opening displacement.

d_n = a constant for the given constraint, determined by the yield stress and the strain hardening coefficient of the material

σ_{ys} = the material yield strength

Observations from this work suggest that there may be a threshold $\Delta J/\Delta t$ that must be exceeded in order to cause crack growth. (Zheng et al. 1996A)

2.2.5.3.5. Coalescence

Most cracks tend to dormancy soon after nucleation, but it appears that the initiation of new cracks nearby can cause coalescence with, and reactivation of, these dormant cracks. (Parkins and Singh 1990) Both co-planar and non co-planar cracks may coalesce, by modes I and II. Non-planar crack coalescence has been experimentally observed to occur as two slightly misaligned cracks growing so that their tips pass each other for a small distance before turning and growing towards each other. (Parkins and Singh 1990) Coalescence requires that the involved cracks be close enough to interact. Since crack density is known to increase with time, the frequency of coalescence can also be expected to increase with time. (Parkins and Singh 1990) The maximum out of alignment distance (y) between a crack and other surrounding cracks that will still permit their coalescence has been expressed by Parkins and Singh (1990) as:

$$y = 0.025mm + 0.14(2a) \tag{13}$$

where 2a = the crack length in mm

Although crack coalescence can extend the effective size of a stress corrosion crack and has been observed to cause reactivation of dormant cracks, there are several reasons that crack coalescence is not thought to be the mechanism of failure in NNpHSCC.

It has been indicated that crack coalescence does not increase crack depth appreciably, although it does increase the effective length of the cracks. After they reach a depth of approximately 0.6mm, the cracks tend to widen, become blunt and fill with corrosion products. Individual cracks, on the other hand, show a linear relationship between depth and length. (Chen et al. 2002B)

In colonies where coalescence has been observed to contribute to crack growth, the final failure stage was dominated by crack growth in the depth direction, not by further coalescence along the pipe surface. (Ott et al. 1992)

Crack colony geometry affects whether near-neutral pH stress corrosion cracks coalesce or grow to failure. The interaction of stress fields created by adjacent cracks may actually reduce crack driving force. (Beavers 2004) This is referred to as stress shielding, and may explain why dense crack colonies tend to dormancy more often than do sparse colonies. Additionally, colonies that are long in the longitudinal pipe direction and narrow in circumferential direction are more risky. For colonies that are equally long and wide, growth mainly occurs at the edges of the colony while cracks near the center of the colony are shielded from stress and become dormant. (Baker 2005)

2.2.5.3.6. Combined Probabilistic Pitting and Crack Growth Model

The initiation and growth of NNpHSCC has been modeled by Zhang et al. (2000A, 2000B) using a thermodynamic crack growth model combined with a finite element crack interaction model. This work aims to model the combination of probabilistic and deterministic events that lead to the development of an SCC

colony. The model creates pits randomly on the surface, and based on a random probability, some of these pits initiate cracks. Individual crack growth is modeled using a combination of hydrogen diffusion and corrosion rates with corresponding thermodynamic forces. The interaction of these individual cracks is addressed with a finite element simulation of multi-crack cluster formation within SCC colonies.

2.2.5.4. Summary of Near-Neutral pH SCC Mechanisms

It is difficult to differentiate between the relative roles of corrosion processes and hydrogen on crack growth. (Been et al. 2004) A number of mechanisms have been proposed to explain the propagation of cracks, and models have been created to relate observed growth to measurable engineering parameters. However, the mechanism of NNpHSCC is still not known, as proposed mechanisms require further research or have fallen short in their ability to explain cracking behaviour. The models to quantify crack growth rates hold promise in their correlations with experimental data, but further development work is needed in this area as well.

2.2.6. Near-Neutral pH SCC Investigation Methods

Near-neutral pH SCC is studied using both laboratory methods and field research. Some common methods are described below.

2.2.6.1. Field Research Methods

Extensive pipeline integrity management programs have been implemented by pipeline operating companies to reduce the likelihood of future leaks or ruptures due to NNpHSCC among other pipeline integrity risks. The main goal of this work is to ensure pipeline safety, not to research NNpHSCC. However, the data collected through this work is compiled and used to improve the understanding of this cracking phenomenon.

Testing of pipelines includes hydrostatic testing and in-line investigation, as well as direct examination methods that require excavation of the pipeline. This latter category includes inspection techniques such as visual, magnetic particle, liquid

penetrant, eddy current, ultrasonic shear wave, potential drop, and alternating current field measurement.

The findings from this work are used to create predictive models and site selection models, which aim to identify high risk areas for NNpHSCC. These models help pipeline operators to select pipe sections for excavation and inspection. This is an iterative process; as more excavations are completed, the predictive model can be refined.

Field research also includes pressure monitoring and detailed study of NNpHSCC colonies found on in-service pipelines. CEPA collected pressure data from a number of oil and gas pipelines and summarized the data in a format useful for the design of stressing conditions in laboratory investigations of NNpHSCC. (Sutherby et al. 2000) Several studies have been conducted to characterize crack colonies developed in the field. (Jack et al. 1999, Bouaeshi et al. 2005, Leis 1996) This work allows laboratory researchers to evaluate the cracks generated in their tests in comparison to field cracks.

2.2.6.2. Lab Investigation Methods

Laboratory techniques to reproduce and study SCC have been developed in response to the integrity threat to pipelines posed by this form of cracking. These methods have been extended to use in studies of other alloy/environment combinations. Most test techniques simulate all three necessary components of an SCC system: susceptible metallurgy, potent cracking environment, and sustained static or cyclic tensile stress. Some techniques omit the stressing component, and are aimed at evaluating only environmental or electrochemical aspects of the stress corrosion cracking. The former type of test is referred to as a mechanical test, and the latter is called an electrochemical test. Common NNpHSCC test techniques in these two categories are listed in Table 6 and several are described in more detail below. (Sedriks, 1990)

Table 6 – Common Mechanical and Electrochemical NNpHSCC Laboratory Test Techniques

Mechanical Test Techniques	Electrochemical Test Techniques
• Slow Strain Rate Test (SSRT) • Tapered Tensile Test (TTT) • Curved Cantilever Beam Test (pre-cracked and smooth) • ½ T – CT Specimen Test • Four Point Bending Test • (constant load, C-ring, U-bend, WOL)	• Potentiodynamic and Potentiostatic Polarization Test • Devanathan-Stachurski Hydrogen Permeation Test

The slow strain rate test uses a cylindrical tensile specimen and subjects it to a slow, constant rate of strain while exposed to the test solution. This is a severe test that guarantees failure within a relatively short test time. It can be used to differentiate the aggressiveness of environmental conditions (solutes, electrochemical potential, dissolved gas concentrations) to near-neutral pH SCC of metals by comparison of the ductility, measured as the reduction in cross-sectional area achieved before final fracture (%RA). (Beavers et al. 1998A, Chen et al. 2002A)

Traditional SSRT do not offer enough sensitivity or control of loading conditions, and so a slow strain rate test technique using pre-cracked compact specimens was developed. (Beavers et al. 1998A) Pre-cracked SSRT specimens typically exhibit a crack growth rate in near-neutral pH conditions that are several orders of magnitude faster than estimated from field observations. (Beavers and Jaske 1999) This could be due to the severe loading conditions used in this test technique. Cyclic loading is generally approved of as a more accurate stressing technique to reproduce the NNpHSCC cracking observed in service conditions.

Constant extension rate tests (CERT) use the same loading conditions as SSRT, but the test specimens for this test method are cold worked with a crimped section

in the middle, which introduces a localized strain concentration. The scatter in crack initiation results is reduced by the strain concentration since cold work and plastic strain are both accelerating factors for stress corrosion cracking. (Rebak et al. 1996)

Many tests, including those on ½T-CT, 4 point bending, smooth tensile or notched tensile specimens, use a cyclic loading profile to stress the specimen. The amplitude of the stress cycle has been found to have a more significant effect on cracking than the magnitude of the maximum stress in the cycle. Other important factors in the design of the stress cycle and their effects on cracking have been documented.

Lower crack velocities were observed for trapezoidal waveform loading than for triangular waveform loading in work by Beavers & Jaske (1998). However, it was noted that this effect may have been within the experimental variation, and should be confirmed with further testing.

Cyclic load tests that were interrupted at several stages during the test to assess the crack progress actually exhibited higher crack growth rates than continuous tests. (Rebak et al. 1996) This may be attributed to the unload-reload transient, which can re-activate dormant cracks, or to environmental effects caused by removing the specimen from the test solution for a short time.

It is common in crack propagation experiments to measure crack length by direct current potential drop (DCPD). This technique is not suitable for initiation experiments, experiments on crack colonies, or for cracks that undergo considerable branching. When crack growth is very slow, experience has shown that this method of crack growth measurement can be unsuitable because of a lack of sensitivity or resolution. (Lambert et al. 2000B) A constant test environment temperature is needed to ensure accurate DCPD readings. A variation of even 1 degree Celsius can compromise the reliability of the data. Measurement of crack

length by DCPD is better suited to NNpHSCC than high-pH SCC because the higher frequency of crack branching in high-pH SCC reduces the accuracy of the measurements obtained. (Beavers and Jaske 1999)

Electrochemical test techniques include polarization tests and hydrogen permeation tests. Potentiodynamic polarization tests scan the electrode potential of a specimen at a constant rate, while monitoring the resulting current density. This test method can be used to determine the expected corrosion behaviour of a metal in a corrosive environment. (Beavers and Jaske 1999) Potentiostatic polarization tests hold the metal potential at a constant value, usually for one to two days. The current density on the metal surface is measured as a function of time. After the test, the specimen surface is examined to characterize the oxide film that has formed. (Beavers and Jaske 1999) In NNpHSCC, active corrosion is normally observed, rather than the surface passivation associated with high pH SCC. Therefore, potentiodynamic and potentiostatic polarization test techniques, which investigate passivation behaviour, have been found to be of limited use in studying NNpHSCC.

Hydrogen embrittlement is thought to play a role in NNpHSCC, and hydrogen permeation test are often performed with NNpHSCC alloy/environment combinations to investigate this mechanism.

The Devanathan-Stachurski technique is well established as a means for measuring hydrogen permeation. The test set-up consists of a two-compartment test cell with the metal sample separating the two compartments. Hydrogen is generated by electrochemical reactions at the metal surface on one side of the cell, the hydrogen diffuses through the metal and is oxidized at the metal-electrolyte interface on the other side of the cell. The rate of hydrogen permeation can be determined by measuring the current on the oxidizing side of the cell using Faraday's law. (Beavers and Jaske 1999)

It has proven difficult to obtain accurate and reproducible data when studying NNpHSCC. Both field and laboratory data frequently show considerable scatter and limited reproducibility. Even under carefully controlled experimental conditions, lifetimes of specimens can vary by an order of magnitude. This experience indicates the probabilistic nature of NNpHSCC processes including pitting, initiation and coalescence, and underscores the difficulty in predicting the life expectancy of field pipes with SCC colonies. (Parkins 1996B) Appropriate statistical methods are therefore advisable in the collection and analysis of laboratory data relating to near-neutral pH SCC.

2.3. Pits and Crack Initiation

2.3.1. Pits as Crack Initiation Sites

Evidence from field failures and laboratory studies suggests that corrosion pits might be the most common site for crack initiation and that pitting generally precedes crack initiation. The initiation and early growth stages may account for up to 90% of the time to failure in NNpHSCC (Parkins and Delanty 1996).

Work investigating the initiation of NNpHSCC has been conducted using original pipe surfaces, (Parkins and Delanty 1996, Bouaeshi et al. 2005) chemically cleaned surfaces, and polished surfaces (Wang et al. 1998A, Wang et al. 1998B, Chen et al. 2003). These studies have all indicated that the majority of cracks are associated with surface pits, and thus that pitting typically precedes crack initiation.

Figure 5 - Crack in a near-neutral pH SCC colony that developed in service on a liquid pipeline

2.3.2. Existing Criteria for Pit-to-Crack Transitions

A criterion for the onset of stress corrosion cracking from pits has not yet been proven or widely accepted. (Turnbull 2000) A number of conditions for crack initiation have been formulated and studied. Kondo's critical pit depth formula proposes that the pit to crack transition occurs when the crack rate exceeds the pit rate (Kondo 1989). Lian and Meletis (1996) propose that hydrogen enhanced localized plasticity creates large strains in a small near-surface volume, and that the material in this region begins to crack at the same fracture strain as observed in bulk specimens without hydrogen effects. In comparison to other crack initiation models, this criterion has the advantage of explaining the observed influence of hydrogen on crack initation.

2.3.3. The Role of Stress in Crack Initiation

Experience from laboratory studies indicates that NNpHSCC cracks require some stress fluctuation, even minor, in order to initiate and grow (Wilmott and Sutherby 1998; Beavers and Hagerdorn 1996). The sources of stress can be classified as operational (from internal pipeline pressure) and secondary (including localized bending or tension, or residual stresses). Much of the laboratory work that has been done to study the factors causing NNpHSCC has used large stress fluctuations, with R-values of 0.5 or 0.6. These stress variations are much more severe than those typically experienced by a gas pipeline in service (Sutherby et al. 2000) but may be appropriate for oil pipelines. In the case of NNpHSCC on

gas pipelines, the stress fluctuations commonly used in laboratory testing likely introduce a disproportionate role of fatigue into the laboratory crack initiation results.

Measurements of residual stress on sections of pipe taken from service have varied from tensile stresses in the range of 29% SMYS to compressive stresses of 77% SMYS. The region near the weld toe shows primarily compressive residual stresses, whereas other locations on the circumference exhibit residual stresses that are mainly tensile (Roy et al. 1993; Eadie et al. 2002). These residual stresses can have a marked effect on the stress condition at potential initiation sites on a pipe surface. For example, a pipeline operating at 72% SMYS may actually have areas on its surface where the net hoop stress is 100% SMYS or more. This level of stress is quite possibly sufficient for crack initiation to occur. (Zheng et al. 2000)

The effect of stress raisers such as surface gouges, weld toes and corrosion pits is to multiply the local stress in their vicinity. When these types of stress raisers are on the surface of a high pressure pipeline, they can multiply the local stress conditions by a factor of two or even more.(Eadie et al. 2002, Zheng et al. 2000, Eadie et al. 2005) For example, elastic-plastic finite element work by Eadie et al. shows that the stresses at the base of a frustum shaped pit on X-65 line pipe operating at 68% SMYS can be 129% SMYS, without any residual tensile stresses in the material. (Eadie et al. 2005)

The combination of residual stresses and local stress raisers has certainly been shown to elevate the stress conditions in localized regions of pipe surface to exceed the yield stress. However, localized plasticity is not a sufficient condition for crack initiation. The involvement of hydrogen in the crack initiation process is also understood to be a crucial component of the near-neutral pH SCC process.

2.3.4. The Role of Hydrogen in Crack Initiation

For NNpHSCC, both dissolution and hydrogen are evidenced to play a role in the cracking process. Dissolution products exist on the lateral faces of NNpHSCC cracks, and it is reasonable to expect that such dissolution will also occur to some extent at the crack tip. (Bouaeshi et al. 2005) However, anodic current measurements indicate that crack growth rates cannot be accounted for solely by dissolution. (Parkins and Beavers 2003) Evidence for the involvement of hydrogen includes quasi-cleavage crack surfaces (before this detail is obscured by ongoing corrosion) and the dependence of cracking propensity on changes in applied potential. (Parkins and Beavers 2003)

Parkins et al. (Parkins 1998, Parkins 1998B, Parkins 1999) have proposed that NNpHSCC cracks initiate from corrosion pits where a localized environment exists with a low enough pH to cause hydrogen to enter the metal at the existing pit potential. Carbon dioxide plays a role in lowering the pH of the solution and enabling the creation of hydrogen ions. The hydrogen in the steel locally degrades the mechanical properties and cracks initiate as a combination of anodic dissolution and hydrogen effects. (Yu 1997) A number of theories exist to describe the mechanisms by which hydrogen in solution degrades the mechanical properties of metals and alloys. These are briefly introduced and described later in this section.

Sources of hydrogen in the near-neutral pH environments include cathodic protection, hydrogen pre-charging, and the presence of CO_2 in groundwater which lowers the solution pH (raises the hydrogen concentration). As illustrated below in Figure 6, the corrosion of metal can act as a source of hydrogen which can be absorbed into the metal at a stress concentration such as a corrosion pit. Anodic dissolution of the metal produces positively charged metal anions, M^{n+}, which react with water to form metal hydroxides and hydrogen ions. Some of this hydrogen adsorbs on the metal surface where it recombines to form H_2, while the balance absorbs into the metal as atomic hydrogen.

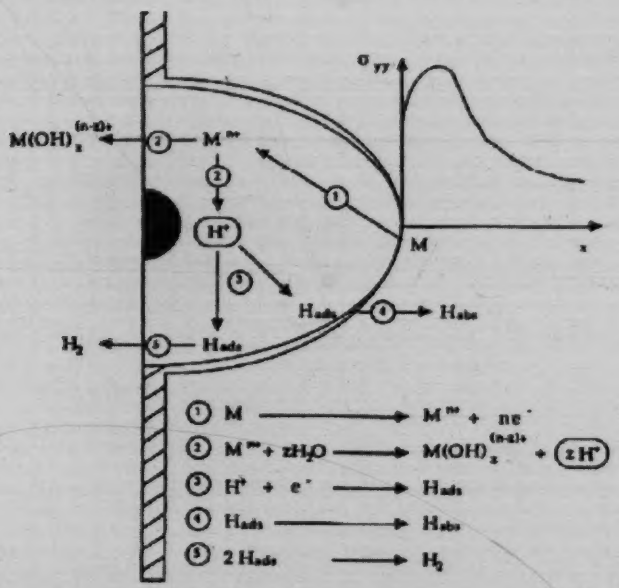

Figure 6 - Schematic of stress corrosion crack initiation from hydrogen ingress at a surface defect [Source: Delafosse and Magnin, 2001]

As described in Section 2.4.2, stressed metal has an increased capacity for interstitial hydrogen. The peak in hydrostatic stress that exists slightly in from the tip of the surface defect acts as a sink for hydrogen that is adsorbed on the metal surface. By SEM fractographic examination of the microdamaged zone in failures caused by NNpHSCC and comparison of the size of these zones to finite element estimates of plastic zone size, Toribio offers evidence that the hydrogen-induced microdamage of hot rolled pearlitic steel is caused by stress-driven diffusion of hydrogen. (Toribio 1996)

Hydrogen embrittlement has received intense study over several decades, (Troiano 1960; Oriani 1970; Johnson and Lin 1981; Hirth 1980; Tyson 1979) but is still not well understood. The effects of hydrogen can be observed in changes to many of the mechanical parameters that are used to characterize materials, including elongation to failure, reduction in area, ultimate fracture strength, strain hardening rate, fracture toughness, and time to failure. The type and extent of these changes varies between different materials and environments, which has

made it more difficult for scientists to understand the mechanisms by which hydrogen is acting. It is currently believed that there are a number of mechanisms by which hydrogen in solution degrades the mechanical properties of metals and alloys.

Systems that experience hydrogen embrittlement can be divided into two categories: those that form hydrides and those that do not. Hydrides form in a category of materials known as exothermic hydrogen occluders when the hydrogen solubility limit in the material is exceeded and hydrogen precipitates as a brittle second phase within the material. (Anderson 1996) The materials of interest in the study of near-neutral pH stress corrosion cracking are non-hydride formers and mechanisms of HE related to hydride formation are not addressed here.

Many models to explain hydrogen embrittlement have been proposed. The most significant of these are the hydrogen phase change theory, the hydrogen pressure theory, the hydrogen enhanced decohesion theory (HEDE) and the hydrogen enhanced localized plasticity theory (HELP).(Krom et al. 1999) Just two of these proposed models seem to be viable in applying them to numerous cases of HE under different conditions. These are the HELP and the HEDE mechanisms. (Parkins and Beavers 2003)

To begin describing these two models, it is first important to address the commonly used term, "hydrogen embrittlement". On a macroscopic scale, it is commonly observed that hydrogen decreases the fracture resistance of metals and alloys, and that the resulting fracture surfaces exhibit brittle quasi-cleavage characteristics. (Parkins 1994) However, describing the process as embrittlement suggests that a ductile-to-brittle transition occurs in the metal as a result of the dissolved hydrogen.(Katz et al. 2001) It should be kept in mind that the term "hydrogen embrittlement" describes some of the macroscopic manifestations of

the effect of hydrogen on metals and alloys, but does not imply that the failure mechanism is a loss of ductility on a microscopic scale.

The hydrogen enhanced decohesion model was introduced by Troiano and by Steigerwald et al. in 1960. (Troiano 1960; Steigerwald 1960) The main premise of this model is that hydrogen acts to decrease the cohesive forces at either the grain boundaries or the cleavage planes. Cracking occurs when the applied tensile stress exceeds this lowered cohesive force. Cracks can propagate by the combined effects of stress concentration and hydrogen enrichment at the crack tip. The fracture surfaces predicted by HEDE should be either intergranular, or follow susceptible crystallographic orientations in each grain.

The hydrogen enhanced localized plasticity model proposes that hydrogen causes highly localized shear failure of the material by increasing the mobility of dislocations in the hydrogen enriched area. Thus, this model is sometimes referred to as the localized-slip model. Beachem was the first proponent of the HELP model for HE (Beachem 1972); other supporters include Lynch, Birnbaum and Robertson (Lynch 1979; Lynch 1986; Birnbaum and Sofronis 1994; Robertson 2001). The HELP model is based on hydrogen-deformation interactions that occur on a microscopic scale and are therefore very difficult to observe through macroscopic tests. The most convincing experimental data for this mechanism are in-situ TEM observations by Birnbaum of dislocation movement at a crack tip. Upon the introduction of gaseous hydrogen to the test cell, dislocation movement increased very significantly and it then slowed when the hydrogen fugacity was decreased or removed. (Tabata and Birnbaum 1983, Tabata and Birnbaum 1984) More strong evidence for the HELP mechanism can be found in the theoretical calculations of elastic shielding of stress centers when hydrogen is dissolved in a metal or alloy. (Birnbaum and Sofronis 1994) The fracture surfaces predicted by HELP should have tear ridges and very small dimples, similar to but smaller than those seen in micro-void coalescence. These dimples have been observed in work by Lynch and others. (Lynch 1986)

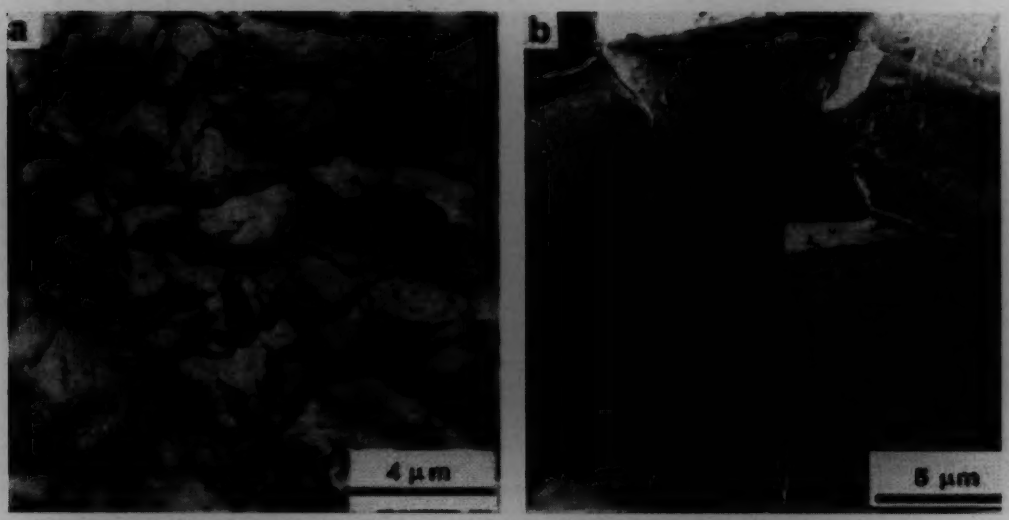

Figure 7 – Replicas showing (a) dimples formed at high K (stress intensity factor) and (b) intergranular tear ridges formed at low K on fracture surface of 0.28% C steel specimen. [Source: Beachem 1972]

The effect of hydrogen on the yield stress and flow stress of metals and alloys is not widely agreed upon. There are researchers who have observed lower yield stresses in the presence of hydrogen (Lian and Meletis 1996; Beachem 1972; Liang et al. 2004; Birnbaum 1994), researchers who report the opposite (Abraham and Altstetter 1995, Kimura and Matsui 1987), and some who have observed no change in yield strength. (Parkins 1998A; Tyson 1979)

There is a higher degree of consensus that hydrogen increases dislocation mobility and dislocation multiplication rates, so it can cause a crack to propagate through the plastic region at a crack tip. (Sofronis and McMeeking 1989)

The flow stress of mild steels is markedly reduced by hydrogen ingress, as was shown in experiments by Beachem.(1972) Hydrogen-related softening has been observed in f.c.c., b.c.c, and h.c.p, systems, in pure metals, solid solutions and in precipitation hardened systems. It appears to be a very general effect which suggests that the mechanism of softening should be able to be described in terms of elastic interactions between dislocation or between dislocations and other stress centres, such as solute atoms and precipitates. (Birnbaum and Sofronis 1994)

Tensile tests performed by Tyson and shearing punch tests carried out by Parkins indicated that hydrogen in solid solution has little effect on the yield stress of steel. (Tyson 1979; Parkins 1998A) The punch tests in Parkins' work showed no dependence of plasticity onset on hydrogen exposure. Hydrogen did not reduce the yield strength for X-52 and X-60 tested in NS4 solution.

The HEDE and HELP mechanisms appear upon first consideration to be very different. Respectively, they predict decohesion and cleavage fracture versus slip and dimpled fracture surfaces. However, the two models both describe the effect of hydrogen on metals and alloys as decreasing the bonding strength within the material: HEDE predicting material separation normal to the largest principal tensile stress and HELP predicting material separation along the direction of greatest shear stress. In both cases, the applied stress needed for crack growth to occur is lowered by the effect of hydrogen in the metal. (Been et al. 2004)

Lian and Meletis have observed that hydrogen enhanced localized plasticity creates large strains in a small near-surface volume, and that the material in this region begins to crack at the same fracture strain as observed in bulk specimens without hydrogen effects. (Lian and Meletis 1996)

This failure criterion may be combined with the quantitative, continuum mechanics-based, description of the hydrogen induced material softening effect that predicts decreasing local flow stress with increasing hydrogen concentration. (Sofronis et al. 2001; Liang et al. 2003; Liang et al. 2004) This relation may be expressed as:

$$\sigma_Y(\varepsilon^p, c) = \sigma_o(c)\left(1 + \frac{\varepsilon^p}{\varepsilon_o}\right)^N \qquad (14)$$

where

σ_Y is the local flow stress

C is the total hydrogen concentration, [H atoms / solvent atom]

$\sigma_o(C)$ is the yield stress in the presence of hydrogen

$\sigma_o(0)$ is the yield stress in the absence of hydrogen

ε_o is the corresponding yield strain in the absence of hydrogen

ε^P is the logarithmic strain in uniaxial tension.

N is the work hardening exponent

In systems that do not form hydrides, the hydrogen concentration, c, will be between zero and one. The work hardening exponent, N, is assumed to remain unaltered in the presence of hydrogen. This assumption is made by the proponents of this model in the absence of any conclusive experimental evidence. The suggested form of $\sigma_o(c)$, the variation in yield stress with hydrogen concentration, is a linear function:

$$\sigma_o(c) = [(\xi - 1)c + 1]\sigma_o(0) \tag{15}$$

where

ξ is a softening parameter (≤ 1)

If ξ were equal to 1, this would indicate no dependence of flow stress on hydrogen concentration. If ξ were equal to 0, this would mean that the yield stress of the material linearly decreases to zero as the hydrogen concentration increased to its maximum value of one hydrogen atom per solvent atom.

It is important to note that, in describing this model, the authors emphasize that they are attempting "to quantify the experimental understanding of the hydrogen effect on dislocation mobility in a continuum sense" and not to reflect a precise constitutive material response. (Liang et al. 2003)

The cracking process driven by HELP is understood to be a slow, sub-critical process controlled by environmental factors. This process is described by stage II in the crack-growth kinetics curve. (Toribio 1996) For a constant load, crack growth progresses by highly localized ductile tearing. The propagation of the crack through the material is controlled by the rate of hydrogen diffusion to the area of peak hydrostatic stress ahead of the crack tip.

2.4. Description of Equilibrium Hydrogen Concentration Model

Hydrogen concentration in metals can be modeled after the work of Sofronis and McMeeking, which is based on the equilibrium theory given by Oriani and Johnson and Lin. (Sofronis and McMeeking 1989; Oriani 1970; Johnson and Lin 1981)

The present work only considers equilibrium hydrogen concentrations, and does not address the diffusion processes required to attain these equilibrium configurations. This simplification requires that the material experiences steady or near-steady conditions for long enough that the diffusion process can be completed. Hydrogen is more mobile at higher temperatures so that the diffusion process will occur more quickly at higher temperatures, and equilibrium will be attained sooner. (Sofronis and McMeeking 1989)

Diffusion can be roughly estimated using:

$$x = \sqrt{Dt} \tag{16}$$

where

x is the distance over which the solute (hydrogen) diffuses,
D is the diffusion coefficient for the solute (hydrogen) in the material, and
t is the time over which the diffusion occurs.

So, for example, if an increase in system temperature were to increase the diffusion constant by a factor of two, equilibrium hydrogen concentrations within

a given distance would be established in half of the original time required. Typical diffusion coefficients for hydrogen in X-52 steel are in the range of 1×10^{-7} cm^2/s and 3×10^{-7} cm^2/s.

Hydrogen can be present in metal either in lattice sites or in trap sites. It is commonly assumed that all traps in iron and steel are saturable (Kumnick and Johnson 1980) and reversible (Oriani 1970). These traps are also assumed to be isolated, so that hydrogen transport between trap sites can only occur by lattice diffusion. (Krom et al. 1999) When hydrogen is present in large enough amounts within a metal or alloy, it can form second-phase hydrides or hydrogen gas blisters. Neither of these phenomena is typically observed in NNpHSCC.

When pipeline steel is in a near-neutral solution, hydrogen will reside in the alloy, both in lattice positions and traps, even when the material is not under stress. In the equations related to hydrogen concentrations, parameters referring to lattice hydrogen use the subscript L, and those referring to trapped hydrogen use the subscript T.

2.4.1. Unstressed Lattice Hydrogen Concentration

The three key parameters that determine the unstressed lattice hydrogen concentration, C_L^o, for a given solution composition are temperature, solution pH and potential. Hydrogen solubility in a metal decreases at higher temperatures.

Solutions with a lower pH create a higher C_L^o because there are more hydrogen ions in solution. From steady-state subsurface hydrogen concentrations determined from Devanathan-Stachurski hydrogen permeation experiments of three grades of pipeline steels at three pH levels, Parkins and Beavers show that a decrease in groundwater pH from 8.3 to 6.1 by absorption of CO_2 produces a roughly five-fold increase in the propensity for hydrogen ingress. This trend is not observed to be dependent upon the type of pipeline steel tested; all three grades of steel showed this result. (Parkins and Beavers 2003)

The effect of solution potential is not as clear. Parkins has shown in tests at pH 5.1 and 6.3 that higher values of C_L^o are observed at intermediate electrochemical potentials, with the peak existing at about -900 mV SCE. As the potential becomes more negative than this, a visible carbonate film forms on the surface, which is a barrier to hydrogen ingress. These results are illustrated in Figure 8, with measurements at open circuit potentials indicated with horizontal lines showing the range of potentials measured. (Parkins 1998A)

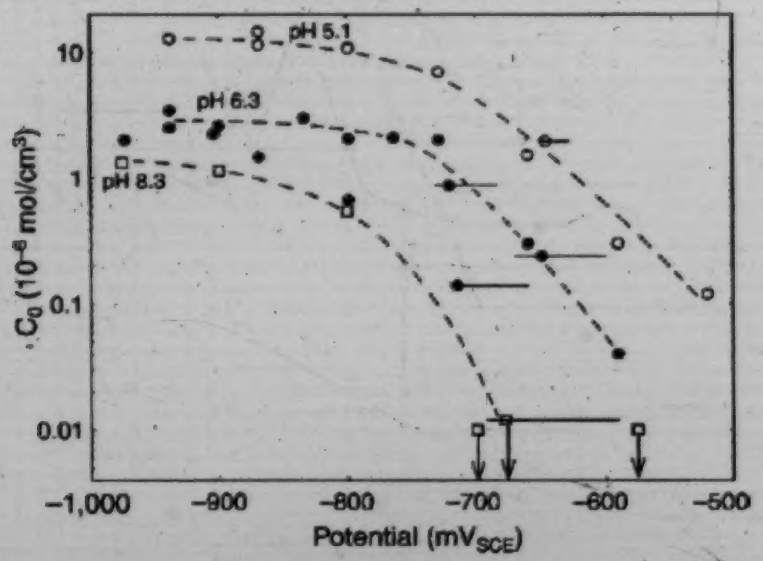

Figure 8 - Hydrogen concentrations for X-52 in NS4 as a function of potential and pH [Source: Parkins and Beavers 2003]

Corrosion products on the surface of a pipe reduce the observed hydrogen diffusivity, D, in the alloy. When hydrogen does penetrate the surface barrier of corrosion products, the subsurface lattice hydrogen concentration, C_L^o, that results is not markedly different than the equivalent concentration found for the polished surfaces tested in work by Parkins. Thus, it has been shown that for pipeline steels in near-neutral pH groundwater solution, C_L^o is a function of the solution, but not a function of the surface condition. (Parkins 1998A)

The experimental measurements of C_L^o by several workers are compared. The relevant measurements of C_L^o are plotted in Figure 9, and the details of these tests are summarized in Table 7.

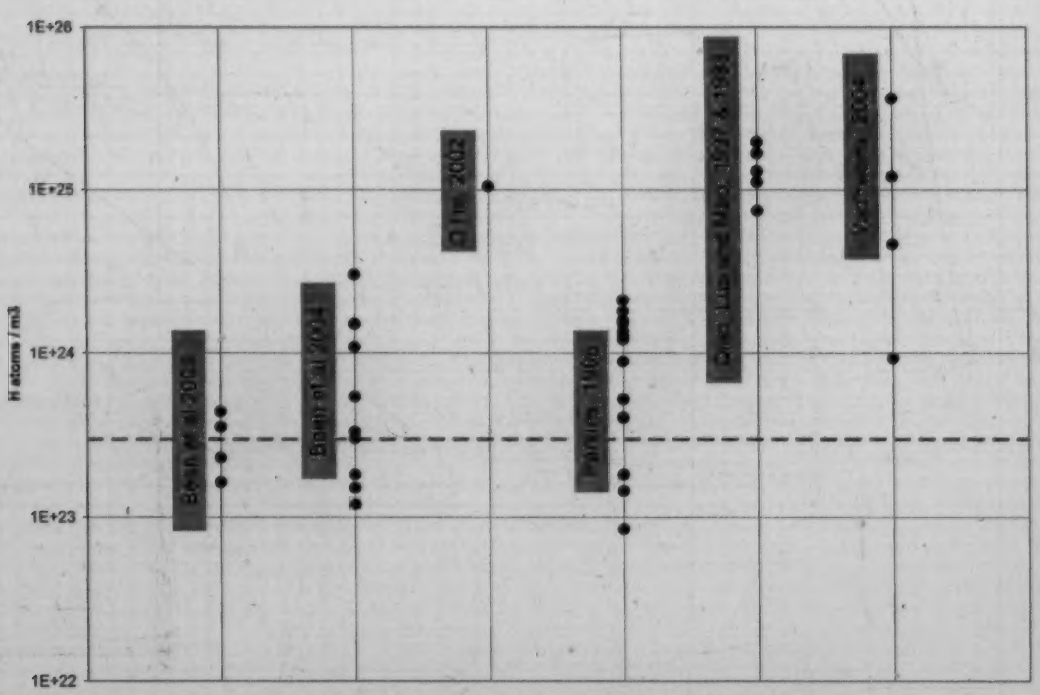

Figure 9 – Unstressed lattice hydrogen concentrations in pipeline steels

Table 7 – Summary of tests giving unstressed lattice hydrogen concentrations

	C_L^o (H atoms / m^3)	Test Conditions
Been et al., 2003: Permeation tests on X-65	4.40×10^{23}	polished specimen in H_2O
	3.55×10^{23}	polished specimen in D_2O
	2.29×10^{23}	millscaled specimen in H_2O
	1.63×10^{23}	millscaled specimen in D_2O
Been et al., 2004: Permeation tests on X-65 in H_2O	1.20×10^{23}	log $[HCO_3^-]$ varied from -3.5 to -2, pH = 8.5
	10.84×10^{23}	log $[HCO_3^-]$ varied from -3.5 to -2, pH = 5.5
	1.81×10^{23}	$[HCO_3^-]$ 610 ppm, 10% CO_2/N_2 gas, $[SO_4^{2-}]$ 300 ppm
	3.31×10^{23}	$[HCO_3^-]$ 610 ppm, 10% CO_2/N_2 gas, $[SO_4^{2-}]$ 0 ppm
	3.01×10^{23}	$[HCO_3^-]$ 610 ppm, 10% CO_2/N_2 gas, $[HS^-]$ 0 ppm
	30.10×10^{23}	$[HCO_3^-]$ 610 ppm, 10% CO_2/N_2 gas, $[HS^-]$ 100 ppm
	1.51×10^{23}	$[HCO_3^-]$ 0 ppm, 10 ppm Cl-, N_2 gas
	15.10×10^{23}	$[HCO_3^-]$ 0 ppm, 10 ppm Cl-, 10% CO_2/N_2 gas

	1.20×10^{23}	$[HCO_3^-]$ 610 ppm, 10% CO_2/N_2 gas, AQDS† 20 ppm
	5.42×10^{23}	$[HCO_3^-]$ 610 ppm, 10% CO_2/N_2 gas, O_2 100 ppm
He, 2002: X-65 in NS4, measurement in LECO RH-402 Hydrogen Analyser	1.04×10^{25}	Charging at -900 mV SCE or 0.2 mA / cm^2
Parkins 1998: Permeation tests on X-52 in NS4	20.90×10^{23}	-938 mV, pH = 6.3
	15.23×10^{23}	-938 mV, pH = 6.3
	13.61×10^{23}	-904 mV, pH = 6.3
	15.84×10^{23}	-900 mV, pH = 6.3
	8.85×10^{23}	-869 mV, pH = 6.3
	18.00×10^{23}	-834 mV, pH = 6.3
	12.35×10^{23}	-799 mV, pH = 6.3
	4.04×10^{23}	-799 mV, pH = 6.3
	12.65×10^{23}	-764 mV, pH = 6.3
	12.11×10^{23}	-729 mV, pH = 6.3
	5.24×10^{23}	-721 mV, pH = 6.3
	0.84×10^{23}	-715 mV, pH = 6.3
	1.81×10^{23}	-660 mV, pH = 6.3
	1.45×10^{23}	-649 mV, pH = 6.3
Qiao, Luo and Mao 1997: X-52 in acidified NS4, precharged in poisoned H_2SO_4, measurement by secondary-ion mass spectroscopy (SIMS)	1.11×10^{25}	OCP, pH = 8
	1.11×10^{25}	-800 mV, pH = 8
	1.95×10^{25}	-1000 mV, pH = 8
	1.30×10^{25}	OCP, pH = 5
	1.67×10^{25}	OCP, pH = 3
Qiao, Luo and Mao 1998: X-80, measurement by SIMS	0.74×10^{25}	unstressed in air
Vadhwana 2004: X-65, diffusible hydrogen measurement by mercury displacement, trapped hydrogen measurement in LECO RH-402 Hydrogen Analyser	1.20×10^{25}	Charged in poisoned H_2SO_4 with currents 0.35 – 1 mA / cm^2
	3.61×10^{25}	Charged in poisoned H_2SO_4 with currents 0.35 – 1 mA / cm^2
	9.29×10^{23}	Trapped hydrogen in as-received sample
	0.46×10^{25}	Diffusible hydrogen after charging in poisoned H_2SO_4 at 0.05 mA/cm^2

† 9,10-anthraquinone-2,6-disulfonate

2.4.2. Lattice Hydrogen as a Function of Stress

The diffusion of hydrogen into the region surrounding a defect is largely controlled by hydrostatic stress gradients. The bcc structure of α-iron provides both tetrahedral and octahedral interstitial sites. The observations of Hirth (1980) as well as Kiuchi and McLellan (1983) indicate that lattice hydrogen in α-iron occupies tetrahedral sites, but this is not known for certain. Both types of sites are too small to contain a hydrogen atom without distortion of the surrounding lattice. When hydrogen is dissolved in α-iron, it causes a positive change in volume. The

chemical potential of hydrogen in α-iron is lower when the iron is under a tensile hydrostatic stress, because the hydrogen atoms fit more easily into the stretched lattice. This chemical potential, μ_L, is expressed as (Krom et al. 1999):

$$\mu_L = \mu_L^0 + RT \ln \frac{C_L}{N_L} - \overline{V}_H \sigma_h \tag{17}$$

where

μ_L° is the chemical potential at a reference temperature and pressure,

R is the universal gas constant, 8.314 J/mol·K

T is the absolute temperature of the system,

C_L is the concentration of hydrogen in lattice sites [H atoms/m^3],

N_L is the number of lattice sites per unit volume,

V_H is the partial molar volume of hydrogen,

σ_h is the hydrostatic stress, $\sum_i \frac{\sigma_{ii}}{3}$,

σ_{ii} is the principal stress and

i denotes the three reference directions.

Assuming that hydrogen expands the metal lattice isotropically, the partial molar volume of hydrogen, V_H, is 2.0 x 10^{-6} m^3/mol. The number of lattice sites per unit volume, N_L, is inversely related to the molar volume of the lattice (Sofronis and Mc Meeking 1989):

$$N_L = \frac{N_A}{V_M} \tag{18}$$

where

N_A is Avogadro's number (6.023x10^{23} atoms/mole), and

V_M is the molar volume of the host lattice [m^3/mole]

For the bcc lattice of steel, V_M is 7.116 x 10^{-6} m^3/mole. This determines that N_L, the number of lattice sites is 8.4643 x 10^{28} / m^3.

When a positive hydrostatic stress exists, hydrogen diffuses to this region in order to lower the chemical potential. Conversely, hydrogen will move out of areas that experience compressive hydrostatic stress. The equilibrium concentration of hydrogen in a stressed lattice, C_L^{σ}, is (Sofronis and Mc Meeking 1989):

$$\frac{C_L^{\sigma}}{C_L^{0}} = \exp\left(\frac{\sigma_h \overline{V}_H}{RT}\right) \tag{19}$$

where

C_L^{0} is the lattice concentration of hydrogen in the absence of stress,

C_L^{σ} is the steady state lattice concentration of hydrogen under hydrostatic stress,

and the other terms are as defined earlier

The equilibrium hydrogen concentration in an unstressed material, C_L^{o}, is a function of temperature, solution pH and electrochemical potential.

2.4.3. Hydrogen Trapping

Hydrogen can also occupy trap sites in the material. Trap sites in steel include dislocations, grain boundaries and interfaces between the matrix and second-phase particles. Each of these types of trap sites provides a larger space for a hydrogen atom to reside than available in an interstitial lattice site. Solute hydrogen will preferentially reside in trap sites. The occupancy of lattice and trap sites, θ_L and θ_T respectively, can be determined with the hydrogen concentrations and the number of available trap and lattice sites (Sofronis and McMeeking 1989):

$$C_L = \theta_L \beta N_L \tag{20}$$

$$C_T = \theta_T \alpha N_T \tag{21}$$

where

C_T is the concentration of hydrogen atoms in traps,

θ_L is the fractional occupancy of lattice sites, [occupied lattice sites / available lattice sites]

θ_T is the fractional occupancy of trap sites, [occupied trap sites / available trap sites]

β is the number of available lattice sites per solvent atom, which is fixed for a given lattice, and is taken as 6 for tetrahedral occupancy in a bcc lattice,

α is the number of hydrogen atoms occupying a trap site (equal to 1), and

N_T is the number of traps per unit lattice volume

2.4.3.1. Trap Densities in Pure Iron

Using hydrogen permeation tests on pure iron with hydrogen gas charging, Kumnick and Johnson collected trap density data for various degrees of plastic work and temperature. (Kumnick and Johnson 1980) This work found that the trap density in iron increases sharply with plastic deformation at low strain level, and then reaches a saturation point at a plastic strain of roughly 0.8. The number of traps, N_T, in the lattice has been empirically fit to a logarithmic function of plastic strain, ε_p, by Sofronis and McMeeking. (Sofronis and Mc Meeking 1989) This relation has been used to in models of materials ranging from pure iron to high strength steel.

$$\log N_T = 23.26 - 2.33\exp\left(-5.5\varepsilon_p\right) \tag{22}$$

where

ε_p is the plastic strain

Figure 10 shows the data of Kumnick and Johnson, and the logarithmic fit proposed by Sofronis and McMeeking. (Kumnick and Johnson 1980; Sofronis and McMeeking 1989)

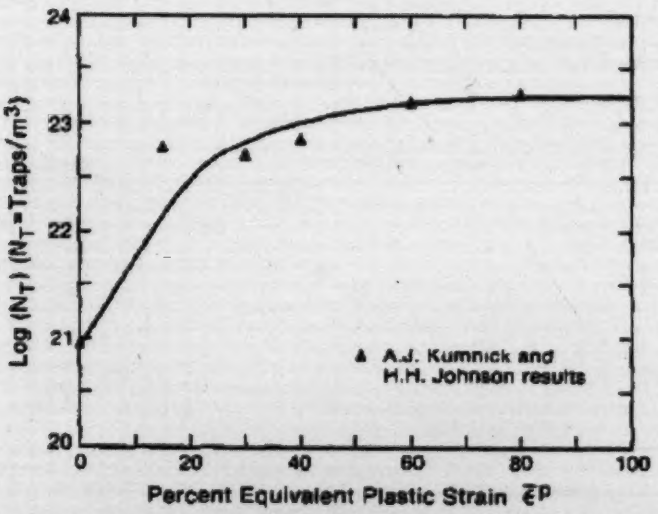

Figure 10 - Trap Density and Equivalent Plastic Strain for Pure Iron [Source: Sofronis and McMeeking 1989]

The work of Kumnick and Johnson also allowed for the determination of the trap binding energy, ΔH_B, as -60 kJ/mol, independent of deformation within the range of 0 – 80% cold work and independent of temperature within the range of 288 – 343 K. This independence of trap binding energy on temperature and cold work parameters indicates the presence of only one type of trap in iron. (Kumnick and Johnson 1980)

2.4.3.2. Trap Densities in Pipeline Steels

Trap density measurements using pipeline steels have been attempted by researchers studying near-neutral pH SCC. Parkins (1998A, 1998B) followed the same approach used by Kumnick and Johnson (1980) in which successive hydrogen permeation tests are conducted on the same sample. If there are unfilled traps in an alloy, an increase in the measured hydrogen diffusivity will be observed between the first and second permeation test. It will take longer for the hydrogen flux through the sample to reach a steady state condition in the first test because additional hydrogen would be needed to fill empty hydrogen traps.

Through hydrogen permeation tests on pipeline steels that had previously been in service, Parkins found that the existing traps in these steels had already been

filled. (Parkins 1998A; Parkins 1998B) Further tests in which the steel samples were annealed to remove trapped hydrogen prior to the first permeation tests still failed to demonstrate the expected increase in measured hydrogen diffusivity during the second permeation test. Even with further adjustments to the experimental procedure, permeation behaviour characteristic of trap filling was not obtained.

In an effort to calculate hydrogen trap density in the steels being studied using the available experimental data, Parkins then used the diffusion rates and the sub-surface lattice hydrogen concentrations measured from permeation tests to calculate the number of traps by a less direct method. Oriani (1970) defines the trap density in a material as:

$$N_T = C_L^o \cdot 2 \times 10^{23} \left[\left(\frac{D_L}{D_B} \right) - 1 \right] \qquad (23)$$

where

D_L is 3.08 x10^{-5} cm^2/s for the conditions in Parkins' tests, and

D_B is the effective diffusion coefficient.

The trap densities calculated using this method indicate that trap density varies with the pH of the test NS4 solution and with the type of alloy. Table 8 lists these results.

The dominant trap type in steels is understood to be the carbide interfaces between ferrite and cementite regions. The three steels tested were found to have significantly different trap concentrations, with the X-52 steel having the most hydrogen traps. This variation between the steels can be correlated with pearlite content. A table by Hirth (1980) summarizing characteristics of different trap types lists a trap binding energy of -84 kJ/mol for carbide interfaces, in comparison to -60 kJ/mol for traps at grain boundaries and dislocation cores.

Table 8 – Mean Number of Hydrogen Traps (10^{25} / m^3) with Standard Deviation in Brackets for Three Pipeline Steels Exposed to NS4 Solution at Different pH [Source: Parkins and Beavers 2003]

Steel	pH 5.1 Solution	pH 6.3 Solution	pH 8.3 Solution
X-52	10.3 (7.4)	3.3 (2.3)	2.3 (0.6)
X-60	6.3 (5.9)	0.7 (0.3)	0.5 (0.06)
X-65	8.1 (6.1)	3.3 (2.0)	1.3 (0.9)

The calculated trap densities vary by up to an order of magnitude between tests in solutions with different pH values. A physical explanation for this effect has not been offered. Parkins and Beavers (2003) state that "it [is not] unexpected that that the values of $N_{[T]}$ depend on the solution pH" because the calculation depends on C_L^o, which varies markedly with solution pH and potential.

2.4.3.3. Equilibrium Between Lattice and Trap Occupancy

As proposed by Oriani, local equilibrium must exist between the hydrogen in interstitial lattice sites and that occupying reversible traps in the material. Assuming that both lattice and trap sites are finite populations and that no interactions occur between occupied sites, this equilibrium can be expressed as (Oriani 1970):

$$K_\theta = \frac{1-\theta_L}{\theta_L}\frac{\theta_T}{1-\theta_T} \tag{24}$$

The equilibrium term, K_θ, is a function only of temperature for α-iron, in which the trap binding energy, ΔH_B, is treated as a constant over the deformation and temperature ranges of interest.

$$K_\theta = \exp\left(\frac{-\Delta H_B}{RT}\right) \tag{25}$$

The process of using the equations described above to find both the lattice and trapped hydrogen concentration is illustrated in Figure 11.

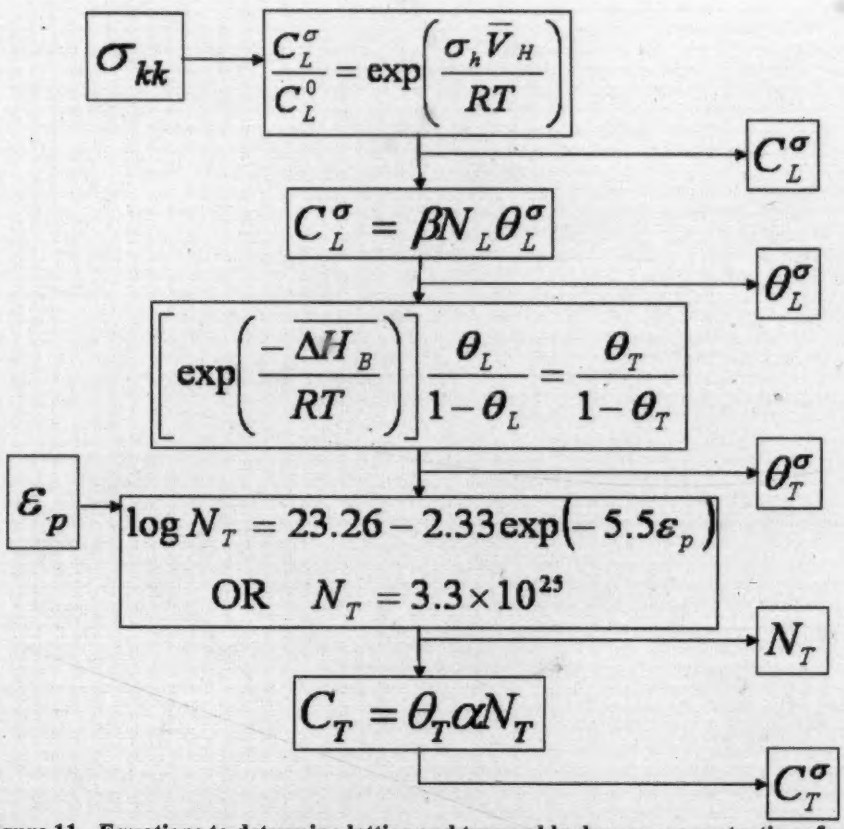

Figure 11 - Equations to determine lattice and trapped hydrogen concentrations from hydrostatic stresses and plastic strains

2.5. Motivation for research

The mechanism by which near-neutral pH stress corrosion cracks initiate from corrosion pits is not well understood and is crucial to the overall understanding of NNpHSCC. The majority of cracks initiate at corrosion pits. These pits are stress raisers and thus higher hydrogen contents exist around them. It is widely accepted that both anodic dissolution and hydrogen effects cause NNpHSCC. If the initiation of NNpHSCC can be explained by the elevated concentration of hydrogen in pipeline steel surrounding a corrosion pit, this will add valuable knowledge to the current understanding of this cracking phenomenon.

The aim of this thesis is to quantitatively investigate the role of hydrogen in the transition of pits to cracks in near-neutral pH conditions. Finite element modelling of stresses and hydrogen concentrations around corrosion pits was carried out. Experiments were carried out to find the difference in hydrogen content between X-52 samples in air and in near-neutral pH solution. The effect of near-neutral pH solution and hydrogen content on the room temperature creep behaviour of X-52 steel was also investigated experimentally.

3. MODELLING AND EXPERIMENTAL METHODS

3.1. Description of Finite Element Model

A three-dimensional finite element model of a surface corrosion pit was created using ANSYS 10.0 software. A two dimensional model of a surface notch was also created with the same software.

3.1.1. Three Dimensional Geometries

The pit modeled in the majority of the finite element work was hemispherical, and was small enough that the pipe material surrounding the pit could be considered to be a semi-infinite body. In other words, the wall thickness is many times larger than the pit radius, so that the stress intensification around the pit does not depend on the pit size. Figure 12 shows results from sensitivity analyses that were conducted to confirm the validity of treating the pit as if it exists in a semi-infinite body. As long as the pit depth is less than roughly 10% of the wall thickness, the stresses surrounding the pit are independent of pit size. For pipes with wall thicknesses of 6.4 to 12.7 mm. (API Specification 5L, 2004), this is a reasonable criterion, as corrosion pits that have been observed in association with NNpHSCC initiation are typically less than 0.5 mm in depth.

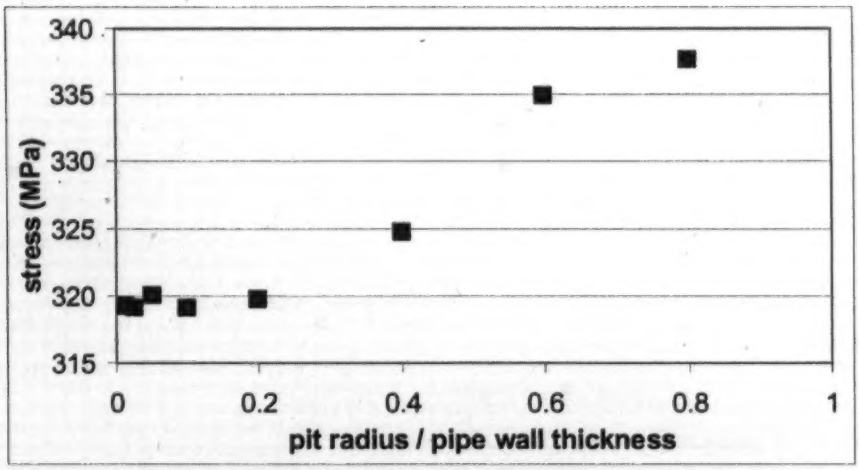

Figure 12 - Maximum hydrostatic stress near pit as a function of pit size

Two planes of symmetry were used to simplify the finite element model and reduce its computational demands. The resulting model is one-quarter of the full model.

The geometry of the model was also modified in order to study the effects of pit elongation or of strain enhanced dissolution that could sharpen the base of hemispherical corrosion pits. Cracks in the millscale on the surface of line pipe tend to be oriented longitudinally, which promotes the development of corrosion pits that are elongated in the direction perpendicular to the principal stress. (Eadie et al. 2005B)

Five geometries of three dimensional corrosion pits were modeled using the finite element program: a hemisphere, a hemisphere with a groove at its base caused by strain enhanced dissolution, a hemisphere with a cylindrical pit at its base, a hemiellipsoid, and a rounded frustum. Images of the pit model shown in this work are all in the same orientation. The quarter pit model with added dissolution at the pit base and its orientation in relation to the pipe surface are shown in Figure 13. The shape of the hemisphere with cylindrical dissolution, hemiellipsoid and rounded frustum models can be seen in Figure 29.

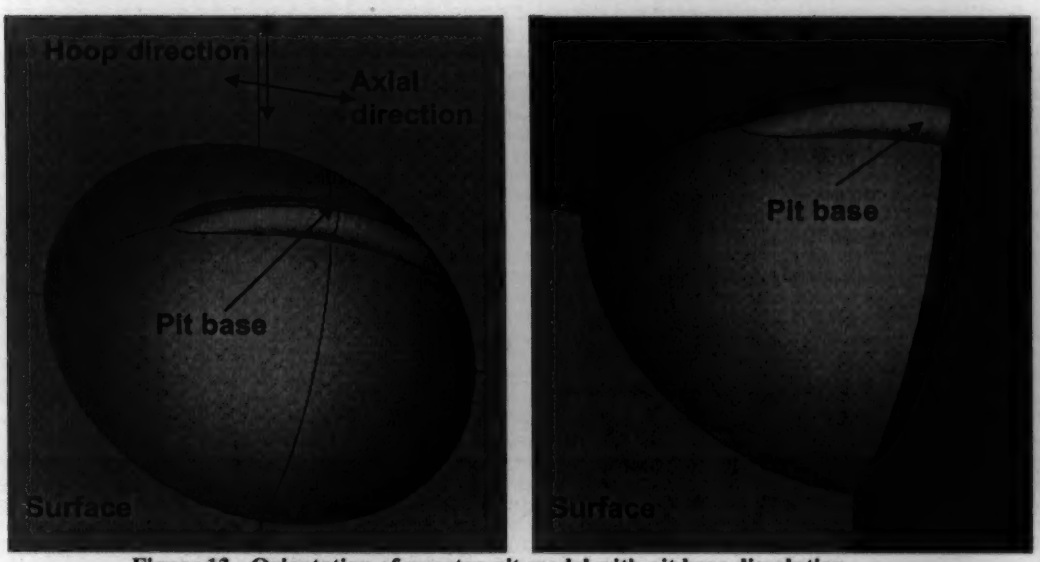

Figure 13 - Orientation of quarter-pit model with pit base dissolution

3.1.2. Two Dimensional Geometries

A series of two-dimensional models of surface notches were created to study the differences in stresses, strains and localized hydrogen concentrations for different depths and shapes of surface flaws. These models were created in two dimensions rather than three dimensions because of the added mesh density and computational demands for the relatively sharp tips of the more severe notches. Each notch was created in a bulk rectangular mesh measuring 50 mm long and 15 mm deep. The maximum notch dimensions modeled were 0.95 mm by 0.22 mm, and the bulk mesh was equivalent to a semi-infinite body with respect to the notch. Three types of model geometries were created. A straight walled notch with a tip radius of 50 μm was modeled with depths of 0.15, 0.25, 0.35, 0.55, 0.75 and 0.95 mm. A notch with walls angled out at 4° and a tip radius of 50 μm was also modeled with depths of 0.15, 0.25, 0.35, 0.55, 0.75 and 0.95 mm. A notch with a 0.15 mm notch mouth width and a depth of 0.3 mm to the notch tip center of curvature was modeled with tip radii of 20, 30, 50, 70 and 75 μm. Sample geometries are compared in Figure 14. In these figures, the notches are plotted right next to each other only for the purpose of easy display. In the modelling

work, each notch was modeled alone and no notch interaction effects were involved.

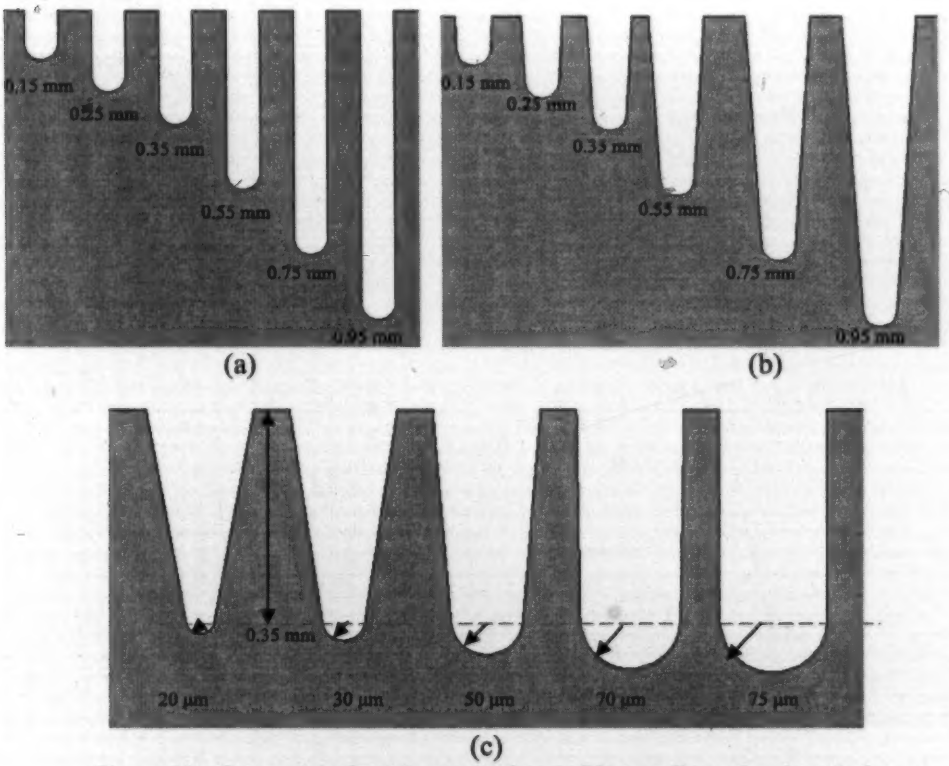

Figure 14 – Categories of notch geometries used in two dimensional analysis (a) straight wall (b) angled wall (c) varied tip radius

3.1.3. Mesh Convergence

The three dimensional pit geometries were meshed using 10-node tetrahedral elements. The two dimensional notch models were created with 6-node triangular elements. For each shape, a mesh convergence study was carried out to ensure that the mesh was sufficiently refined. The external stress values of interest were applied to the model and the mesh was iteratively refined until further refinement offered no change in the stress and strain results of the analysis. For example, the mesh refinement study for the hemispherical pit found that a mesh with 29,000 nodes gave satisfactory precision. Figure 15 shows the stress results for six levels of mesh refinement and Figure 16 shows the percentage change in the stress results from the previous to the current mesh. The change in all stress results

caused by refining the mesh from 29,916 nodes to 40,230 nodes is less than 1%. Further refinement to 55,343 nodes also gives changes in calculated stresses that are less than 1%. A mesh with 29,916 nodes offers sufficient precision for the purposes of this modelling and was used throughout. The same procedure was carried out to ensure mesh convergence for each of the other model geometries.

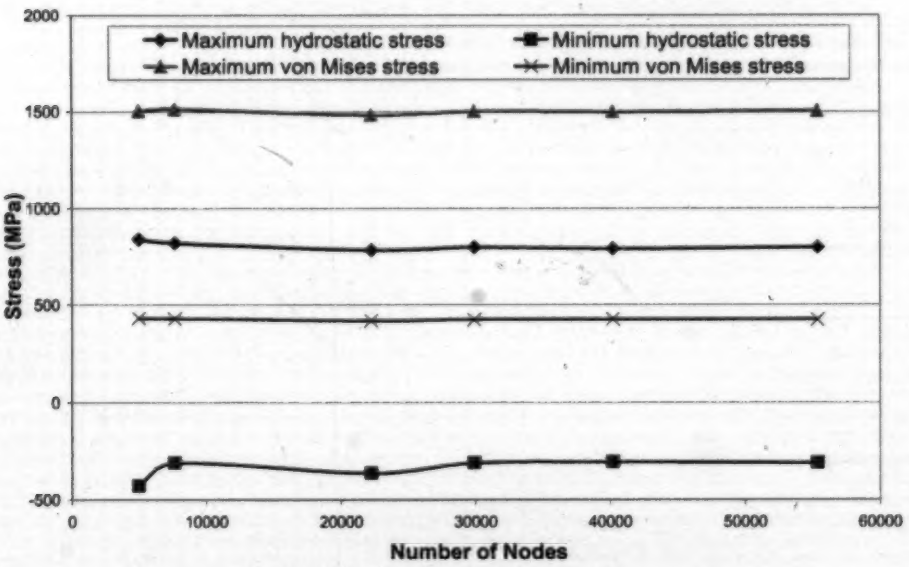

Figure 15 - Convergence of stress results with mesh refinement

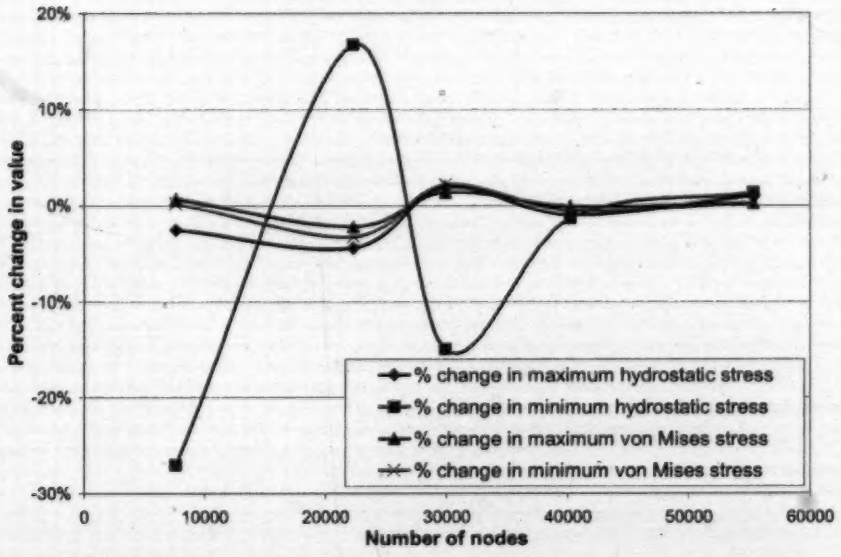

Figure 16 - Change in stress results from previous to current mesh refinement step

3.1.4. Material Properties

The finite element model was designed to model the stress-strain conditions and hydrogen contents of X-52 pipeline steel in a near-neutral pH solution. The chemical composition of this steel is given in Table 9.

Table 9 – Chemical composition (wt%) of X-52 pipeline steel

C	N	Mn	P	Si	Cu	Ni	Cr	Mo	Cb	Ti	Al
0.07	<0.0015	0.80	0.016	0.27	0.28	0.09	0.05	<0.01	0.012	0.019	0.031

Even in the absence of hydrogen effects, the stress-strain behaviour of X-52 can vary considerably between test specimens. The mechanical behaviour of X-52 outlined by API Specification 5L requires only that the yield strength is at least 359 MPa and the ultimate tensile strength is at least 455 MPa. Several stress-strain curves found in the literature for X-52 tensile behaviour in air are given in Figure 17.

There are clearly significant differences between stress-strain curves recorded during different investigations. The nature of the curves is also dependent upon strain rate. (Wang and Chen 2001) At a moderate strain rate of 1×10^{-3} / s, the uniform elongation for X-52 is 15.9%. (Wang et al. 2001) This value was used as the criterion for material cracking as described by Lian and Meletis (1996). When evaluating the results of finite element analyses, localized areas with total strain greater than roughly 16% were identified as areas where cracking will occur by highly localized ductile rupture.

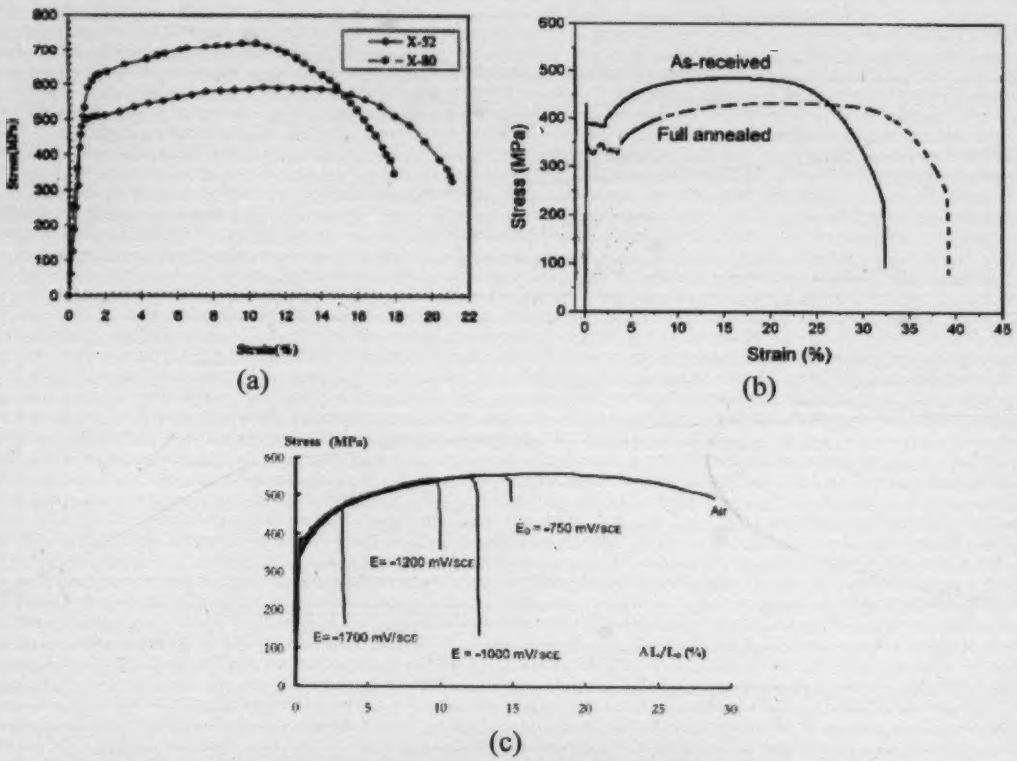

Figure 17 - Stress-strain curves for X-52 in air
(a) Stress strain curves for X-52 and X-80; X-52 has 500 MPa yield strength and 592 MPa ultimate tensile strength, elongation of 20.6% and reduction of area of 77.7% [Source: Yu 1997]
(b) Stress-strain curves of as-received and fully annealed X-52, exhibiting respective yield-point elongations of 2% and 3%. [Source: Wang and Chen 2001]
(c) Stress-strain curves of X-52 in air and at different imposed electrochemical potentials in NS-4 solution [Source: Delafosse and Magnin 2001]

Table 10 and Figure 18 show the true stress-strain material property data used in ANSYS 10.0 and the engineering stress-strain data from which it was calculated. This description of material constitutive behaviour was chosen to represent average properties of X-52.

Table 10 – Stress - strain data used for X-52 in finite element model

Engineering Stress (MPa)	Engineering Strain	True Stress (MPa)	True Strain	
0	0	0	0.000	
100	0.0005	100	0.000	
200	0.0010	200	0.001	
300	0.0014	300	0.001	
360	0.0017	361	0.002	**Yield strength**
400	0.010	404	0.010	
425	0.020	434	0.020	
445	0.025	456	0.025	
460	0.030	474	0.030	
480	0.040	499	0.039	
500	0.055	528	0.054	
520	0.070	556	0.068	
540	0.100	594	0.095	
550	0.140	627	0.131	
552	0.170	646	0.157	**Ultimate tensile strength**
548	0.200			**After necking onset, cannot calculate true stress and strain directly from engineering stress and strain data**
545	0.220			
530	0.250			
495	0.290			

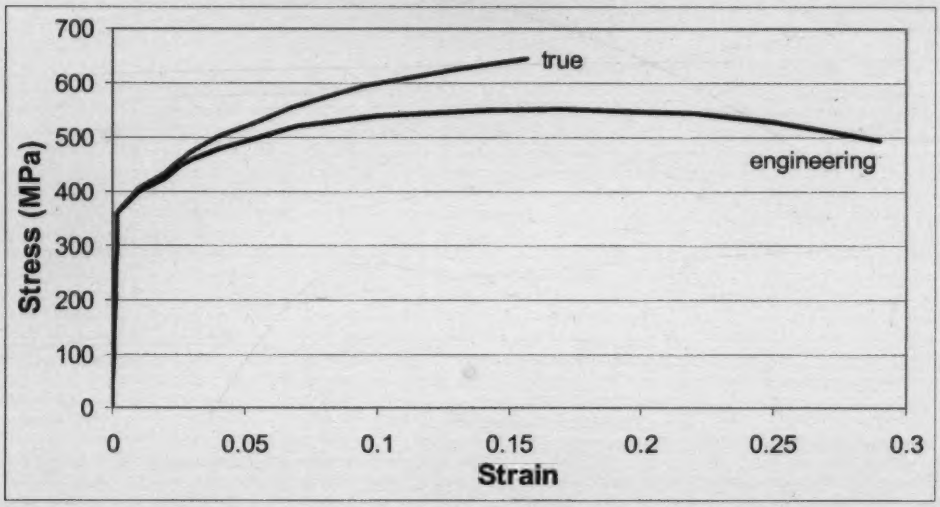

Figure 18 - Engineering and true stress - strain curves used for X-52 in finite element model

The finite element model was designed to include material properties of the steel that would change with hydrogen concentration, but a quantitative description of these changes is unavailable. The constant load elongation experiments conducted in air and in C2 solution described in Section 4 were carried out with the goal of developing an estimate of the effects of hydrogen on the stress-strain behaviour of this alloy.

As will be discussed in Section 4, the results of the constant load elongation tests did not provide information that could be translated into a predicted hydrogen dependent constitutive law. Thus, a hypothetical set of hydrogen dependent material properties was created and finite element modelling was carried out using this model. The hydrogen-induced material softening model is based on the models of Sofronis and Liang as described in Section 2.3.4 in which local flow stress decreases linearly with increasing hydrogen concentration. (Sofronis et al. 2001; Liang et al. 2003; Liang et al. 2004) Although this model of material properties is not based on real data, it reflects the nature of hydrogen enhanced localized plasticity (HELP) and is used with the aim of improving the current qualitative understanding of how HELP can participate in crack initiation.

The degree of HELP in the material property model depends on a softening parameter, ξ, used in the work of Sofronis and Liang as the factor by which the yield stress of the material is decreased when the hydrogen concentration is at a maximum. In the present work, the range of concentrations used in the material property models was fit to the range of hydrogen concentrations obtained in the finite element results. The bulk material was assumed to behave as if in air, with no effects of hydrogen. A typical bulk material hydrogen concentration of 3.43×10^{23} H atoms/m^3 or 0.074 ppm (obtained by biaxial loading of the material with a hoop stress of 97% SMYS) was set as the lower limit of the hydrogen dependent material property model. The concentration for the upper limit of the HELP model was set to be slightly larger than the maximum concentrations obtained in the models and this value was chosen as 4.00×10^{23} H atoms/m^3.

Section 3.1.6 provides more details about the assumptions made in order to arrive at these values. This method of choosing a range of concentrations is in contrast to the models of Sofronis and Liang, which use a range from zero hydrogen concentration to hydrogen saturation (one H atom in every available solvent atom position).

A range of softening parameters between zero and one were tested in the iterative process of applying hydrogen dependent material properties to the finite element model and a value of 0.5 was selected for use as it created sufficient softening to be noticeable and comparable between different cases without being too extreme and making the material very ductile. This value means that a material with the maximum hydrogen concentration (4.00×10^{23} H atoms/m^3) will have one-half the yield strength of the material without hydrogen enrichment (3.43×10^{23} H atoms/m^3 or less), and will exhibit the same strain hardening behaviour. The softening is linearly related to concentration, so a material that has a hydrogen concentration of 3.54×10^{23} H atoms/m^3 (20% of the way between the lower and upper concentration limits) will have a yield strength 10% lower than that of the material without hydrogen effects.

The stress-strain curves used to represent the hydrogen dependent material properties at the bulk condition, the maximum hydrogen condition and levels between these conditions are plotted in Figure 19. The stress and strain points used to create this plot are listed in Table 11.

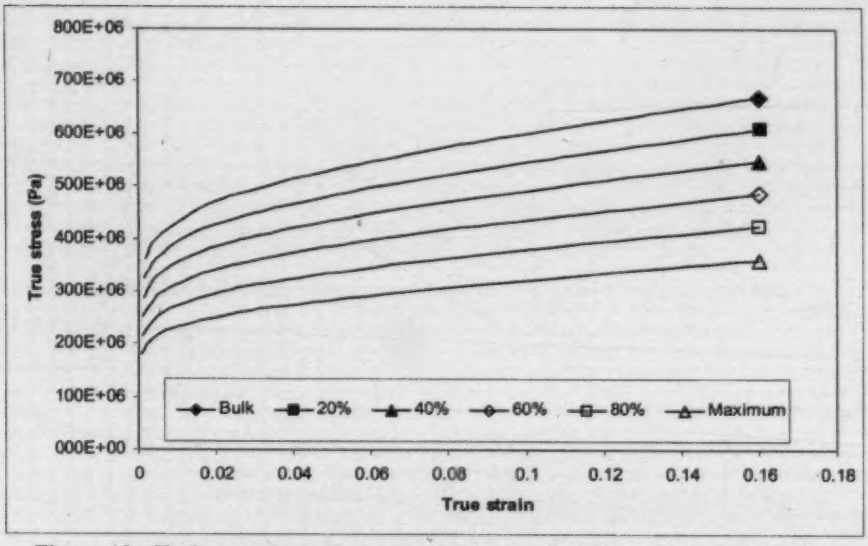

Figure 19 - Hydrogen dependent material properties, 0.5 softening parameter

Table 11 – Stress - strain data for hydrogen dependent material properties, 0.5 softening parameter

Stress (MPa)	Strain	Stress (MPa)	Strain	Stress (MPa)	Strain
Bulk		**20%**		**40%**	
361	0.0017	325	0.0016	288	0.0014
402	0.0050	362	0.0045	301	0.0021
457	0.0161	405	0.0128	353	0.0097
482	0.0247	484	0.0508	376	0.0169
523	0.0454	518	0.0767	401	0.0284
574	0.0799	538	0.0935	445	0.0588
641	0.1348	560	0.1132	504	0.1139
670	0.1602	609	0.1602	548	0.1602
60%		**80%**		**Maximum**	
252	0.0012	216	0.0010	180	0.0009
289	0.0046	273	0.0097	232	0.0100
313	0.0096	308	0.0275	256	0.0230
324	0.0132	322	0.0380	284	0.0489
361	0.0320	354	0.0698	300	0.0697
391	0.0551	373	0.0930	320	0.0975
449	0.1165	396	0.1224	343	0.1344
486	0.1600	423	0.1600	359	0.1601

3.1.5. Stresses Applied

As discussed in Section 2.2, pipelines are operated with an internal pressure limit to maintain a pipe hoop stress less than a specified fraction of the material's SMYS. Most pipelines have a hoop stress limit of 72% SMYS, calculated from internal operating pressure. However, residual stresses and local stress raisers can significantly increase the local effective stress in the pipe. An operating hoop stress of 72% SMYS and a residual stress of 25% SMYS (Roy et al. 1993) were used as representative maximum local hoop stress loading conditions for the current finite element model, combining to give 97% SMYS as the effective hoop stress. The two-dimensional model was stressed uniaxially at 97% SMYS in a direction perpendicular to the notch. For the three-dimensional models, a hoop stress of 97% SMYS was applied, and two cases of axial loading conditions were considered: axial stresses equal to one-half the hoop stresses (representing an idealized "capped-end" condition) and zero axial stresses (representing an idealized "open-end" condition). These two axial load cases also give the realistic extremes in the balance between dilatational and deviatoric stresses in the material.

3.1.6. Coupling of Hydrogen Concentrations and Material Softening

Several assumptions are necessary to be able to calculate the hydrogen concentration in the model using the hydrostatic stress and plastic strain data. For this work, the material will be assumed to be at a temperature of 300 K which is a reasonable assumption to reflect pipeline conditions and also allows use of measurements from a number of other workers' experimental results. (Sofronis and McMeeking 1989; Krom et al. 1999) Buried pipelines have typical temperatures near 280 K. The current model is meant to simulate conditions in X-52 steel at open circuit potential and 300 K, in a typical groundwater with a pH of approximately 6.5. To determine the appropriate C_L^o value to be used, the comparison of experimental measurements of this value by a number of workers was used. This comparison was shown in Figure 9 and Table 7. The measurements from those tests which most closely matched the current model

conditions were considered. An average value of 3.0 $x10^{23}$ H atoms/m^3 was selected for use throughout the current model. A horizontal dashed line in Figure 9 indicates this value for comparison to values reported in the literature. Some work was carried out to understand the sensitivities of the model results to this assumption, and this is addressed in Section 6.1.

Section 2.4.3 gave published values of trap densities for both pure iron and pipeline steels. While the trap densities for these two categories of materials are very different, finite element work modelling high strength steel has been carried out in the past using the trap densities of pure iron. (Sofronis and McMeeking 1989) The present work seeks to understand the effects of trap density on total hydrogen concentrations. Modelling was completed using both types of trap densities. For trapping representative of pure iron, the relation between plastic strain and trap density as expressed in Equation (22) was used in the finite model. For trap densities thought to be more representative of the carbide interface trapping in X-52 steel in near-neutral pH conditions, a trap density of 3.3 $x10^{25}$ traps/m^3 (7.11 ppm) was used. At this level of trap density, changes in dislocation trap densities due to plastic strain are negligible. For example, an increase of roughly 1.3 $x10^{23}$ dislocation traps/m^3 for 50% plastic strain, as measured by Kumnick and Johnson (1980) creates less than 0.5% change in the total number of trap sites if $3.0x10^{25}$ carbide interface trap sites exist in each cubic meter of the material.

When comparing traps at carbide interfaces with those present in ferrite, it is important to keep in mind that hydrogen trapped at carbide interfaces may not raise the hydrogen level in the primary ferrite regions. A large portion of NNpHSCC propagation occurs through primary ferrite regions. Thus, it is arguable that the dislocation traps must be considered for the primary ferrite and the carbide traps for cracking in the pearlite regions

Cyclic stressing can cause a material to fail more quickly and at much lower loads than static stressing. Fatigue loading causes X-52 to work harden, and dislocations build up in the areas of highest stress, such as at a corrosion pit or a crack tip. These extra dislocations can serve as trap sites for hydrogen, so that more trapped hydrogen may exist in the material after it is cyclically loaded in a near-neutral pH solution. A quantitative relationship between cyclic hardening of steel and trap density has not been determined. Modelling work was also done to investigate the effects on hydrogen concentrations if cyclic loading were to increase dislocation trap density by an order of magnitude or more. This modelling work is only applicable to the trap density model for pure iron, in which carbide interface traps are not present. The lack of an established relationship between cyclic loading and trap density necessitated that this work was qualitative in nature. In this case, Equation (22) was modified to multiply the trap density in areas with the highest plastic strain by either a factor of 10 or 30. Equation (26) is the form of the relationship between plastic strain and trap density that was used in the case of trap density being multiplied by a factor of 10.

$$N_T = \left[1 + 9\left(\frac{\varepsilon_p}{\varepsilon_{p\max}}\right)\right]\left[10^{\left(23.26 - 2.33e^{-5.5\varepsilon_p}\right)}\right] \tag{26}$$

The hydrogen concentrations resulting from stresses and strains in the material and the hydrogen induced changes to the material constitutive behaviour form a coupled problem. This coupled nature of these two systems (hydrogen concentration and stress-strain behaviour) was treated using an iterative approach. A finite element model of the corrosion pit, with material properties of X-52 in air (with no hydrogen effects) was analyzed. The stress and strain results for each node were exported to a spreadsheet, and the lattice and trapped hydrogen concentrations were calculated for these results using Equations (18) through (25). These concentrations were converted to a linear scale of temperatures and these temperatures, as well as a temperature-dependent table of material properties, which represented the change in stress-strain behaviour with

increasing hydrogen concentration, were used to formulate a new finite element model. This process was repeated until the results had converged to steady values, a process that typically was complete within three iterations. Figure 20 illustrates the iterative process used to couple hydrogen concentrations and material properties in the finite element model.

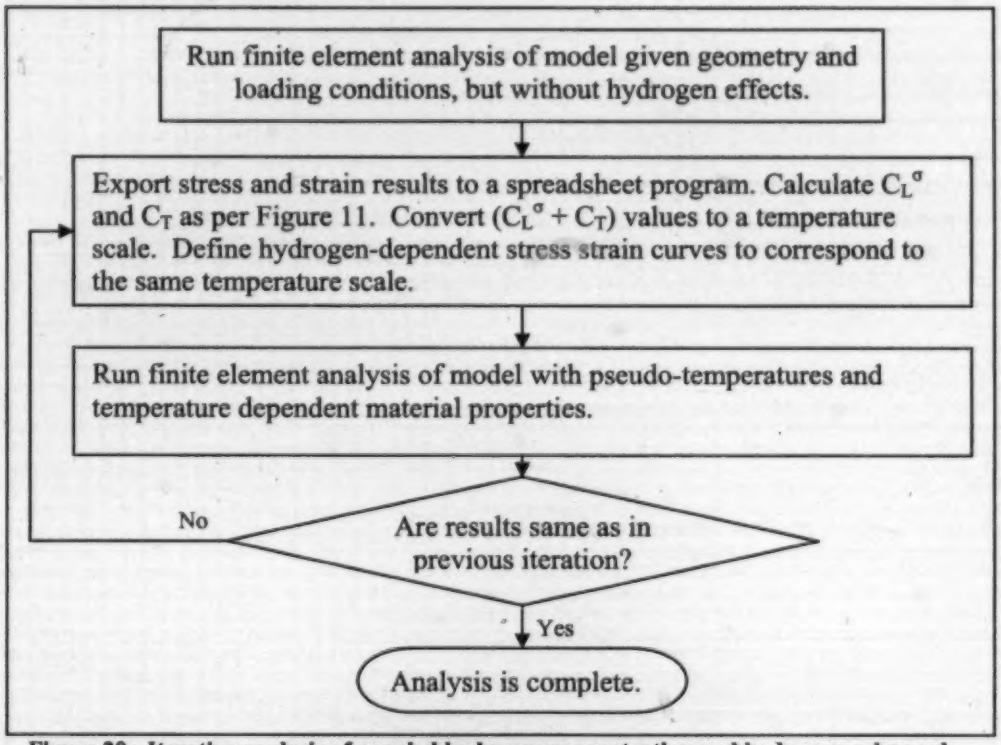
Run finite element analysis of model given geometry and loading conditions, but without hydrogen effects.
Export stress and strain results to a spreadsheet program. Calculate C_L^σ and C_T as per Figure 11. Convert (C_L^σ + C_T) values to a temperature scale. Define hydrogen-dependent stress strain curves to correspond to the same temperature scale.
Run finite element analysis of model with pseudo-temperatures and temperature dependent material properties.
Are results same as in previous iteration?
No
Yes
Analysis is complete.

Figure 20 - Iterative analysis of coupled hydrogen concentration and hydrogen enhanced localized plasticity problem

The system of hydrogen-dependent material properties used in the present work was based on the equations used by Liang et al. to relate hydrogen concentration to reduced yield and flow stresses. (Sofronis et al. 2001; Liang et al. 2003; Liang et al. 2004) This model is described in Section 3.1.4 and the hydrogen-dependent stress-strain behaviour used in the model is shown in Figure 19 and Table 11.

3.2. Constant Load Extension Test Methods

Cylindrical samples of X-52 steel were machined from a section of 36" pipe that had been removed from service. The long dimension of the samples was aligned

with the longitudinal direction of the pipe. The dimensions of the samples are shown in Figure 21. The steel was tested in the as-received condition.

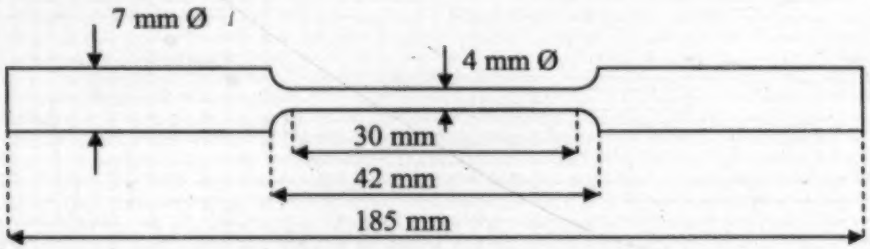

Figure 21 - Dimensions of cylindrical samples used for constant load extension tests

Tests were conducted using a closed loop hydraulic testing machine (INSTRON 8516) in a temperature-controlled laboratory set at 22°C. The tests were controlled and the test data was recorded with Instron WaveMaker-Runtime software.

Three tensile tests were conducted to establish the stress-strain behaviour of the steel. The samples were strained at 2%/min (3.33×10^{-4} /s) and a 25 mm extensometer strain gauge was used for the first 5% strain in the tests.

The constant load extension test samples were strained to 4% total strain, and then the system was switched from displacement control to load control, and the load was held at a constant value for the remainder of the test period. Constant load tests were conducted in two conditions. One set of tests were conducted in air and were held at constant load for 12 hours. Another set of samples were exposed to C2 solution with a 5% CO_2/95% N_2 gas mixture, loaded immediately and were then held at constant load for 36 hours to allow time for hydrogen ingress to reach equilibrium conditions. The first test in solution was held at constant load for 72 hours, which was calculated to be sufficient time for the hydrogen concentration to reach equilibrium throughout the sample, based on estimated hydrogen diffusion rates. The time required for creep exhaustion in this test allowed the load hold time for the following two tests in solution to be reduced to 36 hours.

3.3. Hydrogen Content Determination Test Methods

Tensile samples from five different test conditions were analyzed to measure the total hydrogen concentration in the samples. The five test conditions are described below.

3.3.1. "Air" samples

Two X-52 tensile samples were tested which had been previously strained to 4% in air and then stored in air at room temperature for more than a week. Three test specimens were cut from each gauge section using bolt cutters. This cutting method was chosen because it caused a very minimal heat input to the samples and allowed the cutting to be completed very quickly. The hydrogen concentration of these samples was determined. These samples are referred to as the "air" samples.

3.3.2. "C2" samples

Two X-52 tensile specimens were exposed to C2 solution with a 5% CO_2/95% N_2 gas mixture for 72 hours, then strained to 4%, held at constant load in the solution for 8 hours, and then unloaded and stored in liquid nitrogen until hydrogen content testing. The gauge length of each sample was cut into four samples using bolt cutters. Two tensile samples of this type were tested because the scatter in the measured hydrogen contents from the the first of these samples was thought to be too great, and a second sample was then tested in order to provide more data and improve the accuracy of the average hydrogen content calculated. These samples are referred to as the "C2" samples.

3.3.3. "C2 plus poison" samples

The third type of sample was exposed to C2 solution with 250 ppm As_2O_3 (a hydrogen recombination poison) dissolved in the solution for 72 hours before loading. During this time, a potentiostat was also connected to the tensile sample to impose a cathodic potential of -1100 mV SCE. A 5% CO_2/95% N_2 sparging gas mixture was bubbled through the test solution. The sample was kept in solution, with the potentiostat attached, as it was loaded into the INSTRON and

strained to 4%, held at constant load for 8 hours and then unloaded and stored in liquid nitrogen until hydrogen content testing. The gauge length of each tensile specimen was cut into four pieces using bolt cutters.

It is important to note that while the imposed potential was effectively applied throughout the 72-hour exposure period, this was not the case during the 8-hour loading period. The test sample was not electrically insulated from the metal hydraulic grips of the tensile test machine. The potentiostat would have attempted to maintain the imposed cathodic potential, but the actual potential imposed on the tensile specimen during loading is unknown. This sample is referred to as the "C2 plus poison" sample.

The potential used for electrochemical charging was selected based on the results of Parkins and Beavers (2003) relating charging potential and hydrogen concentration for X-52 in three NS4 solutions of different pH. Figure 8 shows this relationship. Maximum hydrogen concentrations are achieved for potentials between -900 and -1100 mV SCE.

3.3.4. "C2, no stress" samples

Three samples were cut from the grip section of an X-52 tensile specimen that had been stored in air at room temperature for more than one month. The samples were cut using a hacksaw rather than bolt cutters, and the cutting process was interrupted frequently to allow the steel to cool. This cutting method was necessary because the diameter of these samples was too large to fit in the bolt cutters. These samples were exposed to C2 solution with a 5% CO_2/95% N_2 gas mixture for 72 hours before hydrogen content testing. These samples are referred to as the "C2, no stress" samples.

3.3.5. "C2, no stress, previous strain" samples

Three samples were cut from the gauge length of an X-52 tensile specimen that had been previously strained to 4% and then stored in air at room temperature for more than one month. The samples were cut using a hacksaw rather than bolt

cutters, and the cutting process was interrupted frequently to allow the steel to cool. These samples were exposed to C2 solution with a 5% CO_2/95% N_2 gas mixture for 72 hours before hydrogen content testing. These samples are referred to as the "C2, no stress, previous strain" samples.

3.3.6. LECO RH-402 operation

This hydrogen content testing was carried out using the LECO RH-402 Hydrogen Analyzer. The hydrogen concentration in each test sample was determined by the hot extraction method. This type of analysis heats the samples enough for all hydrogen (both lattice and trapped) to be extracted without melting the steel. Samples are placed in quartz crucibles and heated in a sealed induction furnace. The gases released during heating leave the furnace carried by pure nitrogen gas and are cleaned as they flow through reagent tubes that remove water, oxygen, carbon monoxide and carbon dioxide. The hydrogen content of the sample is determined by comparison of the thermal conductivity of the gas after leaving the reagent tube with that of pure nitrogen gas. The thermal conductivities of common gases are listed in Table 12. (LECO 2000) Figure 22 is a flow chart illustrating the operation of the hydrogen analyzer.

Table 12 – Thermal conductivity of gases at STP

Gas	Symbol	Molecular Weight	Thermal Conductivity (calories / cm sec °C) x10^5
Hydrogen	H_2	2	39
Helium	He	4	33
Neon	Ne	20	10.4
Oxygen	O_2	32	5.7
Nitrogen	N_2	28	5.6
Air (Dry)	Air	29	5.4
Carbon Monoxide	CO	28	5.4
Water Vapor	H_2O	18	4.0
Argon	Ar	40	3.8
Carbon Dioxide	CO_2	44	3.3
Sulfur Dioxide	SO_2	64	4.6

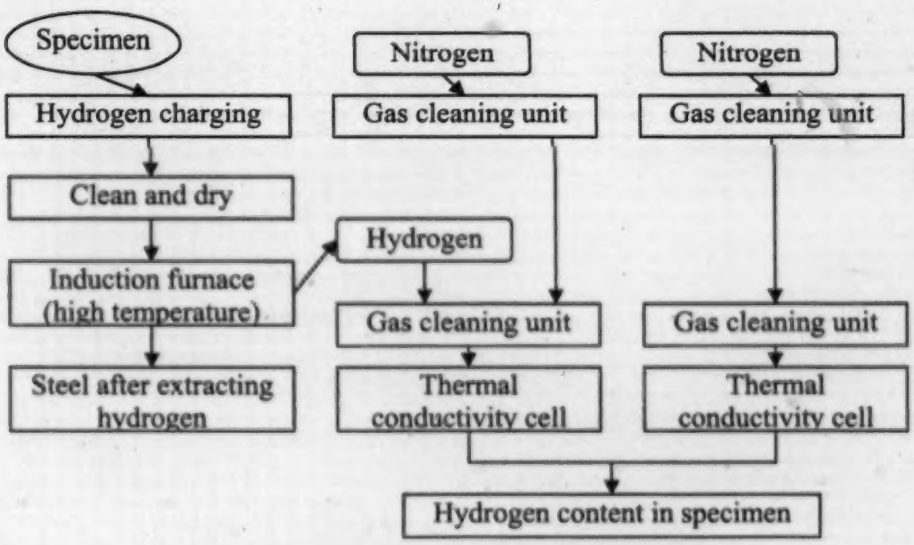

Figure 22 - Flow chart of hydrogen analyzer operation

The hydrogen analyzer was calibrated before each day of testing, using standard hydrogen samples containing 5.4 ± 0.4 ppm H_2. If a new lot of crucibles were to be used, or if the nitrogen gas supply was changed, it was also necessary to analyze blank runs before the calibration was carried out. The blanks are analysis runs in which only the quartz crucibles and no samples are put into the induction furnace. This is a means to identify the background hydrogen noise in the system from the crucibles, the supply gas or other sources.

One standard sample (5.4 ± 0.4 ppm H_2) was cooled by exposure to liquid nitrogen and then tested to evaluate the effects of the low temperature and surface frost formation on the hydrogen analysis results.

After being removed from the Instron, the three types of samples that had been held at constant stress were stored in liquid nitrogen until being tested using the LECO. Two to three minutes elapsed between the specimen being removed from the test solution and being immersed in the liquid nitrogen. This time was required to remove the specimen from the test cell and transfer it to the dewar containing liquid nitrogen. The specimen gauge length has a radius of 2 mm. As

shown in Figure 23, estimates of the distance over which hydrogen could diffuse during a two to three minute exposure to laboratory air after being removed from the test solution range between 0.04 and 0.06 mm, which is less than 3% of the specimen radius, or 6% of the specimen cross-sectional area.

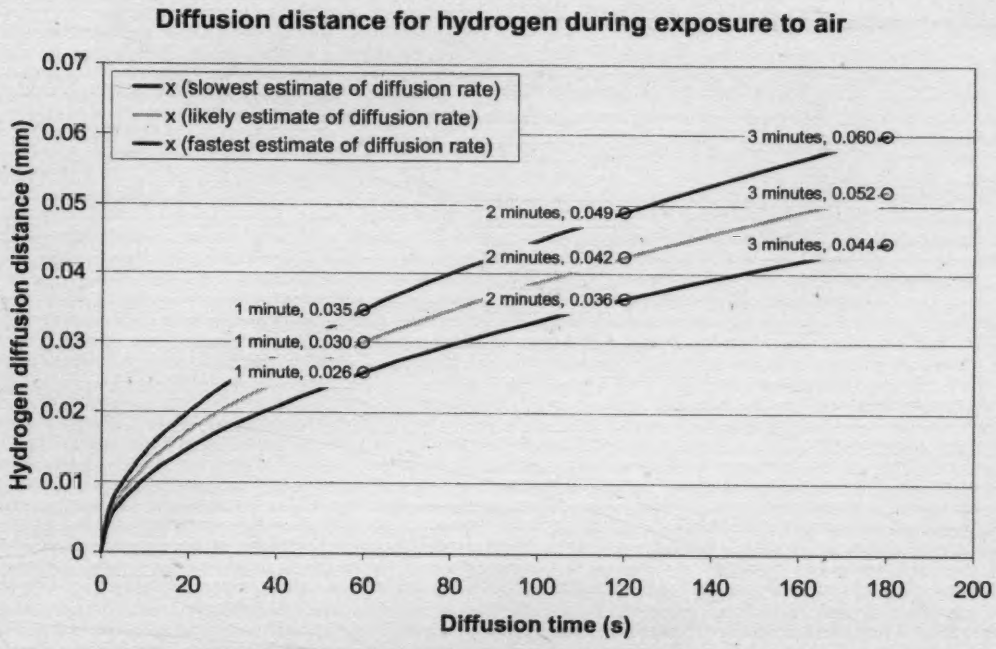

Figure 23 - Estimate of hydrogen diffusion distance possible while transferring specimen from test solution to liquid nitrogen

For the "C2" and "C2 plus poison" specimens, the gauge lengths were cut into three medium samples (0.6 to 1.5 grams) and one small sample (less than 0.5 grams). The small sample was allowed to come to room temperature, while the medium samples were returned to liquid nitrogen until just before they were placed in the induction furnace of the hydrogen analyzer. The surfaces of the tensile samples were cleaned using acetone and a cotton cloth before the gauge lengths were sectioned using bolt cutters. The samples tested and their conditions are summarized below in Table 13.

Table 13 – Samples tested in LECO RH-402 hydrogen analyzer

Sample ID Code	Preparation	Mass
Std N2	Hydrogen standard sample cooled in liquid N_2	1.001 g
Air 1	Strained to 4% in air, unloaded and stored in air	0.9132 g
Air 2		0.8302 g
Air 3		0.9703 g
C2 1	Exposed to C2 solution for 72 hours, then strained to 4% held at constant load for 8 hours while in solution.	1.2245 g
C2 2		0.7783 g
C2 3		0.5811 g
C2 4		0.4410 g
C2 5		0.8717 g
C2 6		0.7420 g
R.T. C2 1		0.7783 g
R.T. C2 2		0.7005 g
C2 plus poison 1	Exposed to C2 solution with 250 ppm As_2O_3, potential of -1100 mV SCE imposed for 72 hours; then strained to 4%, held at constant load for 8 hours while in solution	0.7627 g
C2 plus poison 2		0.6324 g
C2 plus poison 3		1.2453 g
R.T.C2 plus poison		0.4222 g
C2, no stress 1	Exposed to C2 solution for 72 hours	2.1032 g
C2, no stress 2		1.6656 g
C2, no stress 3		1.5722 g
C2, no stress, previous strain 1	Strained to 4%, unloaded, exposed to C2 solution for 72 hours	0.4826 g
C2, no stress, previous strain 2		0.6330 g
C2, no stress, previous strain 3		0.6434 g

4. CONSTANT LOAD EXTENSION TEST RESULTS

Three tensile tests were carried out to establish the stress-strain behaviour of the steel. The results of these tests are plotted in Figure 24. The main characteristics of the results from each test are summarized in Table 14.

Table 14 – Mechanical properties of tested X-52 steel

Test	Yield strength by 0.2% offset	Uniform strain (onset of necking)	Ultimate strength	Failure strain
1	366 MPa	16%	585 MPa	27.9 %
2	378 MPa	13%	583 MPa	25.2 %
3	348 MPa	15%	582 MPa	28.1 %

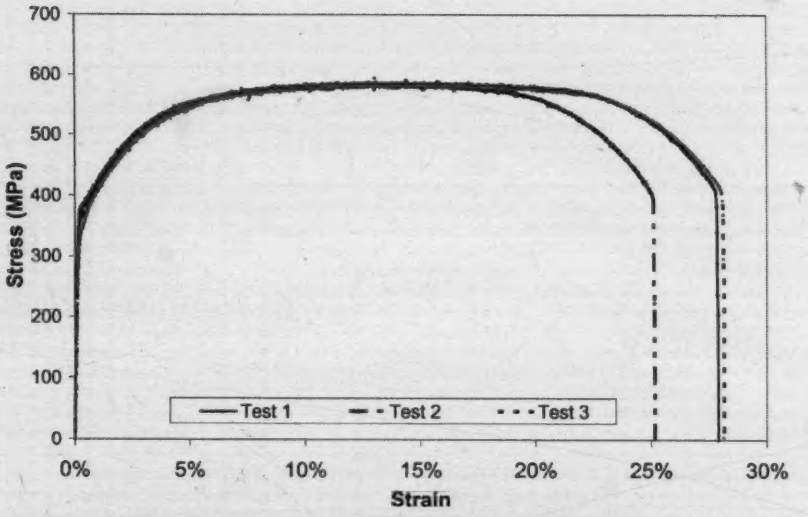

Figure 24 - Results of tensile tests on cylindrical X-52 samples

The constant load tests in air showed an average room temperature creep of 0.92%. Although the constant load condition was maintained for 10 hours, more than 95% of the total creep occurred in the first 2 hours of this period.

The constant load tests in the C2 solution showed an average room temperature creep strain of 0.98%. The first test was held for 72 hours, based on an estimate of the time required for hydrogen in solution to diffuse to the centre of the 4 mm diameter gauge section using Equation (16). However, the results from this first test were very similar to those from the tests in air. In this test, more than 95% of the room temperature creep strain occurred in the first 3 hours of the constant load period and no measurable change in strain was recorded after the first 10 hours of the test. Based on these observations, the duration of the second and third constant load tests in C2 solution was reduced to 36 hours.

The changes in strain during the constant load tests both in air and in C2 solution are shown in Figure 25 and the final room temperature creep strains from each test are compared in Figure 26.

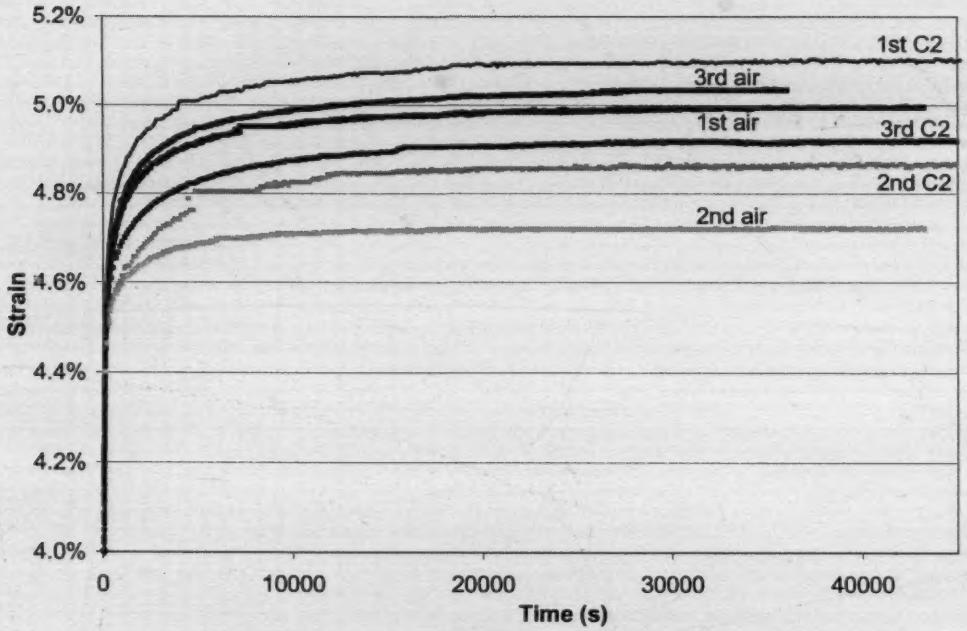

Figure 25- Strain vs. time for constant load tests in air and in C2 solution

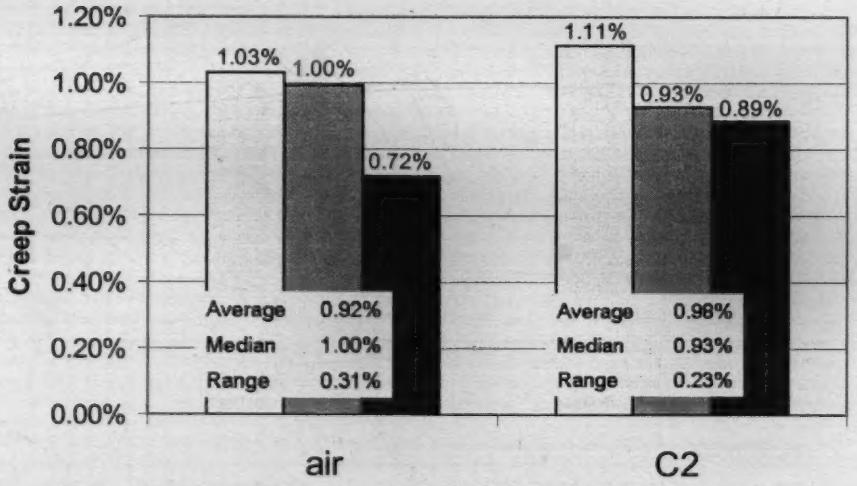

Figure 26 - Creep strains for constant load tests in air and in C2 solution

5. HYDROGEN CONTENT DETERMINATION RESULTS

Using the LECO RH-402 Hydrogen Analyzer, sixteen samples were tested to measure their hydrogen content. The results of these tests are given in Table 15. The details of preparation for each sample are summarized in Table 13.

Table 15 – Results of Hydrogen Content Tests using LECO RH-402 Hydrogen Analyzer

Sample ID Code	H (ppm)	H (H atoms/m^3)	Test Time (s)	Peak Rate (units unknown)
Std N2	5.50	2.55×10^{25}	517	41
Air 1	0.628	2.92×10^{24}	250	13
Air 2	0.736	3.42×10^{24}	250	31
Air 3	0.346	1.61×10^{24}	250	11
C2 1	10.2	4.75×10^{25}	250	924
C2 2	2.45	1.14×10^{25}	250	153
C2 3	6.22	2.79×10^{25}	250	206
C2 4	11.1	5.15×10^{25}	250	882
C2 5	4.87	2.26×10^{25}	250	413
C2 6	4.83	2.24×10^{25}	250	417
R.T. C2 1	0.31	1.44×10^{24}	250	13
R.T. C2 2	1.24	5.76×10^{24}	250	70
C2 plus poison 1	9.08	4.22×10^{25}	250	233
C2 plus poison 2	8.46	3.93×10^{25}	250	273
C2 plus poison 3	3.41	1.58×10^{25}	250	460
R.T. C2 plus poison	2.01	9.33×10^{24}	250	53
C2, no stress 1	52.3	2.43×10^{26}	250	3764
C2, no stress 2	8.6	3.99×10^{25}	250	777
C2, no stress 3	2.7	1.25×10^{25}	250	269
C2, no stress, previous strain 1	88.7	4.12×10^{26}	250	1497
C2, no stress, previous strain 2	9.5	4.41×10^{25}	250	470
C2, no stress, previous strain 3	3.1	1.44×10^{25}	250	116

There are some very apparent outlying data points in the above results. Work was carried out to identify or understand the source of this experimental error. These attempts included replacement of the reagent chemicals (in case these were depleted or expired), improved cleaning of sample surfaces (in case surface carbonate deposits were creating problematic readings), testing the machine for leaks and omission of any organic solvents from the cleaning process (in case acetone or ethanol might not have fully evaporated from the steel surface before testing). None of these approaches was successful in resolving or identifying the problem. On each day of testing with the LECO RH-402, blank determination

runs and calibration runs were carried out. No abnormalities in these runs were ever observed. Appendix A shows a summary of all tests completed, in sequence, including blank determination and calibration runs.

The hydrogen content results and trends in the data are addressed in the discussion section, Section 7.2.

6. FINITE ELEMENT ANALYSIS RESULTS

6.1. Initial Hydrogen Concentration

The results of the finite element model are sensitive to the value of C_L^o, the initial unstressed lattice hydrogen concentration. Figure 9 illustrates that there is nearly a three order of magnitude range in measured values of C_L^o reported in the literature depending on test conditions and measurement methods.

While a value of 3.0×10^{23} H atoms/m^3 was used for the finite element model, some initial work was carried out to investigate the effect of this assumption on the model results.

The three-dimensional finite element model was solved for stress and strain results under 97% SMYS biaxial loading. The resulting hydrogen concentrations for this stressing condition were calculated for a range of initial hydrogen concentrations. This work was carried out with both the trap density model for pure iron (mainly dislocation trapping) and the trap density model for X-52 pipeline steel (mainly carbide interface trapping).

6.1.1. Effect of C_L^o Using Pure Iron Trap Densities

For trap densities representative of pure iron, Figure 27 shows how the resulting maximum lattice and trapped hydrogen concentrations and the fractional trap occupancy vary as the initial hydrogen concentration is varied from 1.2×10^{19} H atoms/m^3 to 2.3×10^{24} H atoms/m^3. These values were calculated using Equations (18) through (25).

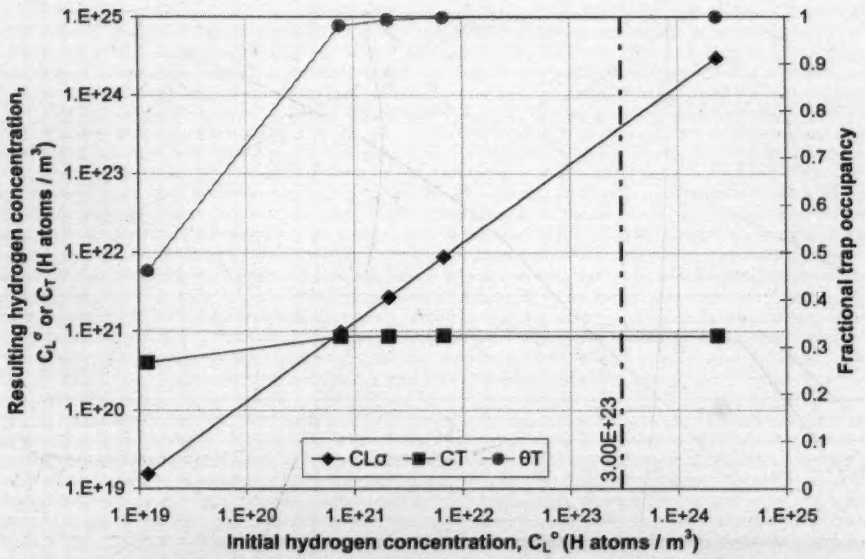

Figure 27 – Effect of initial hydrogen concentration on resulting calculated trapped and lattice hydrogen concentrations (pure iron trapping model)

For C_L^o values above roughly 7.5 x10^{20} H atoms/m^3, the majority of the trapping sites will be occupied, with the trap occupancy, θ_T, approaching 1. In this case, the lattice hydrogen profile will dominate the total hydrogen concentration profile. On the other hand, for low values of C_L^o, trapping will dominate the stressed hydrogen concentration profile. For the case evaluated with C_L^o as 1.2 x 10^{19} H atoms/m^3, the fractional trap occupancy was only 0.46 and yet the trapped hydrogen population was found to be larger than the interstitial lattice hydrogen population.

6.1.2. Effect of C_L^o Using Pipeline Steel Trap Densities

The calculations were repeated for a trap density representative of pipeline steel. Figure 28 shows the dependence of maximum lattice and trapped hydrogen concentrations and the fractional trap occupancy on the initial hydrogen concentration as it is varied from 3.0 x 10^{19} H atoms/m^3 to 3.0 x 10^{24} H atoms/m^3 when N_T = 3.3 x 10^{25} traps/m^3.

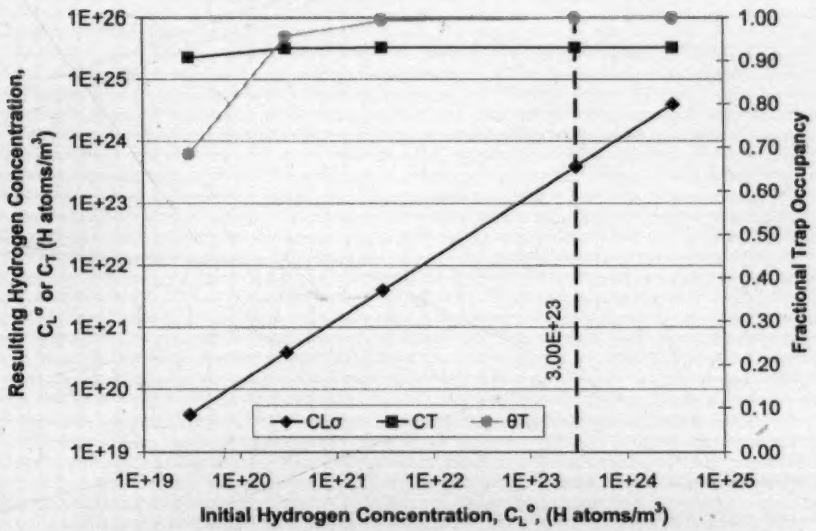

Figure 28 – Effect of initial hydrogen concentration on resulting calculated trapped and lattice hydrogen concentrations (pipeline steel trapping model)

For the entire range of C_L^o values shown, the trapped hydrogen concentration is significantly higher than the lattice hydrogen concentration. The majority of the trapping sites will be occupied (θ_T will approach 1) when C_L^o is above 3.0×10^{20} H atoms/m^3.

For the case that is understood to be most representative of X-52 pipeline steel in a near-neutral pH solution, with $C_L^o = 3.0 \times 10^{23}$ H atoms/m^3 (as discussed in Section 2.4.1) and $N_T = 3.3 \times 10^{25}$ traps/m^3 (as discussed in Section 2.4.3.2) the trapped hydrogen will dominate the total hydrogen concentration level.

The C_L^o value for which traps are almost completely saturated depends on the temperature, the hydrostatic stress condition, and the amount of plastic strain. For the temperature and range of loading conditions evaluated with the finite element model, the above results give important understanding of the hydrogen conditions based on the initial hydrogen concentration value given. It is clear that hydrogen traps will be saturated regardless of the trap density model that is used. This work was repeated with a hemiellipsoidal pit model to confirm that the observed trap saturation would occur at the same levels of C_L^o, independent of pit geometry.

In the case with lower trap densities as measured in pure iron, the hydrostatic stress profile will dominate the total hydrogen concentration levels when an initial hydrogen concentration of 3.0×10^{23} H atoms/m^3 is assumed.

Using the carbide interface trap densities as measured by Parkins and Beavers (2003), the trapped hydrogen population will exceed that of the lattice hydrogen by at least an order of magnitude.

6.2. Uniaxial vs. Biaxial Loading

Line pipe experiences hoop stress in direct proportion to the internal operating pressure of the pipeline. Axial stresses in the pipeline can also exist due to internal operating pressure, residual manufacturing stresses, or bending stresses due to ground settlement or landslides. Two loading conditions were investigated in the three-dimensional finite element modelling. The uniaxial stressing case represented only hoop stress due to internal pressure and residual stresses, with no axial stresses acting on the material. The biaxial case represented a hoop stress as well as an axial stress that was equal to half of the hoop stress. While axial stresses can exceed this level when the ground supporting the pipeline erodes, allowing bending stresses, the biaxial loading case is thought to be a reasonable upper bound in the modelling of a biaxial stress condition in an operating pipeline. It reflects the pipe stresses that would result from a "capped end" condition – if the pipe were to be closed on either end, so that the internal pressure acts on the pipe in both the circumferential and axial directions.

Hydrogen is present in iron and steel in both lattice and trap sites. Hydrogen exists in lattice positions and this concentration is greatly influenced by the hydrostatic (dilatational) stress in the material.

Using the trapping model for pure iron, dislocation traps are created through deformation that is caused by deviatoric stress in the material. Thus trapped

hydrogen concentrations are directly related to the level of deviatoric stress in the material. Any stress state can be expressed as the sum of a dilatational stress and a deviatoric stress. The von Mises stress is a common expression of the deviatoric stress.

$$\sigma_h = \tfrac{1}{3}(\sigma_1 + \sigma_2 + \sigma_3)$$
$$\sigma_{vm} = \frac{1}{\sqrt{2}}\sqrt{(\sigma_1 - \sigma_2)^2 + (\sigma_2 - \sigma_3)^2 + (\sigma_3 - \sigma_1)^2} \quad (27)$$

where

σ_h is the hydrostatic stress,

σ_{vm} is the von Mises stress, and

σ_1, σ_2, and σ_3 are the principal stresses.

For the trap densities measured in pipeline steels, the majority of traps exist at carbide interfaces in the microstructure. The total number of traps in the steel does not change significantly with an increase in deviatoric stress or plastic strain. However, the trap density in the primary ferrite will exhibit a significant increase with plastic strain as has been observed in tests using pure iron (Kumnick and Johnson 1980).

For the case of uniaxial loading, the hoop stress is the first principal stress and the second and third principal stresses are zero. Thus, the hydrostatic stress in the bulk of the material is equal to one-third of the hoop stress. The bulk von Mises or deviatoric stress is equal to the acting hoop stress. The stress case used in the majority of the study had a hoop stress equal to 97% of the specified minimum yield strength (SMYS) of the material, representing 72% SMYS operating stress and a local residual stress of 25% SMYS. The bulk hydrostatic stress for this uniaxial loading case is 32.3% SMYS. The SMYS of X-52 is 359 MPa so the bulk hydrostatic stress is 116 MPa. In a similar way, it can be calculated that the bulk von Mises stress in the material for the model of uniaxial loading is 97% SMYS, or 348 MPa.

For the case of biaxial loading, the hoop stress is the first principal stress, the axial stress is the second principal stress, and the third principal stress is zero. In this case, the hydrostatic stress in the bulk of the material is one-half of the hoop stress and the bulk von Mises stress is 87% of the hoop stress. With a hoop stress of 97% SMYS, the bulk hydrostatic stress is 49% SMYS, or 174.1 MPa, and the bulk von Mises stress is 84% SMYS or 302 MPa.

The local stress and strain conditions surrounding a geometric discontinuity on the surface of a pressurized pipe, as found by finite element analysis, are used to quantify the probable hydrogen concentration surrounding the discontinuity. Of course, these calculated hydrogen contents are estimates. Changes to the assumptions for initial hydrogen concentration (C_L^o), applied stress, trap density or material stress-strain behaviour would affect these results.

The HELP model predicts that the localized presence of hydrogen in steel can cause the material to experience increased plastic strain. If the constitutive behaviour of the steel is hydrogen dependent, the stresses and the hydrogen concentrations calculated near a pit will change in the iterative process of introducing hydrogen-dependent material properties. A first estimate of hydrogen levels is needed to begin this process, and these values provide important information about the conditions in the pipe material. Both the bulk hydrogen concentration in the material and the localized hydrogen concentration are calculated based on the stress-strain behaviour of the material in the absence of any hydrogen effects. These hydrogen concentration values were then used for investigating the iterative application of hydrogen-dependent material properties.

Table 16 summarizes the stress and strain results for a number of modelling cases carried out. The geometry, loading and material properties used for each case are given below the table in a list. The loading cases of uniaxial stressing or biaxial stressing at 97% SMYS hoop stress with no hydrogen effects are listed as cases B

and C respectively. Comparing the results of loading cases B and C, it can be seen that biaxial loading creates higher dilatational stresses (both bulk and maximum) than uniaxial loading. The von Mises stress in the bulk of the material is higher for uniaxial loading, but the maximum von Mises stress levels are similar for the two loading cases, as are the maximum strain values. The other variations of the finite element model included in this table are discussed later in Section 6.

Table 16 – Average and local maximum stresses for uniaxial and biaxial loading

Case	Brief description	Bulk von Mises stress (MPa)	Max von Mises stress (MPa)	Bulk hydro-static stress (MPa)	Max hydro-static pressure (MPa)	Max von Mises total strain
A	72% (SMYS), biaxial, hemisphere, no H dep.	224.9	367.5	129.2	248.1	0.26%
B	97%, uniaxial, hemisphere, no H dep.	348.2	376.0	116.1	208.2	0.47%
C	97%, biaxial, hemisphere, no H dep.	301.6	374.4	174.1	311.0	0.44%
D	97%, uniaxial, hemisphere, $\downarrow\sigma_y$ with $\uparrow$[H]	348.2	386.8	116.1	210.5	0.47%
E	97%, biaxial, hemisphere, $\downarrow\sigma_y$ with $\uparrow$[H]	301.6	383.2	174.1	296.5	0.49%
F	97%, uniaxial, hemisphere, base dissolution, no H dep.	348.2	424.9	116.1	364.7	1.68%
G	97%, biaxial, hemisphere, base dissolution, no H dep.	301.6	422.7	174.1	425.1	1.61%
H	97%, uniaxial, hemisphere, base dissolution, $\downarrow\sigma_y$ with $\uparrow$[H]	348.2	403.8	116.1	389.9	2.01%
I	97%, biaxial, hemisphere, base dissolution, $\downarrow\sigma_y$ with $\uparrow$[H]	301.6	397.0	174.1	387.1	2.10%
J	97%, uniaxial, hemiellipsoid, no H dep.	348.2	389.5	116.1	266.0	0.73%
K	97%, biaxial, hemiellipsoid, no H dep.	301.6	383.8	174.1	346.6	0.62%
L	97%, uniaxial, frustum, no H dep.	348.2	382.5	116.1	259.8	0.59%
M	97%, biaxial, frustum, no	301.6	378.9	174.1	314.7	0.54%

	H dep.					
N	97%, uniaxial, hemisphere with cylindrical dissolution, no H dep.	348.2	457.3	116.1	377.7	2.50%
O	97%, biaxial, hemisphere with cylindrical dissolution, no H dep.	301.6	430.3	174.1	449.7	1.86%

A. *72% SMYS, biaxial loading, hemisphere, no dependence of material properties on hydrogen concentration*
B. *97% SMYS, uniaxial loading, hemisphere, no dependence of material properties on hydrogen concentration*
C. *97% SMYS biaxial, smooth base, no H dep,*
D. *97% SMYS uniaxial, hemisphere, H dep*
E. *97% SMYS biaxial, hemisphere, H dep*
F. *97% SMYS uniaxial, hemisphere with base dissolution, no H dep,*
G. *97% SMYS biaxial, hemisphere with base dissolution, no H dep,*
H. *97% SMYS uniaxial, hemisphere with base dissolution, H dep,*
I. *97% SMYS biaxial, hemisphere with base dissolution, H dep,*
J. *97% SMYS uniaxial, hemiellipsoid, no H dep*
K. *97% SMYS biaxial, hemiellipsoid, no H dep*
L. *97% SMYS uniaxial, frustum, no H dep*
M. *97% SMYS, biaxial, frustum, no H dep*
N. *97% SMYS, uniaxial, hemisphere with cylindrical base dissolution, no H dep*
O. *97% SMYS, biaxial, hemisphere with cylindrical base dissolution, no H dep*

6.3. Sensitivity to Pit Geometry

The ability of a pit to initiate a crack is very dependent upon the geometry of the pit. Both 2D and 3D models were created to investigate the effects of pit geometry on the stress, strain, and hydrogen concentrations that result.

6.3.1. Three Dimensional Geometries

Five different three-dimensional geometries of corrosion pits were evaluated using the finite element model. These are a hemisphere, a hemisphere with a groove at its base (representing geometry changes caused by strain enhanced dissolution), a hemisphere with cylindrical dissolution at its base (also representing geometry changes due to strain enhanced dissolution), a hemiellipsoid and a rounded frustum. These geometries are illustrated in Figure 29. Each model geometry was evaluated with both uniaxial and biaxial loading,

to observe the interaction of different types of stress concentrations and the different loading conditions. The bulk and localized stresses found through these analyses are included in Table 16, listed as cases B, C, F. G, J, K, L, M, N and O. The maximum stresses calculated for each of the geometries are compared in Figure 30.

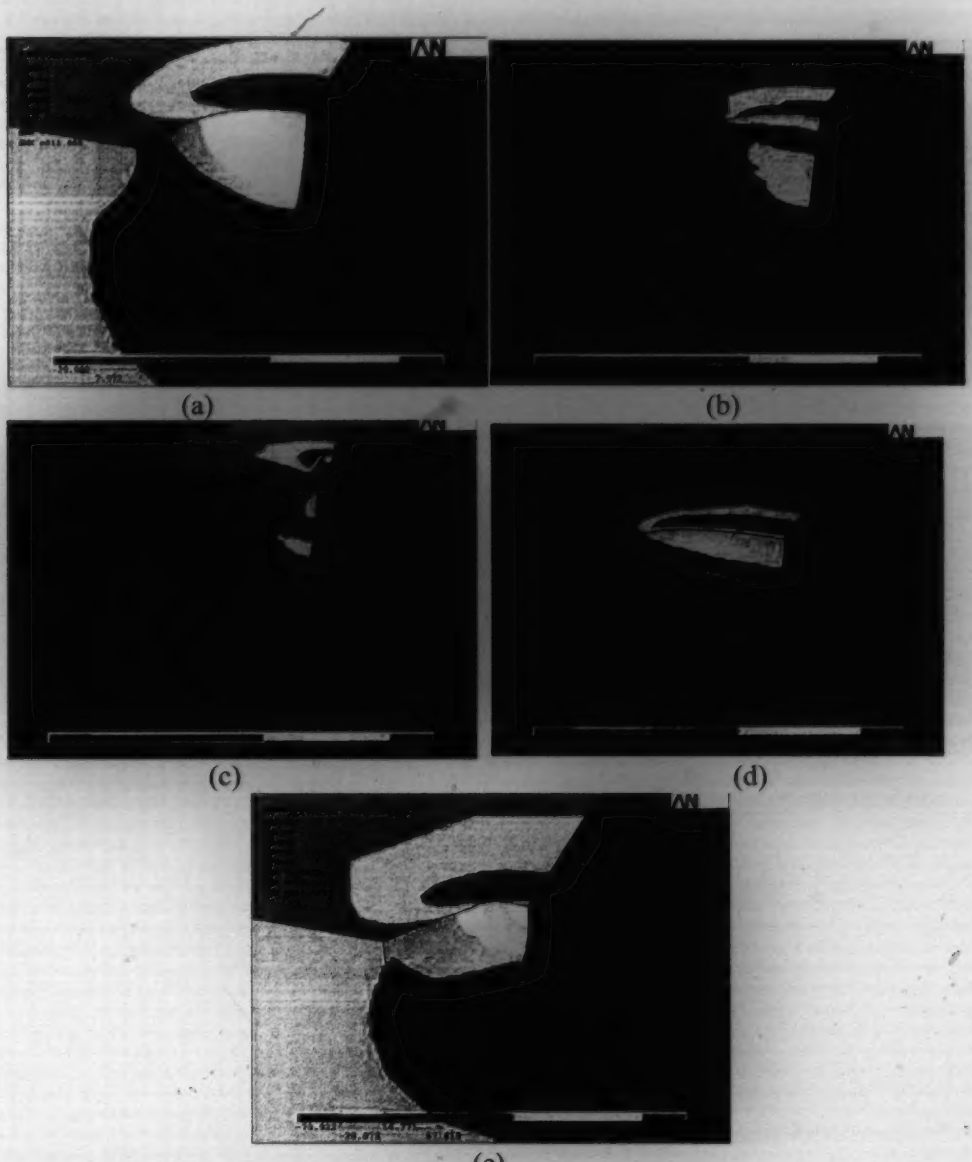

Figure 29 - Hydrostatic stresses from biaxial loading for pits:
(a) hemisphere (b) hemisphere with base dissolution (c) hemisphere with cylindrical dissolution (d) hemiellipsoid (e) frustum

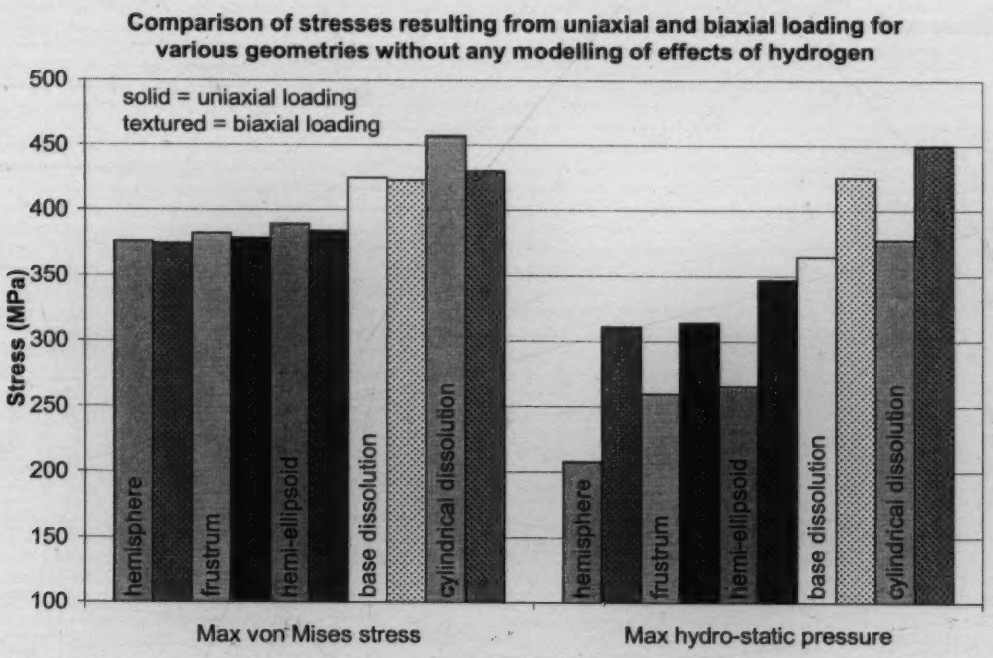

Figure 30 - Comparison of stresses resulting from uniaxial and biaxial loading for various geometries without any modelling of effects of hydrogen

6.3.2. Two Dimensional Geometries

A series of two-dimensional notch geometries were modeled to investigate the effect of geometry on the stress and strain conditions of a uniaxially loaded specimen with a surface flaw. These analyses were only used to find the effect of geometry changes on the stress and strain results due to loading; no hydrogen concentrations were calculated and no iterations with possible hydrogen-dependent material properties were carried out. The maximum von Mises stress, hydrostatic stress and plastic strain values were recorded for each of the cases modeled and these values have been compared to find trends in the results. These results are given here in Table 17. Several relationships were found between the stress and strain results and the geometries modeled.

A linear relationship exists between notch depth and maximum equivalent plastic strain at the notch tip. This relationship applies for both the notches with the straight walls and those with the angled walls – it seems that the change in wall

profile between these two types of notches does not affect either the maximum strain or maximum stress results. As shown in Figure 31, the six data points available for each type of notch give a good fit to the linear relationship, with the best fit line having an R^2 value of 0.998.

Relationships between notch depth and maximum hydrostatic and von Mises stresses can also be seen, but in these cases, the data appears slightly better fitted to a quadratic trend than a linear relationship. The hydrostatic stress versus notch depth plot, shown in Figure 32, can be fitted to a linear trendline with $R^2 = 0.9858$ or to a second order polynomial with $R^2 = 0.9977$. Similarly, the von Mises stress versus notch depth plot, shown in Figure 33, can be fitted to a linear trendline with $R^2 = 0.9689$ or to a second order polynomial with $R^2 = 0.9961$.

Table 17 – Stress and strain results for two dimensional notch finite element models

Notch depth (mm)	Tip radius (mm)	Mouth width (mm)	Max hydrostatic stress (MPa)	Max von Mises stress (MPa)	Max equivalent plastic strain
0.15	0.05	0.107	215.98	488.86	0.0329
0.25	0.05	0.121	227.05	520.48	0.0473
0.35	0.05	0.136	240.17	550.02	0.0623
0.55	0.05	0.164	258.367	587.38	0.0875
0.75	0.05	0.193	271.121	612.82	0.1126
0.95	0.05	0.221	285.94	642.34	0.1489
0.15	0.05	0.100	216.019	488.90	0.0330
0.25	0.05	0.100	226.926	522.55	0.0483
0.35	0.05	0.100	240.138	549.59	0.0620
0.55	0.05	0.100	258.405	587.13	0.0873
0.75	0.05	0.100	271.005	613.35	0.1132
0.95	0.05	0.100	285.808	640.13	0.1460
0.30	0.02	0.150	273.077	615.19	0.1143
0.30	0.03	0.150	258.946	587.47	0.0875
0.30	0.05	0.150	240.260	550.73	0.0626
0.30	0.07	0.150	228.527	525.89	0.0500
0.30	0.075	0.150	226.88	522.07	0.0481

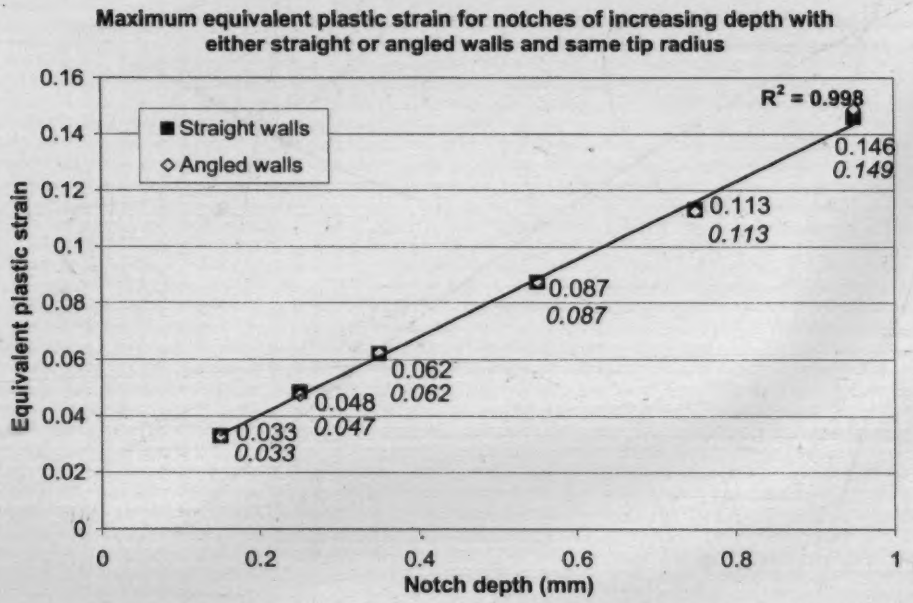

Figure 31 - Linear relationship between maximum equivalent plastic strain and 2D notch depth

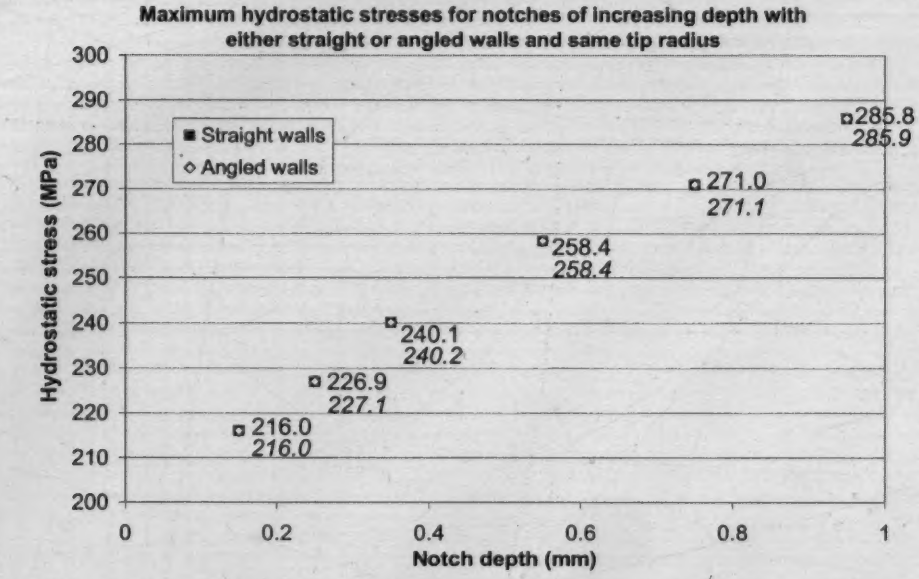

Figure 32 - Relationship between maximum hydrostatic stress and 2D notch depth

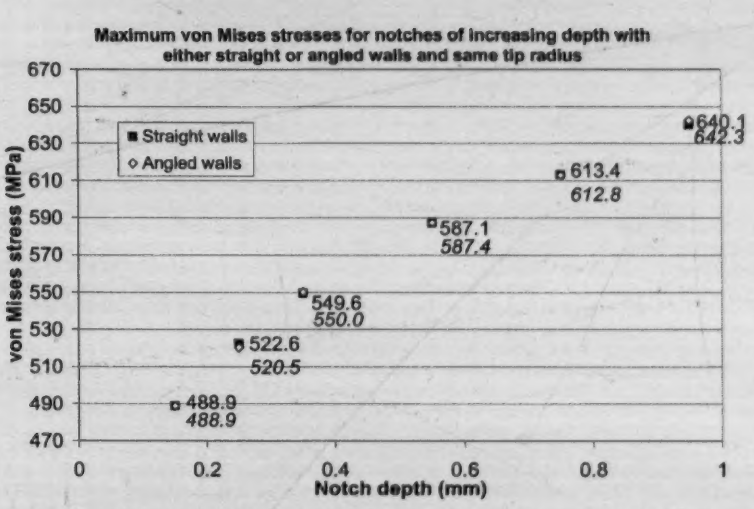

Figure 33 - Relationship between maximum von Mises stress and 2D notch depth

For the series of two-dimensional notches modeled with a range of notch tip radii, the stresses and strains at the notch tip decrease as the radius of the notch tip is increased. Figure 34 shows that a power equation, of the form $\varepsilon_{p,eq} = 0.0087\rho^{-0.658}$, fits the available data points very well, with $R^2 = 1$, where $\varepsilon_{p,eq}$ is the maximum equivalent plastic strain and ρ is the notch tip radius. The maximum hydrostatic stress and the maximum von Mises stress points fit a quadratic relationship with the notch tip radius, as shown in Figure 35.

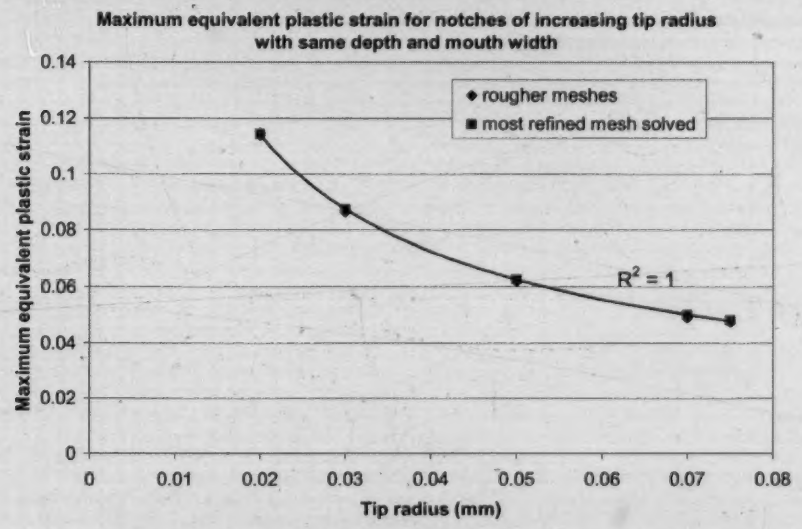
Maximum equivalent plastic strain for notches of increasing tip radius with same depth and mouth width
Maximum equivalent plastic strain
Tip radius (mm)
rougher meshes
most refined mesh solved
R² = 1

Figure 34 - Power relationship between maximum equivalent plastic strain and notch tip radius

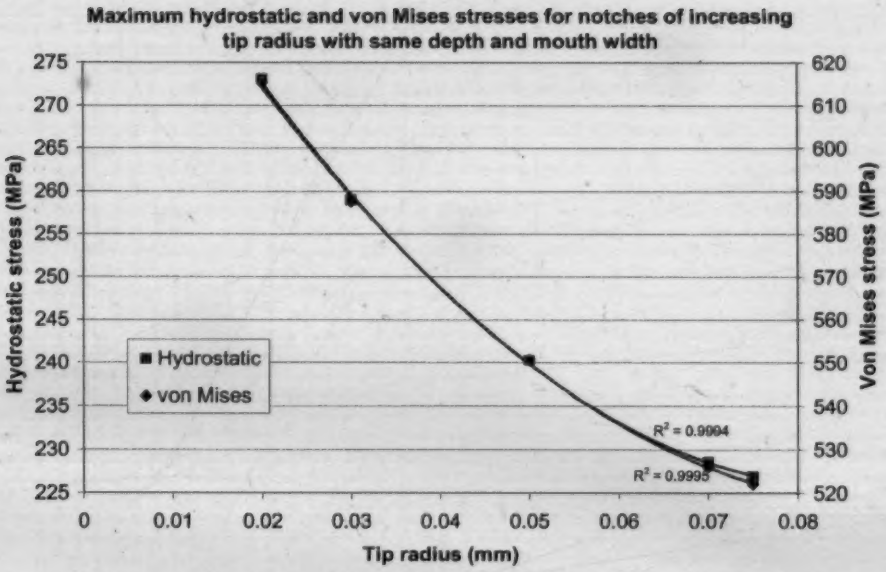

Figure 35 - Quadratic relationships between maximum stresses and notch tip radius

6.3.3. Comparison of Semi-circular Notch and Hemispherical Pit

The stress and strain results from a two-dimensional model of a semi-circular notch and a three-dimensional model of a hemispherical pit were compared. While the three-dimensional model represents a surface flaw of a finite size, the two-dimensional model actually represents a groove with a semicircular cross section that extends along the surface of a semi-infinite block. Thus, the 2D model is less constrained than the 3D model. Both models were subjected to a uniaxial load of 100% SMYS. Table 18 gives the maximum stresses and strains at the pit base for both finite element models.

Table 18 – Stress and strain results for 2D and 3D models of a hemispherical pit under 100% SMYS uniaxial loading

	Maximum hydrostatic stress (MPa)	Maximum von Mises stress (MPa)	Maximum von Mises total strain
3D	217.6	379.5	0.00538
2D	209.5	503.8	0.0416

6.4. Hydrogen Concentrations in Model

6.4.1. Hydrogen Concentrations without HELP

A number of finite element models with different geometries and loading conditions were solved and the hydrogen concentrations resulting from the stress and strain conditions were calculated. In this section of the work, it was assumed that the increased hydrogen concentrations had no effect on the stress-strain behaviour of the material. The bulk and maximum hydrogen concentrations were evaluated for the loading cases listed in Table 16 as A, B, C, F, G, J, K, L, M, N and O. These results are given in Table 19.

Figure 36 and Figure 37 show the differences in the maximum total hydrogen concentration between the different model cases, using the trap densities for pure iron and pipeline steel respectively. Figure 36 uses a linear scale on the y-axis whereas Figure 37 uses a logarithmic scale. The most striking difference between the two figures is the relative magnitude of lattice and trapped hydrogen concentrations with the two models for hydrogen trapping.

Table 19 – Hydrogen concentrations in models without HELP effects

Case	Brief description	Maximum (and Bulk) C_L^{σ} (H atoms/m^3)	Maximum (and Bulk) C_T, using N_T for pure iron (H atoms/m^3)	C_T, using N_T for X-52 (H atoms/m^3)
A	72% (SMYS), biaxial, hemisphere, no H dep.	3.66×10^{23} (3.33×10^{23})	9.18×10^{20} (8.51×10^{20})	3.3×10^{25}
B	97%, uniaxial, hemisphere, no H dep.	3.55×10^{23} (3.29×10^{23})	9.76×10^{20} (8.51×10^{20})	3.3×10^{25}
C	97%, biaxial, hemisphere, no H dep.	3.85×10^{23} (3.45×10^{23})	9.68×10^{20} (8.51×10^{20})	3.3×10^{25}
F	97%, uniaxial, hemisphere, base dissolution, no H dep.	4.02×10^{23} (3.29×10^{23})	1.37×10^{21} (8.51×10^{20})	3.3×10^{25}
G	97%, biaxial, hemisphere, base dissolution, no H dep.	4.22×10^{23} (3.45×10^{23})	1.34×10^{21} (8.51×10^{20})	3.3×10^{25}
J	97%, uniaxial, hemiellipsoid, no H dep.	3.71×10^{23} (3.29×10^{23})	1.05×10^{21} (8.51×10^{20})	3.3×10^{25}
K	97%, biaxial, hemiellipsoid, no H dep.	3.96×10^{23} (3.45×10^{23})	1.02×10^{21} (8.51×10^{20})	3.3×10^{25}
L	97%, uniaxial, frustum, no H dep.	3.69×10^{23} (3.29×10^{23})	1.01×10^{21} (8.51×10^{20})	3.3×10^{25}
M	97%, biaxial, frustum, no H dep.	3.86×10^{23} (3.45×10^{23})	9.96×10^{20} (8.51×10^{20})	3.3×10^{25}
N	97%, uniaxial, hemisphere with cylindrical dissolution, no H dep.	4.06×10^{23} (3.29×10^{23})	1.70×10^{21} (8.51×10^{20})	3.3×10^{25}
O	97%, biaxial, hemisphere with cylindrical dissolution, no H dep.	4.30×10^{23} (3.45×10^{23})	1.43×10^{20} (8.51×10^{20})	3.3×10^{25}

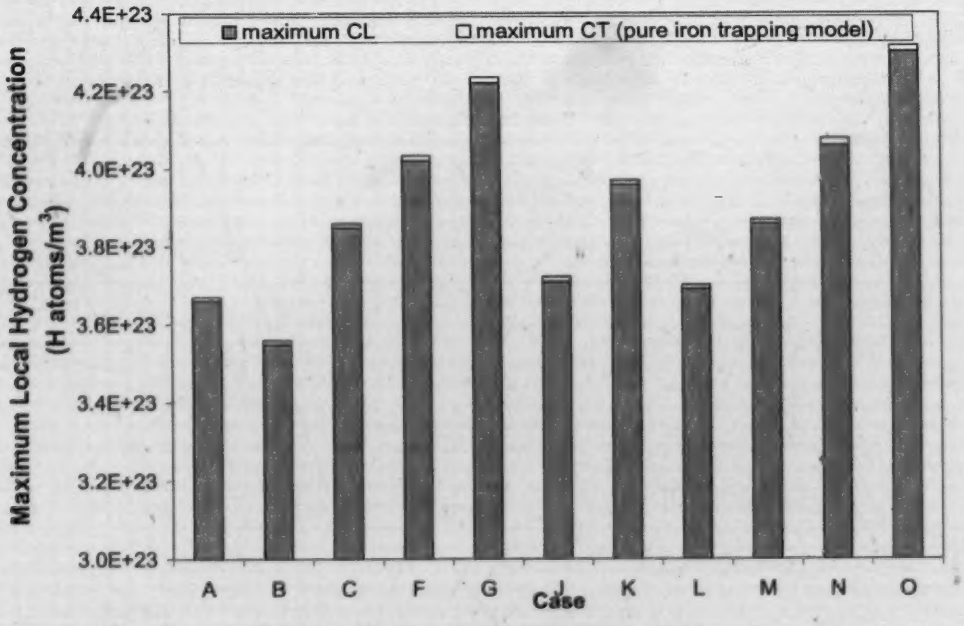

Figure 36 – Contributions of lattice and trapped hydrogen to maximum local concentration, using pure iron trap density model

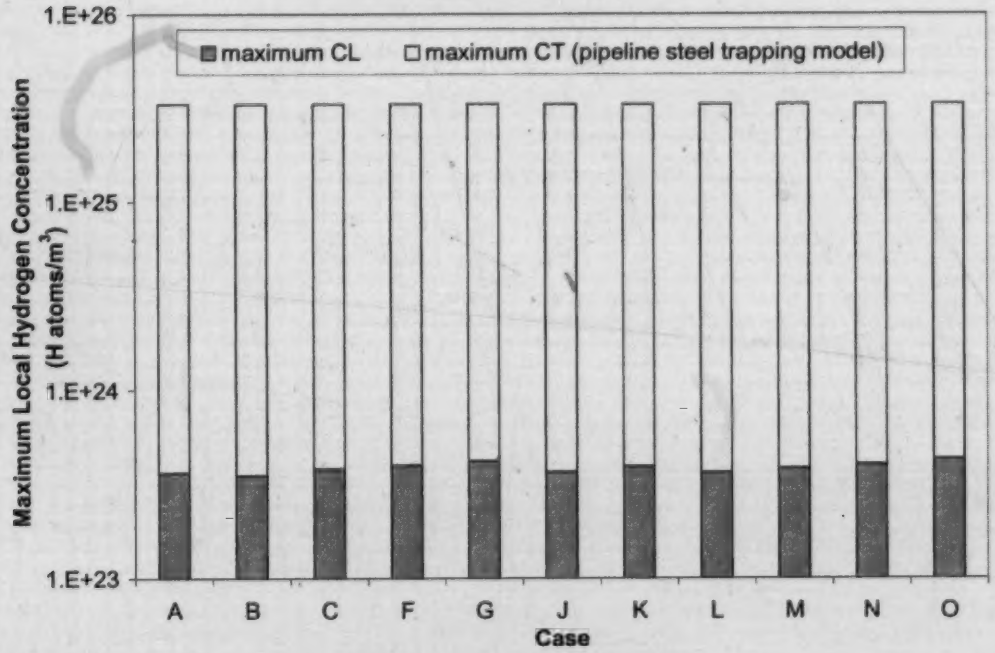

Figure 37 – Contributions of lattice and trapped hydrogen to maximum local concentration, using pipeline steel trap density value

6.4.2. Use of Hydrogen-Dependent HELP Material Property Model

The hypothetical material property model shown in Table 11 and Figure 19 was used to investigate how hydrogen enhanced localized plasticity would affect the local hydrogen concentrations and plastic strain values near a corrosion pit.

In this work, only the trap density model for pure iron was used. These trap densities are thought to apply to the primary ferrite regions in pipeline steels. The trap density model including carbide interface traps, which is thought to be representative of pipeline steel, predicts hydrogen concentrations that are nearly constant throughout the material, so that hydrostatic stress and plastic strain have a negligible effect on the total hydrogen concentration in the steel.

The hydrogen dependent material property model was applied to four different finite element models. These cases were included in the summary of stress and strain results in Table 16. The loading cases before the application of HELP and after the iterative application of the hydrogen-dependent material properties are described in Table 20.

Table 20 – Finite element models using hydrogen dependent material properties

Case with no hydrogen dependence		Corresponding case with hydrogen dependence	
B	97%, uniaxial, hemisphere, no H dep.	D	97%, uniaxial, hemisphere, with H dep.
C	97%, biaxial, hemisphere, no H dep.	E	97%, biaxial, hemisphere, with H dep.
F	97%, uniaxial, hemisphere, base dissolution, no H dep.	H	97%, uniaxial, hemisphere, base dissolution, with H dep.
G	97%, biaxial, hemisphere, base dissolution, no H dep.	I	97%, biaxial, hemisphere, base dissolution, with H dep.

Table 21 – Hydrogen concentrations in models with HELP effects

Case	Brief description	Maximum (and Bulk) C_L^σ (H atoms/m^3)	Maximum (and Bulk) C_T, using N_T for pure iron (H atoms/m^3)
B	97%, uniaxial, hemisphere, no H dep.	3.55×10^{23} (3.29×10^{23})	9.76×10^{20} (8.51×10^{20})
C	97%, biaxial, hemisphere, no H dep.	3.85×10^{23} (3.45×10^{23})	9.68×10^{20} (8.51×10^{20})
D	97%, uniaxial, hemisphere, $\downarrow\sigma_y$ with $\uparrow$[H]	3.55×10^{23} (3.29×10^{23})	9.76×10^{20} (8.51×10^{20})
E	97%, biaxial, hemisphere, $\downarrow\sigma_y$ with $\uparrow$[H]	3.81×10^{23} (3.45×10^{23})	9.82×10^{20} (8.51×10^{20})
F	97%, uniaxial, hemisphere, base dissolution, no H dep.	4.02×10^{23} (3.29×10^{23})	1.37×10^{21} (8.51×10^{20})
G	97%, biaxial, hemisphere, base dissolution, no H dep.	4.22×10^{23} (3.45×10^{23})	1.34×10^{21} (8.51×10^{20})
H	97%, uniaxial, hemisphere, base dissolution, $\downarrow\sigma_y$ with $\uparrow$[H]	4.10×10^{23} (3.29×10^{23})	1.49×10^{21} (8.51×10^{20})
I	97%, biaxial, hemisphere, base dissolution, $\downarrow\sigma_y$ with $\uparrow$[H]	4.09×10^{23} (3.45×10^{23})	1.53×10^{21} (8.51×10^{20})

The changes in the stresses resulting from the use of a hydrogen-dependent material property model are illustrated in Figure 38, which compares the maximum von Mises and hydrostatic stresses in the biaxially and uniaxially loaded models with and without HELP effects.

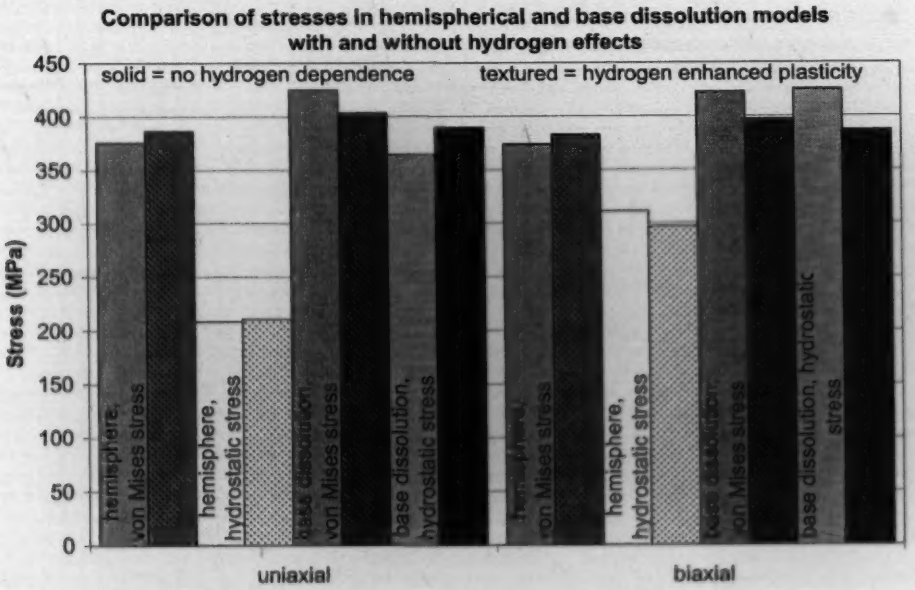

Figure 38 – Comparison of maximum stresses in hemispherical and base dissolution models, with and without hydrogen dependent material property model

The changes in the equivalent total strains resulting from the use of a hydrogen-dependent material property model are illustrated in Figure 39, which compares the strains in the biaxially and uniaxially loaded models with and without HELP effects. In the hemispherical models, the HELP effects increase the maximum strain only minimally: the maximum strain is unchanged at 0.47% in the uniaxial case and increases from 0.44% to 0.49% in the biaxial case. The models of a hemisphere with base dissolution exhibit a larger increase in strain as a result of hydrogen enhanced localized plasticity. The maximum strain in the uniaxially loaded model is 1.68% without HELP and 2.01% with HELP (a 20% increase). The maximum strain in the biaxially loaded model increases by 30%, from 1.61% to 2.10% with the introduction of the HELP material model.

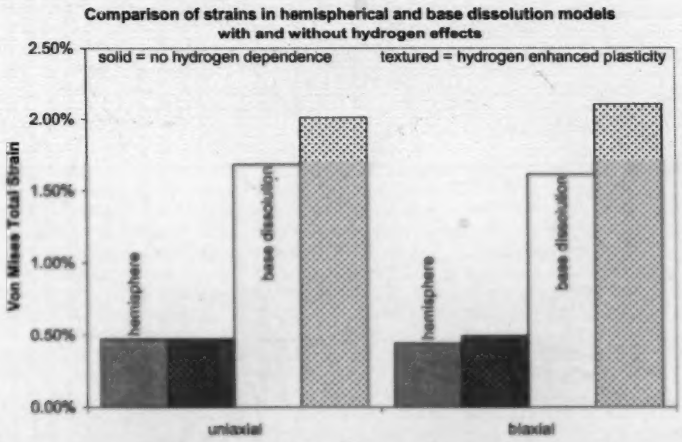

Figure 39 – Comparison of maximum strains in hemispherical and base dissolution models, with and without hydrogen dependent material property model

The influence of the HELP model on the magnitude and location of hydrostatic and von Mises stresses for a hemispherical pit with biaxial loading is illustrated in Figure 40 through a series of contour plots created using the finite element analysis software. Images (a) and (b) show the hydrostatic and von Mises stress profiles respectively. Image (c) shows the pseudo-temperatures used to introduce hydrogen concentrations and hydrogen dependent material behaviour to the finite element program.

The hydrogen concentration contours are very similar to those of the hydrostatic stress, since the lattice hydrogen concentration dominates the total hydrogen concentration when trap densities for pure iron are used. Images (d) and (e) show the hydrostatic and von Mises stress profiles after the iterative application of the hydrogen dependent stress-strain properties. The shape of the hydrostatic stress contours has not changed significantly in comparison to image (a), but the magnitude of the maximum hydrostatic stress has decreased from 311 MPa to 297 MPa. The shape of the von Mises stress contours has changed dramatically, and the maximum von Mises stress is now at a new location in the pit. The base of the pit, where the highest hydrogen concentrations existed, has experienced softening, with increased strains and lowered stresses.

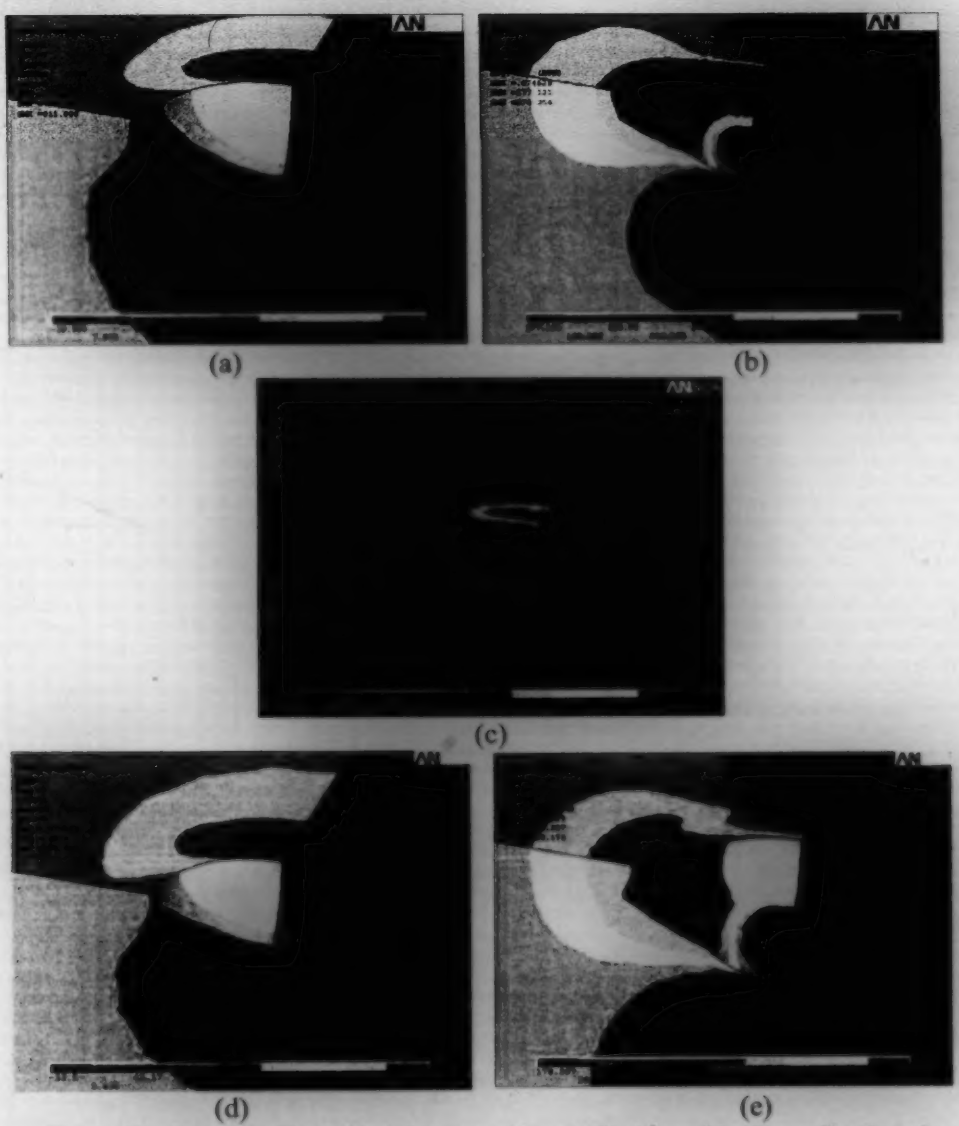

Figure 40 – Stress profiles (a,b) and temperature profile (c) used in the application of a hydrogen-dependent material property model and the resulting stress profiles (d, e)

6.5. Cyclic Loading and Trap Density Effects

Cyclic loading of X-52 may create more hydrogen trap sites by the build up of dislocations. Qualitative modelling work was carried out to investigate the effects on hydrogen concentrations if dislocation trap density is increased by an order of magnitude or more.

This modelling work is only applicable to the trapping model for pure iron, in which carbide trap sites are not present. For the trap density model of the pipeline steel, carbide trap densities greatly exceed dislocation trap densities. Hydrogen trapped at dislocations makes a negligible contribution to total trapped hydrogen in this case. Even an order of magnitude increase in the dislocation trap density would have an insignificant effect on total trap density.

Equation (26) was used to locally increase trap density in areas with the highest plastic strain by either a factor of 10 or 30. The stress and strain results for the 97% SMYS biaxial loading of a hemispherical pit were used to calculate the lattice and trapped hydrogen concentrations for three cases: original trap density, localized multiplication of trap density by a factor of ten and localized multiplication of trap density by a factor of thirty. Comparing the maximum lattice, trapped and total hydrogen concentrations (C_L^{σ}, C_T and $C_L^{\sigma} + C_T$ respectively) values for these cases shows that this trap multiplication has a very small effect on the total hydrogen concentrations, since the trapped hydrogen concentration is several orders of magnitude smaller than the lattice hydrogen concentration.

The maximum total hydrogen concentration is not the sum of the maximum lattice and maximum trapped hydrogen concentrations because these maximums occur at different locations with respect to the hemispherical pit. Figure 41 compares the contours of total hydrogen concentration for the three cases. In each plot, the scale for hydrogen concentration shown on the graph is from 300 to 400, which represents concentrations from 3.43×10^{23} H atoms/m^3 to 4.00×10^{23} H atoms/m^3.

Table 22 – Hydrogen concentrations with trap density multiplication

Multi-plication	Maximum C_L^{σ} (H atoms/m^3)	Maximum C_T (H atoms/m^3)	Maximum $C_L^{\sigma} + C_T$ (H atoms/m^3)	Increase in total hydrogen from original case
None	3.850×10^{23}	9.676×10^{20}	3.857×10^{23}	
10x	3.850×10^{23}	9.676×10^{21}	3.862×10^{23}	0.13 %
30x	3.850×10^{23}	2.903×10^{22}	3.921×10^{23}	1.7 %

(a)

(b)

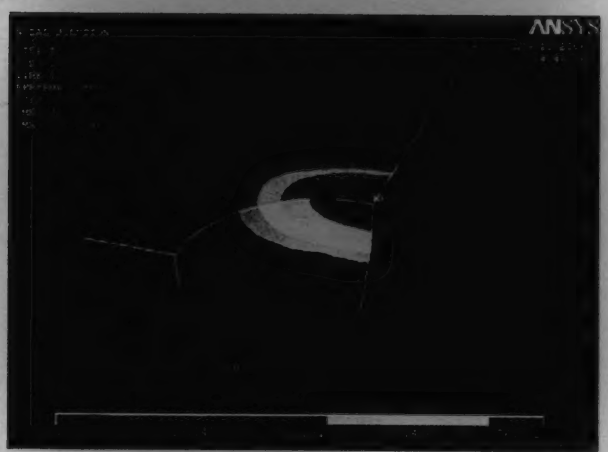

(c)

Figure 41 – Total hydrogen concentrations for (a) original trap density formula (b) maximum trap densities multiplied by ten (c) maximum trap densities multiplied by thirty

7. DISCUSSION

7.1. Constant Load Extension

The creep strains resulting from the constant load tests in air and in C2 solution were summarized and compared graphically in Figure 26. Although the average room temperature creep strain for the tests in C2 is higher than the same average for the tests in air, the scatter in tests results for tests conducted under identical conditions is much larger than the difference in averages between the tests in air and the tests in C2. The large range in results for seemingly identical test conditions indicates that there is a lot of variation in the properties and dislocation structure in this X-52 pipe section over a short distance. The range observed in the results that were obtained suggests that a large number of samples would have to be tested in each condition in order to find a statistically significant conclusion about the difference in room temperature creep occurring in X-52 in air and in a C2 solution.

The purpose of these constant load extension tests was to demonstrate lower yield strength of X-52 due to hydrogen ingress in a near neutral-pH solution. The hypothesized lower yield strength was expected to be evidenced as a higher room temperature creep strain in C2 solution than in air. The test results did not show the predicted trend. However, while the tests did not clearly demonstrate a difference between room temperature creep in air and in C2 solution, the results do not rule out the possibility of such a difference. The range of results between trials is large enough that no conclusions can be made about the effect of hydrogen ingress in near neutral-pH solution on the yield strength and room temperature creep of X-52 steel.

7.2. Hydrogen Content Determination

To see if storing the samples in liquid nitrogen affected their hydrogen content reading, a hydrogen standard sample (5.4 ± 0.4 ppm) was put into liquid nitrogen and then tested using the hot extraction method. It was thought that the liquid nitrogen might affect the test results because the samples are cold enough that

frost forms on their surface in the few seconds that they are taken out of the cup and put into the crucible and into the test machine. The standard sample that was immersed in liquid nitrogen came out with an accurate reading (5.5 ppm), suggesting that cold temperatures and frost do not affect the hydrogen content measurements.

As addressed in Section 5, there were some problems with the results obtained from the hydrogen content determination tests, including abnormally high hydrogen concentration measurements, large scatter on replicate tests and a pattern in which the first sample tested in a set of three tests of identical samples produced a higher reading. The reason for the outlying data points is unknown. However, it is still possible to find value in the results that were obtained by using judgment to omit the results that are problematic. There is a trend for the first hydrogen content measurement in a set of three replicate tests to be unrealistically high. Four of the twenty-two data points were discarded due to this trend. The four discarded points were for tests "C2 1", "C2 4", "C2, no stress 1" and "C2, no stress, previous strain 1". In each case, these first test results were at least 60% higher than the other measurements for the same sample type.

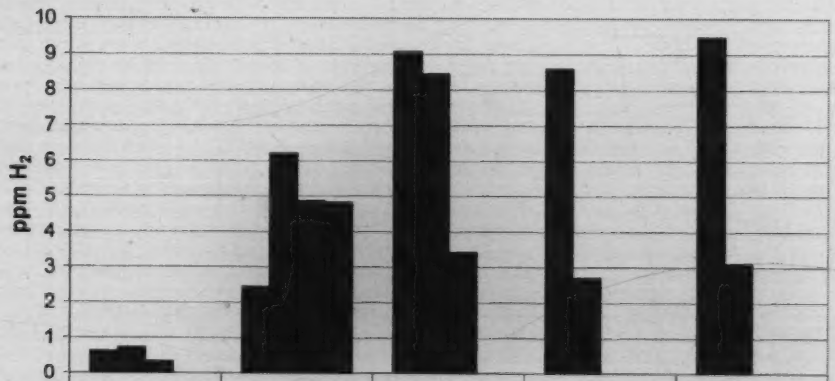

	Air	C2	C2 plus poison	C2, no stress	C2, no stress, previous strain
#1	0.628	2.45	9.08	8.6	9.5
#2	0.736	6.22	8.46	2.7	3.1
#3	0.346	4.87	3.41		
#4		4.83			

Figure 42 – Measured Hydrogen Concentrations in Five Types of Test Samples

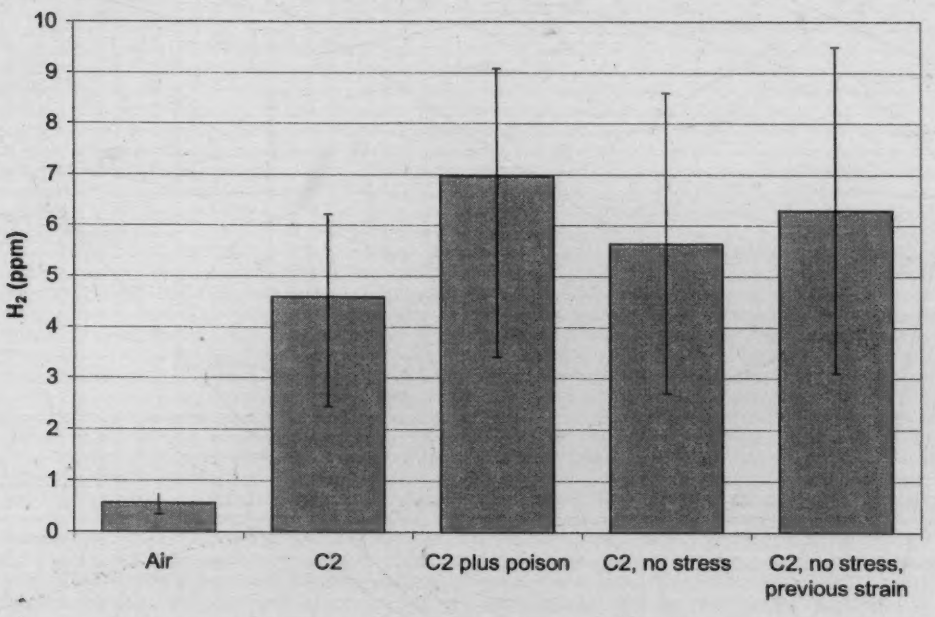

Figure 43 – Average and Range of Measured Hydrogen Concentrations in Five Types of Test Samples

The results of the hydrogen content tests show that the hydrogen content of X-52 steel samples is increased by exposure to C2 solution when compared to the equilibrium hydrogen concentration in air. Figure 42 and Figure 43 compare the hydrogen concentration measurements for fourteen of the eighteen test results that were deemed to be accurate. (The remaining four data points are three samples stored in liquid nitrogen that were allowed to come to room temperature before testing, and one calibration standard sample that was cooled in liquid nitrogen before testing.)

It is very apparent from these graphs that the hydrogen concentration was higher in the samples exposed to C2 solution than in the samples stored in air. The average hydrogen concentration measured in the three tests of samples in air was 0.57 ppm. In comparison, the average hydrogen concentration for the eleven tests of samples in C2 with various other conditions is 5.75 ppm.

Three of the tensile samples tested were put under constant stress while exposed to C2 solution and then stored in liquid nitrogen before testing in the LECO hydrogen determinator. Two of these samples belong to the "C2" test condition category and the third was a "C2 plus poison" sample. A small piece was cut from the gauge length of each of these three tensile samples and these were allowed to come to room temperature before testing. These pieces were tested in the LECO RH-402 to see how the hydrogen content of the sample changed by warming up and being exposed to room conditions for at least twenty minutes. For each tensile specimen, the room temperature sample was found to have lower hydrogen content than the samples that had been stored in liquid nitrogen until testing. The values measured (0.31, 1.24 and 2.01 ppm) for these room temperature samples were still higher than the hydrogen contents for the "air" samples that had never been exposed to C2 solution. Figure 44 shows this comparison. This indicates that some of the hydrogen had left these samples before they were tested, but that the hydrogen concentration in these pieces had not yet reached equilibrium with their new environment – the air in the laboratory.

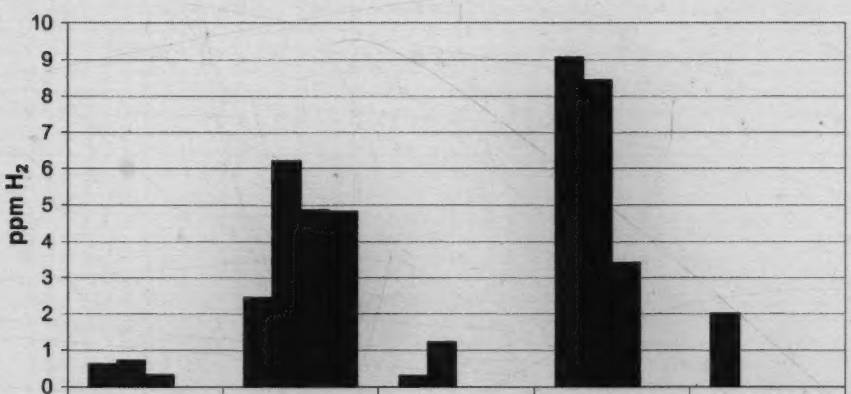

	Air	C2	R.T. C2	C2 plus poison	R.T. C2 plus poison
#1	0.628	2.45	0.31	9.08	2.01
#2	0.736	6.22	1.24	8.46	
#3	0.346	4.87		3.41	
#4		4.83			

Figure 44 – Comparison of Measured Hydrogen Concentrations in Previously Stressed Samples Stored in Liquid Nitrogen or Allowed to Reach Room Temperature

The observation that a large portion of the hydrogen is leaving the samples in air contradicts the present understanding of lattice and trapped hydrogen in pipeline steels. As will be shown in more detail in Section 7.3.3 using Figure 46, hydrogen contained in either dislocation traps or carbide interface traps is not predicted to leave these trap sites at temperatures below 350 K. Only the more mobile lattice hydrogen, which is present in much lower concentrations that trapped hydrogen in pipeline steel, is expected to escape quickly from the steel. Based on the lattice hydrogen concentration values used for the finite element modelling, the loss of all diffusible lattice hydrogen in the samples cannot account for the decrease in measured hydrogen contents when the samples were allowed to reach room temperature. The observation that much of the hydrogen is leaving the samples when they are warmed in air indicates either that the actual proportion of lattice and trapped hydrogen in the steel is different than understood from the finite element modelling or that the trapped hydrogen is behaving differently than presently thought and could be escaping from the carbide interface traps at room temperature.

Upon comparing the measured hydrogen contents for the "C2" and "C2 plus poison" conditions, it appears that the application of both a recombination poison and an imposed cathodic potential was successful in increasing the hydrogen content in the samples. However, due to the large range in the data points, this observation cannot be firmly relied upon. The comparison of hydrogen concentrations in room temperature samples of "C2" and "C2 plus poison" shows the same inclination towards a higher hydrogen concentration in the samples that was exposed to poison and cathodic potential (2.01 ppm vs 1.24 ppm and 0.31 ppm)

Figure 9, showing the unstressed hydrogen concentrations as measured in a number of conditions by other workers, is repeated here as Figure 45 with the results of the present tests added for comparison purposes.

The hydrogen concentrations measured are within the same range as those measured by He, Vadhwana and Qiao, Luo and Mao. The maximum hydrogen content determined in the present work (9.5 ppm) is higher than the highest concentration reported by any of the workers cited (7.78 ppm). This concentration, reported by Vadhwana, was achieved on the charging side of an X-65 coupon in a 0.1 N H_2SO_4 solution poisoned with 10 ppm As_2O_3, being charged at 1 mA/cm^2. However, when it is considered that the literature values being used for comparison do not include trapped hydrogen concentrations while the LECO test results include trapped hydrogen concentrations and that range of reported values is nearly three orders of magnitude, then the maximum value in the present results that is roughly 18% higher than other cited values does not indicate that the present results are inaccurate.

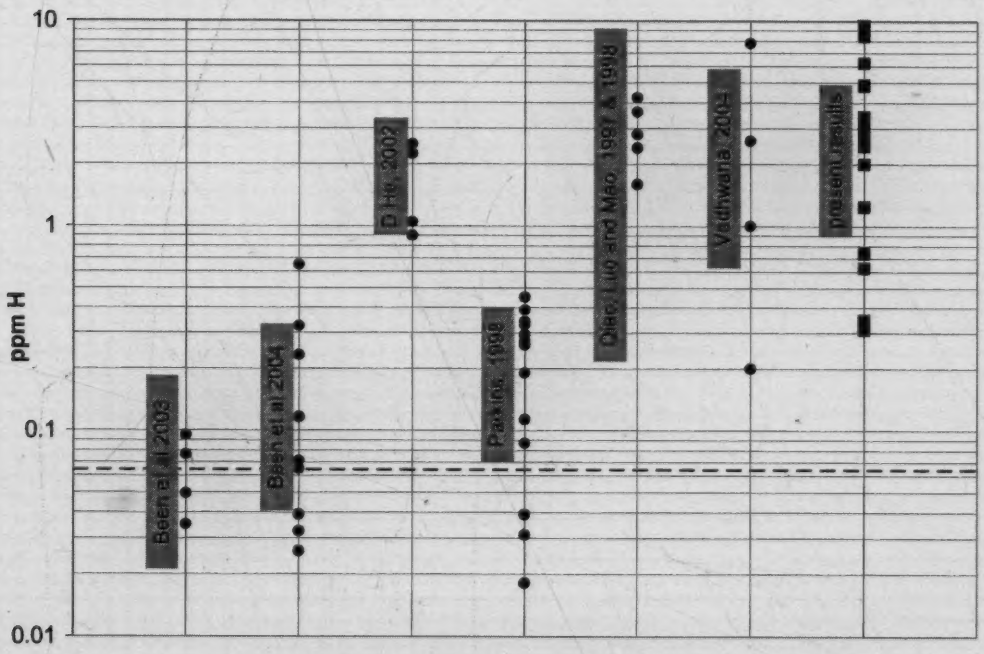

Figure 45 – Comparison of unstressed hydrogen concentrations reported in the literature to the present hydrogen determination results

The dashed horizontal line in Figure 45 shows the C_L^o value that was used in the finite element model. As discussed previously, the difference between the initial concentration used in the finite element model ,which represents only lattice

hydrogen concentration, and the higher hydrogen concentrations measured in the present work and other work is not problematic in interpreting the results of the model. The hydrogen concentrations measured in the present work include trapped hydrogen while C_L^o does not.

7.3. Finite Element Model

Plastic strains reach their maximum values right at the surface of the stressed material. Moving into the material from the surface of the stress raiser, the plastic strain decreases towards zero and the hydrostatic stress rises to a peak at some distance below the free surface and then decreases towards the bulk hydrostatic stress value. The magnitude of the hydrostatic stress and plastic strain surrounding a corrosion pit determine the level of local hydrogen enrichment.

7.3.1. Uniaxial vs. Biaxial Loading

Even before calculating the concentrations of lattice and trapped hydrogen that would reside near the pit for the cases of biaxial or uniaxial loading, it is clear that there are some significant differences in stress and strain conditions resulting from the different loading cases. The biaxially loaded model has a significantly lower bulk von Mises stress and higher bulk and maximum hydrostatic stress than does the uniaxially loaded model.

Using the pure iron trapping model, the biaxially loaded bulk material will have less trapped hydrogen than its uniaxial counterpart because of the lower von Mises stress and thus lower plastic strains. The biaxially loaded model will have more interstitial hydrogen than its uniaxial counterpart because it has higher bulk and maximum hydrostatic stresses. Since, when using the pure iron trapping model, the lattice hydrogen concentration dominates the total hydrogen concentration, this latter comparison is the more significant of the two.

The biaxially loaded model of a hemispherical pit will have an equilibrium hydrogen concentration in the bulk material about 5% higher than the same pit with only uniaxial loading.

When the localized stress conditions surrounding the pits are considered, this difference is magnified. In the base of the pit, where the stress and strain conditions make crack initiation most likely, the von Mises stress levels, and hence the trapped hydrogen concentrations are quite close while there is a larger difference in the localized hydrostatic stress at the pit base, which will cause a higher concentration of interstitial, lattice hydrogen. At the location with maximum stress at the base of a pit model, the model with biaxial loading will have a maximum hydrogen concentration about 8% higher than the same geometry under uniaxial loading.

This comparison is explained for the smooth hemispherical pit for convenience. The same comments hold true for the other four geometries that were modeled.

When the trap densities for pipeline steel are applied, the differences in stress and strain between the uniaxial and biaxial loading cases no longer translate to differences in the total hydrogen concentrations. The hydrogen trapped at carbide interfaces dominates the total hydrogen concentration and this quantity is not dependent upon stress and strain conditions. However, it is understood that the hydrogen concentration in the primary ferrite regions will still be increased as seen in the model using trap densities representative of pure iron.

While the quantitative effects of hydrogen on material properties of line pipe steel are still unknown, the two assumptions that (1) hydrogen plays a critical role in the initiation of near-neutral pH stress corrosion cracks, and (2) the total hydrogen concentration (rather than either just the lattice or trapped hydrogen) controls the changes in material properties, leads to the conclusion that: (a) if lattice hydrogen concentrations exceed trapped hydrogen, then a biaxially loaded pipe will have a higher susceptibility to NNpHSCC than a pipe with zero or low levels of axial stress and (b) if hydrogen at carbide interfaces exceeds that at dislocation traps

and in lattice sites, then NNpHSCC susceptibility cannot be linked to local hydrogen enrichment at stress and strain concentrations.

If the hydrogen concentrations in the primary ferrite regions and pearlite colonies of pipeline steel are treated separately and understood to have significantly different values, then hydrostatic stress and plastic strain may be important in the local hydrogen enrichment of the ferrite regions.

7.3.2. Sensitivity to Pit Geometry

Five types of three-dimensional pit geometries were modeled using finite element analysis. Figure 30 in Section 6.3.1 graphically compared the maximum von Mises and hydrostatic stresses under both uniaxial and biaxial loading for the five pit geometries.

For all five geometries, the maximum von Mises stress obtained was just slightly higher for the uniaxial loading case than for biaxial loading. The differences ranged from 0.4% (for the smooth hemispherical pit) to 6% (for the hemisphere with cylindrical dissolution) higher von Mises stresses in the uniaxial case.

The maximum hydrostatic stress in the models was higher under biaxial loading than with uniaxial loading. This applies to all of the geometries that were modeled. The differences ranged from 16% (for the hemisphere with base dissolution) to 49% (for the smooth hemispherical pit) higher hydrostatic stresses in the biaxial case.

The geometries that were modeled can be ranked in order of increasing severity (increasing stress and strain concentrations) as hemisphere, frustum, hemi-ellipsoid, hemisphere with base dissolution and then hemisphere with cylindrical dissolution. This trend can be linked to the minimum radius of curvature in the pits. The hemispherical pit has the smoothest geometrical profile modeled, and has the lowest stress concentrations of the five geometries modeled. The small

radius of curvature in the area of cylindrical pit base dissolution produces the highest stress concentrations of the four geometry cases. The frustum is an interesting case when linking radius of curvature in a pit to stress intensification. The transition from the conical walls to the flat base of this pit has a smaller radius of curvature than that of the pit base dissolution, but the location of this radius of curvature is also important: the curve in the frustum does not occur at the center of the pit and thus does not have the same impact on stress levels. Figure 29 shows the hydrostatic stress profiles under biaxial loading for the five geometries modeled, and the differences in the geometry and stress results discussed here can be seen in these stress contour plots.

The comparison of stress and strain results from a two-dimensional and a three-dimensional model of a hemispherical corrosion pit, in Table 18, shows the effect of the lower degree of constraint in the two-dimensional model. The hydrostatic stress values for the two models are similar, with the 3D model holding a higher stress (217. 6 MPa versus 209.5 MPa). The differences in the maximum values of von Mises stress and total strain are much more striking. The two dimensional model calculates a 33% higher value for the maximum von Mises stress (503.8 MPa versus 379.5 MPa) and a maximum strain value that is nearly eight times higher (0.0416 versus 0.0054) than the corresponding results from the three dimensional model.

This difference between the two dimensional and three dimensional model results shows that 3D modelling is necessary for investigating stress and strain values and hydrogen concentrations near pipeline surface flaws such as corrosion pits.

A series of small two dimensional surface notches were modeled with uniaxial tensile loads to find relationships between notch geometry and stress concentrations at the notch tip. Variations were made in the depth, tip radius and wall angle of the notches, as was illustrated in Figure 14.

It was found that a notch with vertical walls and one with angled walls that had the same depth and tip radius would produce essentially identical stress and strain results. Between the 0° and 15° wall angles that were modeled, it can be stated that the wall angle of a notch does not affect the stress conditions around the notch.

The maximum hydrostatic stress, von Mises stress and equivalent plastic strain at the notch tip all increase as the depth of a notch is increased independent of its other dimensions. These trends were expected, but the ease with which the results could be fit to a numerical relation was not anticipated. With results for six different notch depths, trend lines were fit to the data with an excellent fit. The relationships between von Mises or hydrostatic stress and notch depth are best suited to a quadratic relation, while the relationship between plastic strain and notch depth is linear.

For the models that varied the notch tip radius, it was found that as the notch tip becomes sharper (has a smaller radius), the maximum stresses and strains near the notch tip increase. The maximum hydrostatic stress, von Mises stress and equivalent plastic strain can each be fit to quadratic relations as a function of notch tip radius.

It was shown that the results of two dimensional models are much different than similar three dimensional models. It follows that the trends in stress and strain as a function of notch depth and tip radius in two dimensions cannot be transferred to three dimensional problems. However, the good fit of the two dimensional models to simple numerical relations indicates that such trends likely exist for three dimensional surface flaws. To improve our understanding of the effect of corrosion pit geometry on the local stress and strain conditions on the surface of a pressurized pipe, it would be worthwhile to carry out similar modelling in three dimensions, using axisymmetric pits with a variety of depths and radii. Due to the significantly higher computational demands of three dimensional finite element

work, this would be a more demanding initiative than the two dimensional notch modelling carried out in the present work.

7.3.3. Hydrogen Concentrations in Model

The lattice and trapped hydrogen concentrations in the bulk of the material included in the finite element models are not dependent upon the geometry of the pit being modeled. For the given initial hydrogen concentration, $C_L^o = 3.0 \times 10^{23}$ H atoms/m^3, the bulk hydrogen concentration was found to depend only upon the applied loading to the model. Uniaxially loaded models have a bulk C_L^σ value of 3.29×10^{23} H atoms/m^3 while biaxially loaded models have a bulk C_L^σ value of 3.45×10^{23} H atoms/m^3. These values are 9.7% and 15% higher respectively than the initial unstressed hydrogen concentration. The bulk of the material has no plastic strain. Using the trap density model for pure iron, the bulk C_T value is 8.51×10^{20} H atoms/m^3. If the trap density model for pipeline steel is used, the bulk C_T value is 3.3×10^{25} H atoms/m^3 (110 times greater than C_L^o).

The maximum C_L^σ value at the base of a three dimensional pit model is dependent upon hydrostatic stress, and thus depends upon pit geometry as well as loading conditions. The higher hydrostatic stresses obtained from biaxial loading of models with hemiellipsoid pits or hemispherical pits with base dissolution create higher lattice hydrogen concentrations for these models. For example, the pit with base dissolution has a maximum lattice hydrogen concentration of 4.22×10^{23} H atoms/m^3 when under biaxial load; this is a 40% increase in lattice hydrogen when compared to the unstressed value, C_L^o. This can be compared to the smooth hemispherical pit model. When it is loaded biaxially, the maximum C_L^σ value is 3.85×10^{23} H atoms/m^3, a 28% increase in lattice hydrogen when compared to the unstressed value, C_L^o.

Trapping can play an important role in hydrogen assisted cracking. Trapped hydrogen can contribute significantly to NNpHSCC susceptibility if the system is at temperatures high enough that lattice diffusion is assisted but still low enough

that substantial hydrogen will exist in trap sites. By Equation (19), when the system temperature increases, C_L decreases, and then by Equations (24) and (25), C_T decreases as well. In the temperature range of interest for NNpHSCC (roughly 280 K to 310 K), hydrogen can diffuse sufficiently well through the steel, while saturating the available trap sites. Figure 46 shows that the trap sites will be saturated in the temperature range of interest. Using a fractional lattice occupancy value of 6.78×10^{-7}, a representative value taken from the finite element model results, the fractional trap occupancy was calculated at a range of temperature for both of the binding energies of interest: -60 kJ/mol for dislocation traps and -84 kJ/mol for iron carbide interface traps.

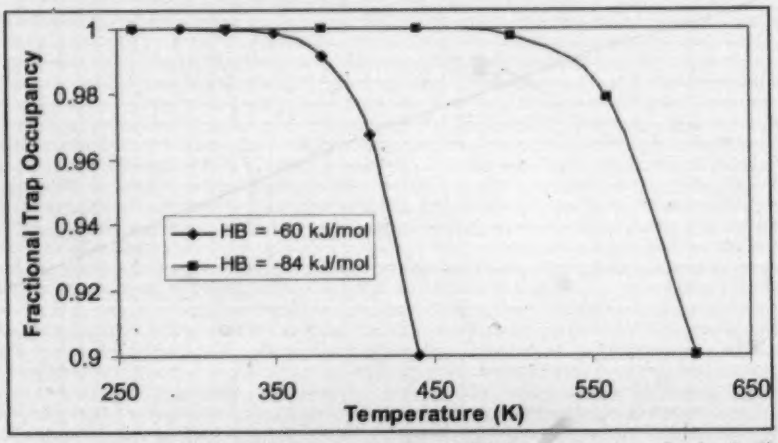

Figure 46 – Decrease in fractional trap occupancy at high temperature for both dislocation traps and carbide interface traps

Using the trap density model for pure iron, the maximum C_T value is dependent upon plastic strain, and thus upon pit geometry. In contrast, if the trap density model for pipeline steel is used, the C_T value is the same everywhere in the material, and does not depend upon geometry or loading conditions. Hydrogen trapping in pipeline steels is understood to exist primarily at carbide interfaces in the microstructure. Therefore, the trapped hydrogen concentration in the primary ferrite regions can be expected to depend upon plastic strain even though the total trapped hydrogen concentration in the steel will be independent of hydrostatic stress and plastic strain.

The C_T values resulting from the pure iron trap densities are much lower than the C_L^{σ} values for the same pit model. In these cases, as illustrated by Figure 36, the lattice hydrogen concentration dominates the total hydrogen concentration.

When N_T values representative of pipeline steels are used in the hydrogen concentration calculations, the trapped hydrogen concentration exceeds the lattice hydrogen and dominates the total hydrogen concentration as shown in Figure 37.

Figure 47 shows this difference in the relative magnitudes of C_L^{σ} and C_T between the two trapping models by showing how C_L^{σ} remains constant and C_T increases linearly when N_T is increased. Vertical dashed lines on this graph mark the typical trap densities of the two trapping models used in the hydrogen concentration calculations.

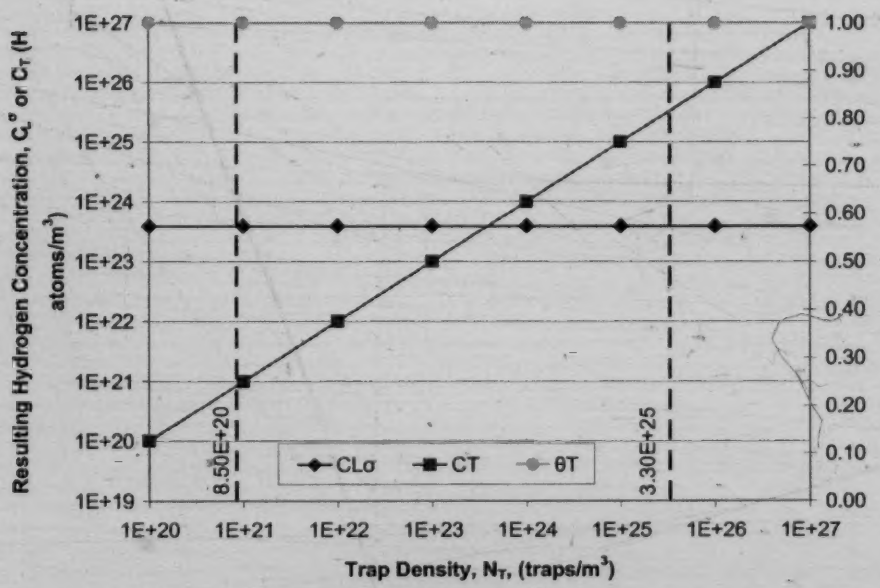

Figure 47 – Maximum lattice and trapped hydrogen concentrations as a function of trap density

The hemispherical and base dissolution pit models were used to investigate the effects of a hypothetical system of hydrogen dependent material properties on the stress, strain and hydrogen concentrations in these models. This work only applies

to the pure iron trap density model, in which there is a significant enrichment in hydrogen around the corrosion pits being modeled.

The changes in hydrostatic stress and von Mises stress due to the HELP model were not consistent across the different geometries and loading conditions used. Figure 38 graphically compares the maximum stresses in the models both with and without the use of the hydrogen dependent material properties and Figure 39 does the same for maximum strain. Table 23 summarizes these changes. An arrow indicates whether the stress in question increased or decreased with the application of the HELP material property model. The number in parentheses gives the change in stress from the model without hydrogen concentration dependence to the model with this dependence.

Table 23 – Changes in maximum stresses and strains due to the use of hypothetical hydrogen-dependent material properties

	Von Mises Stress		Hydrostatic Stress		Total Strain	
	Uniaxial Loading	Biaxial Loading	Uniaxial Loading	Biaxial Loading	Uniaxial Loading	Biaxial Loading
Hemisphere	↑ (2.9%)	↑ (2.4%)	↑ (1.1%)	↓ (4.7%)	→ (0%)	↑ (11%)
Base Dissolution	↓ (5.0%)	↓ (6.1%)	↑ (6.9%)	↓ (8.9%)	↑ (20%)	↑ (30%)

For the hemispherical pit that was modeled with uniaxial loading, the hydrostatic stress without hydrogen dependence is fairly equally distributed along the plane of pit symmetry in the y-direction. The hydrostatic stress contour plot for this case is shown in Figure 48. The hydrogen content is enriched all along this line, instead of at the pit base. Similarly, the von Mises stress, which is the driving force for plastic deformation, shows even contours along the plane normal to the direction uniaxial loading. When the area with hydrogen enrichment is effectively softened by the use of hydrogen dependent material properties, this entire band experiences more general deformation and higher stresses, and the surrounding material is under less stress as a result.

Figure 48 – Hydrostatic stress contour plot for hemispherical pit under uniaxial loading with no hydrogen dependence of stress-strain behaviour

The stress and hydrogen concentration plots for biaxial loading of the hemispherical pit were shown in Figure 40. In this case, the hydrogen enrichment is localized at the pit base, while the area with the highest von Mises stresses extends further along the surface near the pit. The hydrogen enhanced plasticity acts to soften the material at the pit base, lowering both the von Mises and hydrostatic stresses in this area, while transferring the load towards the surface edge of the pit, and increasing the von Mises stress in this region.

Before application of the hydrogen dependent material properties, the hemispherical pit with base dissolution has very localized high stresses in the region of base dissolution under both uniaxial and biaxial loading. The hydrogen concentration is highest right below the surface of the area of dissolution. The introduction of a HELP phenomenon to the model weakens this locally hydrogen enriched area. When this area is softened, it reduces the effect of the base dissolution on the overall stress conditions of the pit and causes it to behave more like a smooth hemispherical pit. The base undergoes additional strain, but is unable to carry as much of the load, and this load is transferred to the rest of the pit. The hemispherical pit model with base dissolution underwent greater changes in stress and strain with the application of the HELP model than the similar hemispherical model.

In both the uniaxial and biaxial loading cases, with the introduction of the hydrogen dependent material properties, the von Mises stress spreads out towards the surface of the pit, and the peak stress is decreased because the load is being carried over a larger area. As this hydrogen induced softening occurs, the uniaxially loaded model experiences an increase in hydrostatic stress, while the biaxially loaded model undergoes a decrease in maximum hydrostatic stress.

Critical surface strain is thought to be responsible for crack initiation by HELP. The large increase in strains at the base of the more severe pit is an indication that the present understanding of the HELP mechanism may explain how local hydrogen enrichment can lead to crack initiation at stress concentrations. The difference in the effect of the HELP model on the two geometries investigated suggests that a fairly severe pit geometry is needed in order for HELP to have a significant effect on the surrounding stress and strain conditions.

7.3.4. Cyclic Loading and Trap Density Effects

In laboratory experiments, cyclic stressing of test samples is often required to create initiation and growth of near-neutral pH stress corrosion cracks. Cyclic loading can cause the build-up of dislocations in material. To investigate how an increase in dislocation density could affect the concentration and location of hydrogen in a model of a hemispherical pit under biaxial loading, the number of traps in the model were multiplied on a graduated scale, using Equation (26), by a factor of either 10 or 30.

Table 22 and Figure 41 give the results of models with trap multiplication. Multiplying the number of traps by a factor of ten in the areas with the highest plastic strain resulted in an increase of only 0.13% in the maximum total hydrogen concentration. Increasing the multiplication factor to thirty resulted in the maximum hydrogen concentration reaching a level 1.7% more than in the original case. The trap multiplication was shown to have a very small effect on

the total hydrogen concentrations. Referring to Figure 36, which shows the relative contributions of lattice and trapped hydrogen graphically when using the pure iron trap density model, it can be seen what a small contribution is made by trapped hydrogen. The trapped hydrogen concentration is more than two orders of magnitude smaller than the lattice hydrogen concentration.

Another contributing factor to the very small effect of trap density multiplication on the hydrogen concentrations is that the lattice and trapped hydrogen reach their peak values at different locations with respect to the geometry of the pit. Using the example with multiplication of the traps by ten, if the maximum trap density and the maximum hydrostatic stress occurred at the same location so that $C_L{}^{\sigma}{}_{max}$ and $C_{T,max}$ could simply be added, the trap multiplication would create a 2.3% increase in maximum total hydrogen concentration. The actual increase is only 0.13% because of the different shapes of the trapped and lattice hydrogen concentration profiles.

7.3.5. Application of Model to Actual Pits

The finite element modelling process that was used in this work to quantify the hydrogen concentrations surrounding hypothetical pits can also be used with actual pits, provided that the three dimensional geometry is known. Such modelling could provide valuable information about the critical local hydrogen concentration associated with NNpHSCC crack initiation.

An example of NNpHSCC initiation from a corrosion pit is shown in Figure 49. The images and information related to this pit are provided by Bingyan Fang and are part of an ongoing study. (Fang 2006) This corrosion pit grew on the side face of a tensile specimen that was exposed to C2 solution and cyclically stressed with σ_{max} = 100% SMYS and R = 0.8. Near the base of the pit, a smaller, crack-like pit was formed and then a sharp crack initiated from the tip of this smaller pit.

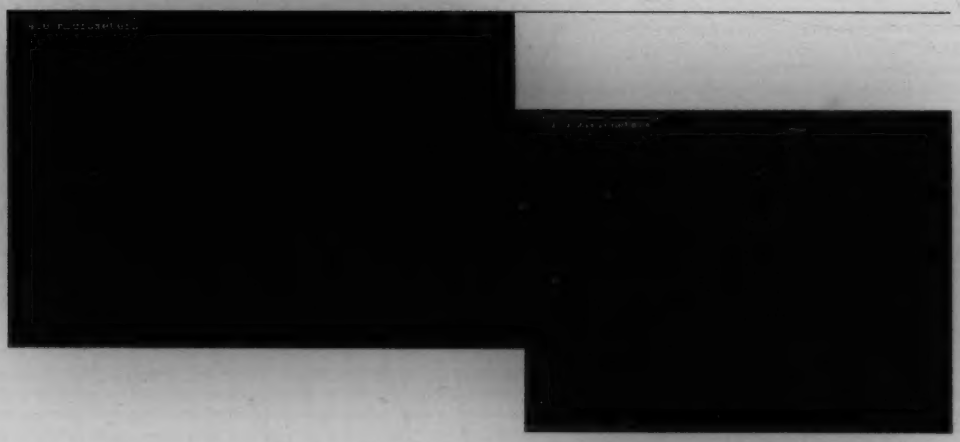

Figure 49– Pit-to crack transition on X-52 tensile sample in near-neutral solution

An attempt was made to create a finite element model of this pit, so that the hydrogen concentration at the tip of the small pit could be estimated. However, the only available information about the geometry of this pit is the micrographs shown in Figure 49 which enables the creation of only a two-dimensional model. Figure 50 shows the points that were used to create the model geometry based on the image in Figure 49. As was shown in Section 7.3.1, the results of two- and three-dimensional models of a uniaxially loaded tensile sample with a corrosion pit are very different. A two-dimensional model treats the pit as if it were a surface groove rather than a surface flaw of a finite size. It is due to this effect that the pit pictured above could not be modeled carrying a load of 100% SMYS using finite element analysis. With a tensile load of only 60% SMYS applied to the sample, the two-dimensional model of this actual pit predicts local ductile failure at the tip of the pit. Under this loading condition, the maximum von Mises stress and total strain are 635 MPa and 14% respectively, as shown in Figure 51 and Figure 52.

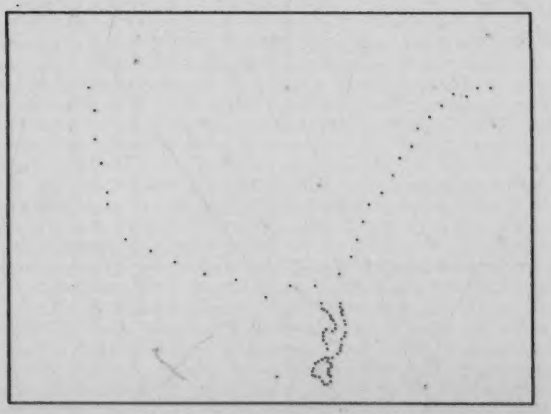

Figure 50 – Points used in the creation of a two-dimensional finite element model of actual corrosion pit

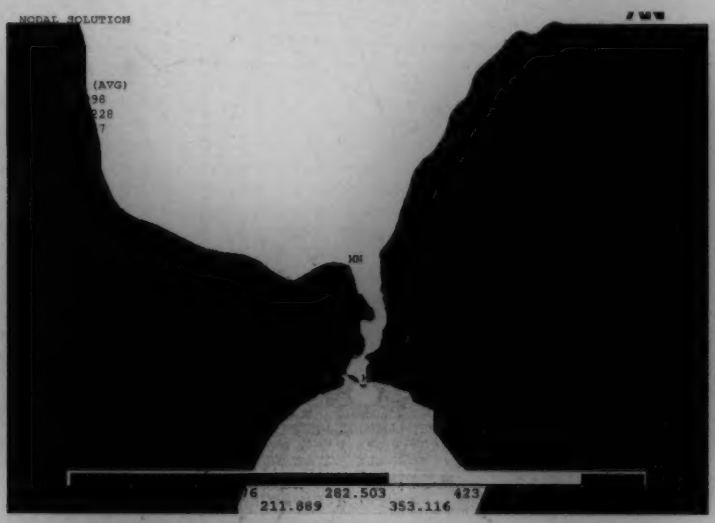

Figure 51 – Von Mises stress contour plot for two-dimensional model of actual pit, with tensile load of 60% SMYS

Figure 52 – Total strain contour plot for two-dimensional model of actual pit, with tensile load of 60% SMYS

In reality, since the pit is actually three-dimensional and not a surface groove, the von Mises stress and strain at the tip of the crack-like pit will be much less than that shown in the above plots and the hydrostatic stress will be higher than that predicted by this model.

An idealized three-dimensional geometry similar to this pit was modeled and is discussed in Sections 6.3.1 and 7.3.2. This geometry is referred to as a hemisphere with cylindrical base dissolution. This work shows that a cylindrical volume of strain assisted dissolution at the base of a hemispherical corrosion pit acts to significantly increase the maximum stress and strain surrounding the pit. Of the five three-dimensional pit geometries modeled, this was the most severe in terms of stress and strain concentrations around the pit.

The pit with sharp base dissolution from the experimental work of Bingyan Fang led to sharp cracking. The path of the crack was mainly through primary ferrite regions. Under uniaxial loading at 97% SMYS, the similar three-dimensional finite element model with cylindrical dissolution at its base was calculated to have a maximum lattice hydrogen concentration of 4.3×10^{23} H atoms/m^3 (0.093 ppm),

a maximum trapped hydrogen concentration of 1.43×10^{20} H atoms/m^3 (3.08×10^{-5} ppm) in dislocation traps and a trapped hydrogen concentration of 3.3×10^{25} H atoms/m^3 (7.11 ppm) including carbide interface traps. The hydrogen surrounding the pit at the time of cracking may constitute a critical hydrogen concentration for crack initiation. The hydrogen concentration values calculated using the finite element model provide an idea of the magnitude of this critical hydrogen concentration. As the cracking was observed to proceed through primary ferrite regions, the trapped hydrogen concentration at carbide interfaces is thought to be unrelated to the critical hydrogen concentration that may exist for crack initiation.

The hydrogen-enhanced localized plasticity (HELP) model states that local hydrogen enrichment causes increased plasticity that can lead to crack initiation at a critical strain. The hypothetical quantitative model for HELP that was applied to two of the three-dimensional geometries caused increases in strain by up to 30% of the initial strain value. Although this HELP model is hypothetical and overly severe (based on the present estimates of lattice and trapped hydrogen values), the type of changes it created in the stress and strain results surrounding the pits provides support for HELP as a crack initiation mechanism. If hydrogen enrichment does create local increases in material plasticity, this local softening may be sufficient for crack initiation at a critical surface strain at the base of corrosion pits.

The loss of a significant amount of hydrogen during the hydrogen content determination tests at room temperature compared to those stored in liquid nitrogen (Section 7.2) suggests that a larger proportion of the hydrogen in the steel may be diffusible lattice hydrogen than predicted by the present model. In this case, stressed pipeline steel in near-neutral pH solution may experience lattice hydrogen enrichment by as much as 100 times instead of the 30% enrichment calculated in the present finite element work. For example, as discussed in Section 7.2, an average hydrogen concentration of 4.6 ppm was measured for

samples stressed in C2 solution while this average value decreased to 0.78 when the samples sat in air for 20 minutes. If all of this lost hydrogen is in fact diffusible lattice hydrogen, this could be important to improving the understanding of HELP as an initiation mechanism by showing that near-neutral solution can increase lattice hydrogen concentrations several times over.

In the future, three-dimensional geometrical information should be collected about corrosion pits that did and did not serve as crack initiation sites. These pit geometries could be modeled with the appropriate applied stresses in hopes of identifying a critical local hydrogen concentration associated with NNpHSCC initiation.

The reliability of this modelling work, as is the case with any present models of hydrogen in pipeline steels, depends on our understanding of the density and behaviour of hydrogen traps in this material. Before valuable information can be gained from the modelling of actual pit-to-crack transitions, we must first improve upon our hydrogen trapping models.

7.4. Implications for Crack Initiation

The hydrogen content determination tests carried out using the LECO RH-402 showed that the hydrogen concentration increases when X-52 samples are exposed to C2 solution with a CO_2 blend purging gas. The constant load extension tests failed to show a large increase in plasticity for X-52 samples held at constant load as they were exposed to C2 solution so that hydrogen ingress would occur. Together, these two findings suggest that the elevated hydrogen concentration in X-52 steel when exposed to a near-neutral pH solution does not lead to significant hydrogen enhanced plasticity. Cyclic loading tests carried out by other researchers have shown that pipeline steels are more susceptible to cracking when exposed to near-neutral pH environments. Although the elevated hydrogen concentration in the present tests did not result in increased bulk strain under

constant load, the hydrogen must still contribute to the cracking process, possibly by changing or accelerating the fatigue process.

The hypothetical hydrogen-dependent stress-strain model used to study the effects of HELP on stressed corrosion pits was quite severe. It required that the yield strength of the steel would decrease by half when the hydrogen concentration was increased by roughly 30%. With this severe softening effect, the increases in strain in the modeled hemispherical pits are quite limited, while the sharper geometry of the pit with base dissolution allowed for a larger effect of the HELP model on the maximum strains as shown in Figure 39. The results of the hydrogen content determination tests and the constant load extension tests indicate that the HELP model used in the finite element work was much more severe than is realistic, and yet crack initiation can not even be predicted with this model. These findings suggest that very sharp pit geometry, such as that in Figure 49 must be created by corrosion fatigue or strain directed dissolution before HELP effects can be expected to result in sharp crack initiation.

One of the key determining factors in predicting the concentration and location of hydrogen in pipeline steels is the hydrogen trapping. The two trapping models used throughout the finite element modelling produce very different hydrogen concentration results.

By the trapping model derived from permeation tests on pure iron, the hydrogen concentration will be dominated by lattice hydrogen and will be at a maximum at the location with peak hydrostatic stress. For biaxial loading, this location is the pit base. This seems to support the concept that NNpHSCC will be more likely to initiate in areas with elevated hydrogen concentrations. However, these trap densities are thought to be unrealistically low for an X-52 steel.

In contrast, the trap densities measured for X-52 steel in NS4 solution are several orders of magnitude higher. These traps are understood to be at the interfaces

between ferrite and cementite phases in the steel. The trap densities are not dependent on plastic strain, and will not be higher near the base of corrosion pits where stress concentrations can cause plastic strain. Modelling with these trap densities finds a total hydrogen concentration that is dominated by trapped hydrogen. The concentration profile is essentially even, with negligible hydrogen enrichment near surface flaws on the surface of a pressurized pipe. The differences in hydrogen concentration do not exist over lengths of several hundred microns, but are instead present within the microstructure on a much shorter scale. Ferrite regions in the steel will have hydrogen concentrations nearly equivalent to those measured in pure iron. The hydrogen concentration in these regions is still expected to be dependent upon hydrostatic stress and plastic strain in the material, but will be much lower than the hydrogen concentration at the cementite interfaces. The Fe_3C interfaces will have at least two orders of magnitude more hydrogen than the nearby ferrite.

Figure 53 – Surface of an X-52 sample, previously polished as for metallography without etching, then exposed to NS4 solution with pH = 6.3 for 3 days, x1000 [Source: Parkins and Beavers 2003]

A micrograph of an X-52 microstructure is shown in Figure 53. It shows ferrite grains and lamellar pearlite regions. This particular image contains a higher ratio of pearlite to primary ferrite than is typical of this steel. A near-neutral pH stress corrosion crack propagating through a ferrite-pearlite microstructure such as this will pass through ferrite as well as pearlite. The ferrite grains do not have nearly

as much hydrogen as is present in the pearlite and yet the cracks do not show a markedly different cracking character.

This disagreement between the locations of high hydrogen concentration in the X-52 microstructure and the experimentally observed cracking behaviour suggests that cracking propensity in pipeline steels cannot be directly linked to total hydrogen concentration and that hydrogen may play different roles in the stress corrosion cracking of pearlite and primary ferrite regions.

8. CONCLUSIONS

8.1. Main Conclusions

The present research studied the role of hydrogen in the initiation of near-neutral pH stress corrosion cracks. It is widely accepted that hydrogen and dissolution are the key factors in the NNpHSCC mechanism. Hydrogen content determination tests were carried out to measure the concentration of hydrogen in samples of X-52 steel in various conditions. Constant load extension tests in air and in C2 solution were compared to investigate the effect of elevated hydrogen concentrations on the room temperature creep behaviour of X-52 pipeline steel. Extensive finite element modelling was completed to gain understanding of the concentrations and locations of hydrogen in pressurized line pipe with respect to surface corrosion pits, and the effect of changes in stresses and geometry on the equilibrium hydrogen concentration. A hypothetical material stress-strain model, simulating the effects of hydrogen-enhanced localized plasticity, was used to investigate the possible role of hydrogen-enhanced plasticity in crack initiation. Throughout the modelling work, two distinct hydrogen trapping models were used and compared. The following is a summary of conclusions made during the course of this research project:

1. Samples of X-52 in C2 solution exhibited a slightly higher average room temperature creep strain than similar samples tested in air. The scatter between replicate test results is much larger than the difference in averages between the tests in air and the tests in C2. No firm conclusion

can be made about the effect of elevated hydrogen contents on the room temperature creep behaviour of this steel.

2. Considerable scatter in the hydrogen concentrations measured using the LECO RH-402 diminishes the precision and reliability of these results. Although the results include large scatter, the measured values are in agreement with other published experimental results.
3. Compared to samples in air, X-52 samples exposed to C2 solution have an increased equilibrium hydrogen concentration. The average hydrogen concentration for all samples soaked in C2 before testing was 5.75 ppm (2.67×10^{25} H atoms/m^3), compared to 0.57 ppm (2.65×10^{24} H atoms/m^3) for the samples stored in air.
4. During roughly twenty minutes of exposure to laboratory air, the large majority of hydrogen in steel samples that had been previously exposed to C2 solution can escape from the samples.
5. The addition of a recombination poison and the imposition of a cathodic potential to samples exposed to C2 solution increases the hydrogen content of the samples in comparison to samples in C2 solution without poison or imposed potential. The average hydrogen content for samples in C2 solution was 4.6 ppm (2.14×10^{25} H atoms/m^3) and samples in C2 solution with 250 ppm As_2O_3 and -1100 mV SCE imposed potential had an average hydrogen concentration of 7.0 ppm (3.25×10^{25} H atoms/m^3).
6. Based on numerous measurements of unstressed interstitial hydrogen concentrations in X-52 in near neutral pH environments reported in the literature, a reasonable but conservative estimate of this value is 3.0×10^{23} H atoms/m^3 (0.065 ppm).
7. In the material surrounding a corrosion pit on the surface of a pressurized pipe, hydrogen is present in both irreversible traps and interstitial lattice positions. For realistic estimates of pipe temperatures, stress levels and initial hydrogen concentrations, the hydrogen traps have a fractional occupancy close to one.

8. Existing hydrogen concentration modelling work has used trap densities measured in permeation tests of pure iron. These trap densities are a function of plastic strain, and range from 8.5×10^{20} traps/m^3 to 1.7×10^{23} traps/m^3. Similar permeation measurements conducted on X-52 pipeline steel measured trap densities between 2.3×10^{25} and 1.0×10^{26} traps/m^3.
9. The lower trap densities in pure iron cause the interstitial lattice sites to be the dominant location for hydrogen. In this case, the hydrogen concentration profile is determined by the hydrostatic stress in the material. With the higher trap densities associated with carbide interface trapping in pipeline steels, the trapped hydrogen is the dominant component of the total hydrogen concentration. In this case, on a macroscopic scale, the hydrogen concentration is equal everywhere in the material and is not influenced by stress or strain.
10. The higher trap densities in pipeline steel are understood to be due to trapping at the interfaces between ferrite and cementite phases. Hydrogen concentrations at these interfaces will be much higher than in the bulk ferrite material. The hydrogen concentration in the primary ferrite regions is understood to be dependent primarily upon hydrostatic stress as it is in pure iron.
11. NNpHSCC propagates through ferrite grains instead of only following the carbide interfaces. This disagreement between the locations of high hydrogen concentration in the X-52 microstructure and the experimentally observed cracking behaviour suggests that cracking propensity in pipeline steels cannot be directly linked to total hydrogen concentration and that hydrogen may play different roles in the stress corrosion cracking of pearlite and primary ferrite regions.
12. Biaxial loading in a pipe causes higher hydrostatic stresses near a surface flaw. If lattice hydrogen is important to the NNpHSCC process, a pipe with both hoop and axial stress will be more susceptible to cracking than a pipe with only hoop stress.

13. Numerical relationships with a good quality of fit were found to relate the maximum stress and strain conditions around a uniaxially loaded two-dimensional notch to the depth and tip radius of the notch.
14. A hypothetical hydrogen-dependent material property model was applied to finite element models of pits. The hydrogen induced property degradation in these models was much more severe than is realistic, and caused increases in total strain by up to 30% of the maximum strain value without HELP, but was not sufficient to create localized plastic strains indicative of crack initiation by highly localized ductile rupture as was hypothesized.
15. The difference in the effect of the HELP model on the smooth hemispherical pit and the hemispherical pit with base dissolution suggests that fairly severe pit geometry is needed in order for HELP to have an effect on the surrounding stress and strain conditions that would be significant in terms of critical crack initiation conditions.
16. Multiplication of dislocation traps in a pure iron trapping model by a factor of thirty to represent dislocation build-up by cyclic loading fails to significantly increase the total hydrogen concentration.
17. Three dimensional modelling is necessary in the use of finite element analysis to investigate crack initiation from surface pits. Comparison of two dimensional and three dimensional models of a hemispherical pit with uniaxial loading demonstrated that the two dimensional model does not provide realistic constraints, and represents a groove instead of a pit.

8.2. Suggestions for Future Work

8.2.1. Localized Hydrogen Dependent Stress-Strain Behaviour

Many tests have been done to understand the effect of hydrogen on the mechanical properties of steel. Slow strain rate tests, punch tests and tensile tests are some of the common tests used A premise of the HELP model is that hydrogen acts to allow significant plasticity in only a very limited volume of material and that this material fails by ductile rupture which then proceeds to

quasicleavage fracture further from the initiation site. Quantitative data relating hydrogen concentrations to changes in local material properties is needed. Further research into the role of hydrogen in promoting material degradation for the near-neutral pH SCC system would allow a better understanding of the role played by hydrogen in NNpHSCC.

8.2.2. Pipeline Steel Trap Densities

Available data on the trap densities in pipeline steels is limited. The trap densities used in the present research were taken from the results of Parkins (1998B), but in this work, the more traditional method of determining trap densities from successive permeation runs was unsuccessful and instead, the N_T value was calculated from C_L^o. More work to confirm the reported trap densities would provide valuable information about the hydrogen in pipeline steels. Future work should also investigate the effect of variables such as pearlite coarseness, grain size and plastic strain on trap density. This work could be done using permeation testing, hot extraction hydrogen content determination or other methods.

The nature of the traps in pipeline steel also requires further research. The present understanding of the traps as carbide interface traps poses a problem in understanding how hydrogen can play an important role in a cracking phenomenon that proceed primarily through ferrite grains.

8.2.3. 3D Modelling with Systematic Variations in Pit Geometry

To improve our understanding of the effect of corrosion pit geometry on the local stress and strain conditions on the surface of a pressurized pipe, it would be worthwhile to carry out finite element modelling in three dimensions, similar to that in the present research, using axisymmetric pits with a variety of depths and radii.

9. REFERENCES

D.P. Abraham and C.J. Altstetter, *Effect of Hydrogen on Yield and Flow Stress of an Austenitic Stainless Steel*, Metallurgical and Materials Transactions **26A**, pp. 2849-2858, (1995).

American Petroleum Institute, *Specification for Line Pipe*, API Specification 5L, 43rd Ed, March 2004

M.J. Anderson, *Finite Element and Analytical Modelling of Microstructural and Textural Anisotropy of Zr-2.5%Nb Nuclear Reactor Pressure Tube Material*, M.Sc. thesis, University of Alberta, 1996.

B. Arrigoni and E. Sinigaglia, *Transverse Stress Corrosion Cracking in a Landslide Area*, Proceedings of the 11th Biennial PRCI-EPRG Joint Technical Meeting, pp. 10-1 – 10-10, (1997).

Michael Baker Jr., Inc., OPS TTO8 – *Stress Corrosion Cracking Study*, January, 2005.

C.P. Beachem, "New Model for Hydrogen-Assisted Cracking (Hydrogen "Embrittlement")", *Metallurgical Transactions A*, Vol. 3, pp. 437-451, (1972).

J.A. Beavers, N. G. Thompson, and K. E. W. Coulson. *Effects of Surface Preparation and Coatings on SCC Susceptibility of Line Pipe: Phase 1—Laboratory Studies*. CORROSION/1993, Paper No. 93597. (1993A).

J.A. Beavers, N. G. Thompson, and K. E. W. Coulson. *Effects of Surface Preparation and Coatings on SCC Susceptibility of Line Pipe: Phase 2—Field Studies*. Proceedings of the12th International Conference on Offshore Mechanics and Arctic Engineering, (1993B).

J.A. Beavers, E.L. Hagerdorn, *Low-pH SCC: Mechanical Effects on Crack Propagation*, Pipeline Research Committee Report R207-01, PRC International, , (1996A).

J.A. Beavers and E.L. Hagerdon, *Near-Neutral pH SCC: Mechanical Effects on Crack Propagation*, Ninth Symposium on Pipeline Research, A.G.A. Cat. No. L51746 Paper 24 (1996B).

J.A. Beavers and B.A. Harle, *Mechanisms of High pH and Near-Neutral pH SCC of Underground Pipes*, 1996 *International Pipeline Conference*, Vol. 1, pp. 555-564, ASME New York, NY, 1996.

J.A. Beavers, C.E. Jaske, *Near-Neutral pH SCC in Pipelines: Effects of Pressure Fluctuations on Crack Propagation*, Corrosion/98, NACE Conference, Paper 257 (1998).

J.A. Beavers C.L. Durr and S.S. Shademan, *Mechanistic studies of near-neutral pH SCC on underground pipelines*, Materials for Resource Recovery and Transport, Edited by L. Collins, Metallurgical Society of CIM, 51-69 (1998).

J.A. Beavers and C.E. Jaske, *SCC of Underground Pipelines: A History of the Development of Test Techniques*, Corrosion/99, NACE Conference, Paper No. 142 (1999).

J.A. Beavers and C.E. Jaske, *Effect of Pressure Fluctuations on SCC Propagation*, Final Report to PRCI Contract PR-186-9706, Catalogue No. L51872, PRCI, Arlington, Virginia 2002.

J.A. Beavers, J.T. Johnson and R.L. Sutherby, *Materials Factors Influencing the Initiation of Near-Neutral pH SCC on Underground Pipelines, 2000 International Pipeline Conference*, Vol. 2, pp. 979-988, New York, NY, ASME, 2000.

J.A. Beavers, K.C. Garrity, *100 mV Polarization Criterion and External SCC of Underground Pipelines,* Corrosion/2001, NACE Conference, Paper No. 01592, (2001).

J.A. Beavers, C.L. Durr, B.S. Delanty, D.M. Owen and R.L. Sutherby, *Near Neutral pH SCC: Crack Propagation in Susceptible Soil Environments*, Corrosion 2001, NACE Conference, Paper 01217 (2001).

J.A. Beavers, R.G. Worthingham, *The Influence of Soil Chemistry on SCC of Underground Pipelines*, 2002 International Pipeline Conference, Paper No. IPC2002-27146, ASME, (2002).

J.A. Beavers, C.L. Durr and K.C. Garrity, *The Influence of Soil Chemistry on SCC of Pipelines and the Applicability of the 100 mV Polarization Criterion*, Corrosion 2002, NACE Conference, Paper No. 02426 (2002).

J.A. Beavers, *Near Neutral pH SCC: Dormancy & Re-Initiation of Stress Corrosion Cracks*, Report for Gas Research Institute, Report R1025-01R, Contract GRI-7045, (2004).

J. Been, M. Elboujdaini, R.W. Revie, and G. de Silveira, *Fundamental Studies in Crack Initiation and Early Crack Growth and Implications for Pipeline Operators*, Final report to Fraser King, NRTC. 2001.

J. Been, F. King, L. Yang, W. Chen, R. Sutherby and R. Worthingham, *Environmental effects on near-neutral pH SCC*, NACE Northern Area Conference, (2003).

J. Been, H. Lu, F. King, T. Jack, and R. Sutherby, *The role of hydrogen in EAC of pipeline steels in near-neutral pH environments*, EICM 2, Banff, AB, Canada, (2004).

H.K. Birnbaum, *Hydrogen effects on deformation - Relation between dislocation behavior and the macroscopic stress-strain behavior*, Scripta Metallurgica et Materialia **31(2)**, pp. 149-153, (1994).

H.K. Birnbaum and P. Sofronis, *Hydrogen-enhanced localized plasticity – a mechanism for hydrogen-related fracture*, Materials Science and Engineering **A176**, pp. 191-202, (1994).

W. Bouaeshi, S. Ironside, R. Eadie, "Research and Cracking Implications from an Assessment of Two Variants of Near-Neutral pH Crack Colonies in Liquid Pipelines", to be published

M.P.H. Brongers, J.A. Beavers, C.E. Jaske, and B.S. Delanty. *Effect of Hydrostatic Testing on Ductile Tearing of X-65 Line Pipe Steel with Stress Corrosion Cracks*. Corrosion 2000, NACE Conference, Paper No. 00355 (2000).

CEPA, *CEPA Stress Corrosion Cracking Database: Second Trending Report*, (2000).

W. Chen, M. Wilmott, T. Jack, "Hydrogen Permeation and Surface Deterioration of Pipeline Steel Exposed to Netural pH SCC Environment", NOVA Chemicals Report #01311, 1999

W. Chen, S.H. Wang, F. King, T.R. Jack, M.J. Wilmott, *Hydrogen Permeation Behaviour of X-70 Pipeline Steel in a Near-Neutral pH Soil Environment*, 2000 International Pipeline Conference, Vol. 2, pp. 953-960, ASME, (2000).

W. Chen, L. Yang, R. Eadie, *Low temperature Creep Near the Long Seam Weld in a X-65 Line Pipe Steel Under Static and Cyclic Loading Conditions and Its Effect on Near-Neutral pH Stress Corrosion Cracking and/or Corrosion Fatigue at the Toe of the Weld*, NOVA Chemicals Report No. 01560, (2001).

W. Chen and S.H. Wang, *Room Temperature Creep Behaviour of Pipeline Steels and Its Influence on Stress Corrosion Cracking*, 2002 International Pipeline Conference, Paper 27273, ASME, (2002).

W. Chen, F. King, T.R. Jack and W.J. Wilmott, *Environmental Aspects of Near-Neutral pH Stress Corrosion Cracking of Pipeline Steels*, Met. & Mat. Trans, **33A**, pp. 1429-1436 (2002A).

W. Chen, F. King, and E. Vokes, *Characteristics of Near-Neutral pH Stress Corrosion Cracks in an X-65 Pipeline*, Corrosion, **58**, pp. 267-275 (2002B).

W. Chen, S.H. Wang, R. Chu, F. King, T.R. Jack, and R.R. Fessler, *Effect of Pre-Cyclic Loading on SCC Initiation in an X-65 Pipeline Steel Exposed to Near-Neutral pH Soil Environment, Metall and Mater. Trans.*, **34A**: pp. 2601-2607 (2003).

W. Chen, R. Sutherby, *Environmental Effect of Crack Growth Rate of Pipeline Steel in Near-Neutral pH Soil Environments*, 2004 International Pipeline Conference, Paper IPC04-0449 (2004).

W. Chen, R.L. Eadie, R.L. Sutherby, *Environmental Effects on Near-Neutral pH Stress Corrosion Cracking in Pipelines*. 2nd International Conference on Environment-Induced Cracking of Metals (EICM-2), (2004).

W. Chen, W. Zheng, *Progress in understanding of pipeline SCC: initiation and propagation*, Symposium of Pipelines for the 21st Century, Calgary, Canada, August 21-24, (2005).

R.Chu, W. Chen, S.H. Wang, F. King, T.R. Jack, and R.R. Fessler, *Microstructure Dependence of SCC Initiation in X-65 Pipeline Steel Exposed to a Near-Neutral pH Soil Environment*, Corrosion **60(3)**, pp. 275-283, 2003.

D. Delafosse, T. Magnin, *Hydrogen induced plasticity in stress corrosion cracking of engineering systems*, Engineering Fracture Mechanics, Vol. 68, 2001, pp. 693-729

B. Delanty, J. O'Beirne, *Major Field Study Compares Pipeline SCC with Coatings*, Oil and Gas Journal, June 1992, pp. 39-44 (1992).

B.S. Delanty, and J.E. Marr. Stress Corrosion Cracking Severity Rating Model. In *Proceedings from the International Conference on Pipeline Reliability*. CANMET. 1992.

R.L. Eadie, L.W. Hunt, R.L. Sutherby, G. Roy, G. Shen, J. Luo, W. Chen, T.C. Hamré, F. King and T. Jack; *Long Seam Welds in Gas and Liquids Pipelines and Near-Neutral pH Stress Corrosion Cracking and Corrosion Fatigue*, 2002 International Pipeline Conference, Paper 27118, (2002).

R.L. Eadie, G. Shen, J. Been and R.L. Sutherby, *Stress at Pits and Long Seam Welds and Their Contribution to Stress Corrosion Cracking Especially Near-Neutral pH SCC*, to be published. 2005A.

R.L. Eadie, W. Chen, J. Luo, M. Elboujdaini. *Near-Neutral pH Stress Corrosion Cracking in Steel Pipelines.* 2005B.

R.L. Eadie, K.E. Szklarz, and R.L. Sutherby, *Corrosion Fatigue and Near-Neutral pH Stress Corrosion Cracking of Pipeline Steel and the Effect of Hydrogen Sulfide*, Corrosion **61(2)**, pp. 167-173, (2005C).

M. Elboujdaini, Y.Z. Wang, R.W. Revie, R.N. Parkins, and M.T. Shehata. *Stress Corrosion Crack Initiation Processes: Pitting and Microcrack Coalescence*, Corrosion/2000, NACE Conference, Paper No. 00379, (2000).

B. Fang, personal communication, October 30 (2006).

R.R. Fessler, and K. Krist, *Research Challenges Regarding Stress Corrosion Cracking of Pipelines*, Corrosion/2000, NACE Conference, Paper No. 00370, (2000).

R.G. Gangloff, R.G. Kelly, *Microbe-Enhanced Environmental Fatigue Crack Propagation in HY130 Steel*, Corrosion **50(5)**, pp. 345-354, (1994).

B. Gu, W.Z. Yu, J.L. Luo, X. Mao, *Transgranular Stress Corrosion Cracking of X-80 and X-52 Pipeline Steels in Dilute Aqueous Solution with Near-Neutral pH*, Corrosion **55(3)**, pp. 312-318, (1999A).

B. Gu, J. Luo and X. Mao, *Hydrogen-Facilitated Anodic Dissolution-Type Stress Corrosion Cracking of Pipeline Steels in Near-Neutral pH Solution*, Corrosion, **55(1)**, pp. 96 – 106, (1999B).

B.A. Harle, J.A. Beavers, C.E. Jaske, *Mechanical and Metallurgical Effects on Low pH Stress Corrosion Cracking of Natural Gas Pipelines*, Corrosion/95, Paper No. 646, (1995).

D. He, *Effect of surface conditions on electrochemical and mechanical properties of pipeline steels in near-neutral pH environment*, M.Sc. thesis, University of Alberta, 2002.

D-X. He, W. Chen, J-L Luo, *Effect of Cathodic Potential on Hydrogen Content in a Pipeline Steel Exposed to NS4 Near-Neutral pH Soil Solution*, Corrosion, **60(8)**, pp 778-786, (2004).

J.P. Hirth, *Effects of Hydrogen on the Properties of Iron and Steel*, Met. Trans. **11A**, pp. 861-890, (1980).

T.R. Jack, M.J. Wilmott, W. Chen, *Evaluation of SCC Susceptibility of X-70 Steel in Contact with Various Soil Solutions at Near Neutral pH: Comparison of Laboratory Predictions with Field Conditions*, EPRG/PRCI 12th Biennial Joint Tech Mtg. Netherlands, Paper 10, (1999).

T.R. Jack, B. Erno, K.Krist and R.R. Fessler, *Generation of near neutral pH and high pH SCC environments on buried pipelines*, Corrosion/2000, NACE Conference, Paper No. 00362, (2000).

H.H. Johnson and R.W. Lin, *Hydrogen deuterium trapping in iron*, Hydrogen Effects in Metal, Ed. I.M. Bernstein, A.W. Thompson, Metallurgical Society of AIME, pp. 3-23, (1981).

J. T. Johnson, C.L. Durr, J.A. Beavers, and B.S. Delanty, *Effects of O_2 and CO_2 on Near-Neutral pH Stress Corrosion Crack Propagation*, Corrosion/2000, NACE Conference, Paper No. 00356, (2000).

R.H. Jones, R.E. Ricker, *Mechanisms of Stress-Corrosion Cracking*, from "Stress-Corrosion Cracking", ASM International, (1992).

D.A. Jones, *Localized Surface Plasticity During Stress Corrosion Cracking*, Corrosion **52(5)**, pp. 356-362, (1996).

Y. Katz, N. Tymiak, W.W. Gerberich, *Nanomechanical probes as new approaches to hydrogen/deformation interaction studies*, Engineering Fracture Mechanics **68**, pp. 619-646, (2001).

H. Kimura and Matsui, *Mechanism of hydrogen-induced softening and hardening in iron*, Script Metallurgica **21**, pp. 319-324, (1987).

F. King, T. Jack, W. Chen, M. Wilmott, R. Fessler, K. Krist, *Mechanistic Studies of Initiation and Early Stage Crack Growth for Near-Neutral pH SCC on Pipelines*, Corrosion/2000, NACE Conference, Paper No. 00361, (2000).

F. King, T. Jack, W. Chen, S.-H. Wang, M. Elboujdaini, W. Revie, R. Worthingham, P. Dusek, *Development of a Predictive Model for the Initiation and Early-stage Growth of Near-neutral pH SCC of Pipeline Steels*, Corrosion/2001, NACE Conference, Paper No. 01214, (2001).

K. Kiuchi and R.B. McLellan, *The Solubility and Diffusivity of Hydrogen in Well-Annealed and Deformed Iron,* Acta Metallurgica **31(7)**, pp. 961-984, (1983).

Y. Kondo, *Prediction of Fatigue Crack Initiation Life Based on Pit Growth*, Corrosion **45(1)**, pp. 7-11, (1989).

A.J. Kumnick, H.H. Johnson, *Deep trapping states for hydrogen in deformed iron*, Acta Metall. **28**, pp. 33-39, (1980).

T. Kushida, K. Nose, H. Asahi, M. Kimura, Y. Yamane, S. Endo, H. Kawano, *Effects of Metallurgical Factors and Test Conditions on Near Neutral pH SCC of Pipeline Steels*, Corrosion/2001, NACE Conference, Paper No. 1213, (2001).

A.H.M. Krom, R.W.J. Koers and A. Bakker, *Hydrogen transport near a blunting crack tip*, Journal of the Mechanics and Physics of Solids **47**, pp. 971-992, (1999).

S.B. Lambert, R. Sutherby, *Fracture Mechanics Modeling of Stress Corrosion Crack Colonies*, International Conference on Pipeline Reliability, (1998).

S.B. Lambert, *Application of Superposition to TCPL Pressure Data*, Report to Tom Jack, NOVA Research and Technology Corporation, November 9, 2000

S.B. Lambert, J.A. Beavers, B. Delanty, R. Sutherby, and A. Plumtree, *Mechanical Factors Affecting Stress Corrosion Crack Growth Rates in Buried Pipelines*, 2000 International Pipeline Conference, Vol. 2, pp. 961-965, (2000A).

S.B. Lambert, A. Plumtree, R. Sutherby, *Modeling of Environmental Crack Growth in Pipeline Steel*, Corrosion/2000, NACE Conference, Paper No. 00364, (2000B).

LECO Corporation, *RH-402 Instruction Manual* (2000).

D. Le Friant, B. Bayle, C. Adam and T. Magnin, *Stress Corrosion Cracking of Pipelines Steels in Simulated Ground Water: From Mechanisms to a Ranking Test* Environmental Degradation of Engineering Materials, Vol. 1, pp. 168-173, 1999

B.N. Leis, *Initiation of SCC on Gas Transmission Pipelines in Related Cracking Environments*, Corrosion/96, NACE Conference, Paper No. 268, (1996).

B.N. Leis, J.A. Colwell, *Initiation of Stress-Corrosion Cracking on Gas Transmission Piping*, Effect of the Environment on the Initiation of Crack Growth, ASTM STP 1298, (1997).

K. Lian and E.I. Meletis, *Environment-Induced Deformation Localization During Transgranular Stress Corrosion Cracking*, Corrosion, **52(5)**, pp. 347-355 (1996).

Y. Liang, P. Sofronis, N. Aravas, *On the effect of hydrogen on plastic instabilities in metals*, Acta Materialia **51**, pp. 2717-2730, (2003).

Y. Liang, P. Sofronis, R.H. Dodds Jr., *Interaction of hydrogen with crack-tip plasticity: effects of constraint on void growth*, Materials Science and Engineering **A366**, pp. 397 – 411, (2004).

B.D. Lichter, H. Lu, W.F. Flanagan, Strain-enhanced dissolution: a model for Transgranular stress-corrosion cracking, Presented at the Second International Conference on Environment Sensitive Cracking and Corrosion Damage, pp. 271-278, 2001.

B.R. Linter, G.T. Burstein, *Reactions of pipeline steels in carbon dioxide solutions*, Corrosion Science **41**, pp. 117-139, (1999).

B. Lu, J. Luo, B. McCrady, *Near-Neutral pH SCC Initiation and Early Propagation of X70 Pipeline Steel*, 2002 International Pipeline Conference, Paper IPC2002-27234, (2002.)

S.P. Lynch, *Hydrogen embrittlement and liquid-metal embrittlement in nickel single crystals*, Scripta Metallurgica **13**, pp. 1051-1056, (1979).

S.P. Lynch, *A fractographic study of hydrogen-assisted cracking and liquid-metal embrittlement in nickel,* Journal of Materials Science **21**, pp. 692-704, (1986).

M. Meyer, M. Pontremoli, *Comparing of Laboratory Behaviour of Different Pipeline Steels Regarding Their Near-Neutral SCC-Susceptibility*, 13th Biennial PRCI-EPRG Joint Technical Meeting on Line Pipe Research, (2001).

M. Meyer, L. Scoppio, B. Rudd, E. Lo Piccolo, S. Matthews, J.-P. Jansen, *Near-Neutral pH SCC Resistance of Pipeline Steels: Effect of Some Material and Mechanical Parameters (EPRG-Report)*, 14th Biennial PRCI-EPRG Joint Technical Meeting on Line Pipe Research, (2003).

National Energy Board, *Stress Corrosion Cracking on Canadian Oil and Gas Pipelines. Report of the Inquiry*, Report No. MH-2-95, (1996).

R.A. Oriani, *The diffusion and trapping of hydrogen in steel*, Acta Metall.**18**, pp. 147-157, (1970).

K.F. Ott, Y.P. Surkov and V.G. Rybalko, *Some Features of the Operational Failure of Pipe Steels*, The Physics of Metals and Metallography **73(5)**, pp.523-526, (1992).

P. Paris and F. Erdogan, *A critical analysis of crack propagation laws*, Journal of Basic Engineering, Transactions of the American Society of Mechanical Engineers **85**, pp.528-534, (1963).

R. N. Parkins, *Electrochemical influences in fracture initiation*, Metals Technology **9**, (1982).

R.N. Parkins, R.R. Fessler, *Line Pipe Stress Corrosion Cracking – Mechanisms and Remedies*, Corrosion/86, NACE Conference, Paper No. 320, (1986).

R.N. Parkins, P.M. Singh, *Stress Corrosion Crack Coalescence*, Corrosion **46(6)**, pp. 485-499, (1990).

R.N. Parkins, *Stress Corrosion Cracking in Pipelines*, NACE Canada Region West Conference, (1994).

R.N. Parkins, W.K. Blanchard Jr., and B.S. Delanty, *Transgranular Stress Corrosion Cracking of High-Pressure Pipelines in Contact with Solutions of Near Neutral pH,* Corrosion **50(5)**, pp. 394-408, (1994).

R.N. Parkins, *Stress Corrosion Cracking of Pipelines – Its Control or Prevention*, Corrosion/96, NACE Conference, Paper 249 (1996 B).

R.N. Parkins and B.S. Delanty, *The Initiation and Early Stages of Growth of Stress Corrosion Cracks in Pipeline Steels Exposed to a Dilute, Near Neutral pH Solution*, Ninth Symposium on Pipeline Research, pp. 19-1 to 19-14, AGA Catalog No. L 51746 (1996).

R.N. Parkins, *The influence of hydrogen on crack growth in pipelines*, Materials for Resource Recovery and Transport, ed. L. Collins, Met. Soc. of CIM, pp. 35-49, (1998A).

R.N. Parkins, *Effects of Hydrogen on Low pH Stress Corrosion Crack Growth*, Final Report for PR-232-9704 (PRCI) (1998B)

R.N. Parkins, *A Review of Stress Corrosion Cracking of Pipelines in Contact with Near-Neutral (Low) pH Solutions*, Report for the Line Pipe Research Supervisory Committee of PRC International, (1999A).

R.N. Parkins, *The Involvement of Hydrogen in Low pH Stress Corrosion Cracking of Pipeline Steel*, 12th EPRG/PRCI Biennial Joint Technical Meeting in Line Pipe Research, May 1999, Groningen, the Netherlands. (1999B)

R.N. Parkins, *A Review of Stress Corrosion Cracking of High Pressure Gas Pipelines*, Corrosion/2000, NACE Conference, Paper No. 00363, (2000).

R.N. Parkins and J.A. Beavers, *Some Effects of Strain Rate on the Transgranular Stress Corrosion Cracking of Ferritic Steels in Dilute Near-Neutral pH Solutions*, Corrosion, **59(3)**, pp. 258-272 (2003).

L. Qiao, J.L. Luo and X. Mao, *J. Mater. Sci. Letters,* **16**, pp. 516-520 (1997).

L. Qiao, J.L. Luo and X. Mao, *Hydrogen Evolution and Enrichment Around*

Stress Corrosion Crack Tips of Pipeline Steels in Dilute Bicarbonate Solution, Corrosion, **54(2)**, pp. 115-120 (1998).

Z. Qin, B. Demko, J. Noel, D. Shoesmith, F. King, R. Worthingham, and K. Keith, *Localized Dissolution of Millscale-Covered Pipeline Steel Surfaces*, Corrosion, **60(10)**, pp 906-914, (2004).

R.B. Rebak, Z. Xia, R. Safruddin, Z. Szklarska-Smialowska, *Effect of Solution Composition and Electrochemical Potential on Stress Corrosion Cracking of X-52 Pipeline Steel*, Corrosion **52(5)**, pp. 396-405, (1996).

G. Roy, D. Kiff, R.W. Revie, *Residual Stresses in CANMET/Industry SCC Consortium Pipe Specimens*, Metals Technology Laboratories Report 93-33 (TR), protected business information, (1993).

A. J. Sedriks, *Stress Corrosion Cracking Test Methods*, Corrosion Testing Made Easy, Vol. 1, NACE, 1990

S.A. Shipilov, *Location of the fracture process zone for hydrogen-induced corrosion fatigue crack propagation*, Scripta Materialia 47, pp. 301-305, (2002).

V. Sizov, *SCC Initiation Study of X-52 Pipeline Steel and its Various Microstructures in Near Neutral pH Bicarbonate System*, M.Sc. thesis, University of Calgary, 1999.

Sofronis, P. and McMeeking, R.M., *Numerical Analysis of Hydrogen Transport Near a Blunting Crack,* Journal of the Mechanics and Physics of Solids **37(3)**, pp. 317 – 350, (1989).

Sofronis, P., Liang, Y., Aravas, N., *Hydrogen induced shear localization of the plastic flow in metals and alloys*, Eur. J. Mech. A/Solids **20**, pp. 857-872, (2001).

E. A. Steigerwald, F. W. Schaller, A.R. Troiano, Trans. Met. Soc. AIME **218**, pp. 832, (1960).

Y.P. Surkov, V.G. Rybalko, M.Y. Pavlov, T.S. Sycheva, *Corrosion Crack Initiation in Gas Pipelines*, The Physics of Metals and Metallography **78(1)**, pp.102-104, (1994).

R.L. Sutherby, *The CEPA Report on Circumferential Stress Corrosion Cracking*, 1998 International Pipeline Conference, Vol. 1, pp.493-503, ASME, (1998).

R. Sutherby, T. Jack, G. Van Boven, M. Wilmott, *CEPA Study on Characterization of Pipeline Pressure Fluctuations in Terms Relevant to Stress Corrosion Cracking*, 2000 International Pipeline Conference, Vol. 2, pp. 989-996, ASME, (2000).

T. Tabata and H.K. Birnbaum, *Direct observations of the effect of hydrogen on the behaviour of dislocations in iron*, Scripta Metallurgica **17**, pp. 947-950, (1983).

T. Tabata and H.K. Birnbaum, *Direct observations of hydrogen enhanced crack propagation in iron*, Scripta Metallurgica **18**, pp. 231-236, (1984).

J. Toribio, *Hydrogen-Plasticity Interactions in Pearlitic Steel: A Fractographic and Numerical Study*, Materials Science and Engineering **A219**, pp. 180-191, (1996).

A.R. Troiano, *Embrittlement by Hydrogen and Other Interstitials*, Metal Progress **77(2)**, pp. 112-117, (1960).

A. Turnbull, *Issues in Modelling of Environment Assisted Cracking*, Environmentally Assisted Cracking: Predictive Methods for Risk Assessment and Evaluation of Materials, Equipment and Structures, ASTM STP 1401, R.D. Kane, Ed., (2000).

W. Tyson, *Hydrogen in Metals*, Canadian Metallurgical Quarterly **18**, pp. 1-11, (1979).

N. Vadhwana, *Hydrogen behavior in three grades of pipeline steel*, M.Sc. thesis, University of Alberta, 2004.

G.J. Van Boven, *The Influence of Residual Stress on the Initiation and Propagation of Trans-granular Stress Corrosion Cracking in High Pressure Natural Gas Transmission Pipelines*, MSc thesis, University of Alberta, 2003

W.A. Van Der Sluys, M. Wilmott, K. Krist, *Effect of Sulfide on Stress Corrosion Crack Growth in Gas Transmission Pipe Lines*, 1998 International Pipeline Conference, 1998.

Y-Z. Wang, R.W. Revie and R.N. Parkins, *Mechanistic Aspects of Stress Corrosion Crack Initiation and Early Propagation*, Corrosion/99, NACE Conference, Paper 143 (1999).

S.H. Wang, W. Chen, T. Jack, F. King, R. Fessler, K. Krist, *Role of Prior Cyclic Loading in the Initiation of Stress-Corrosion Cracks on Pipeline Steels Exposed to Near-Neutral pH Environment*, 2000 International Pipeline Conference, Vol. 2, pp. 1005-1011, ASME, (2000).

S.H. Wang, W. Chen, *Room temperature creep deformation and its effect on yielding behaviour of a line pipe steel with discontinuous yielding*, Materials Science and Engineering **A301**, pp. 147-153, (2001).

S.-H. Wang, Y. Zhang, W. Chen, *Room temperature creep and strain-rate-dependent stress-strain behavior of pipeline steels*, Journal of Materials Science **36**, pp. 1931-1938, (2001).

S. H. Wang and W. Chen, *A study on the pre-cyclic-load-induced burst of creep deformation of a pipeline steel under subsequent static load*, Materials Science and Engineering **A325**, pp. 144-151, (2002).

Y-Z. Wang, R.W. Revie, M.T. Shehata and R.N. Parkins, *Early Stages of stress Corrosion Crack Development of X-65 Pipeline Steel in Near-Neutral pH Solution*, Materials for Resource Recovery and Transport, ed. L. Collins, Met. Soc. of CIM, pp. 71-93 (1998A).

Y-Z. Wang, R.W. Revie, M.T. Shehata, R.N. Parkins and K. Krist, *Initiation of Environment Induced Cracking in Pipeline Steel: Microstructural Correlations*, 1998 International Pipeline Conference, Vol. 1, pp. 529-542, ASME, (1998B).

J.M. West, *Some Quantitative Aspects of Hydrogen Embrittlement*, Hydrogen in Steel, The Institution of Metallurgists, Spring Residential Conference **19**, (1982).

M.J. Wilmott, T.R. Jack, J. Geerligs, R.L. Sutherby, *Soil probe measures several properties to predict corrosion*, Oil & Gas Journal **93(14)**, pp 54-58, (1995).

M.J. Wilmott, and D.A. Diakow, *Factors Influencing Stress Corrosion Cracking of Gas Transmission Pipelines: Detailed Studies Following a Pipeline Failure. Part 1: Environmental Considerations,* 1996 International Pipeline Conference, Vol. 1, pp. 507-524, ASME, (1996).

M.J. Wilmott, T.R. Jack, G. Van Boven, R. L. Sutherby, *Pipeline Stress Corrosion Cracking: Crack Growth Sensitivity Studies Under Simulated Field Conditions,* Corrosion/96, NACE Conference, Paper No. 242, (1996).

M. Wilmott and R.L. Sutherby, *The Role of Pressure and Pressure Fluctuations in the Growth of Stress Corrosion Cracks in Line Pipe Steels*, 1998 International Pipeline Conference, Vol. 1, pp. 409-422, ASME (1998).

Yu, W., *Stress Corrosion Cracking Behaviour of Pipeline Steels in Near-Neutral pH Solutions,* M.Sc. thesis, University of Calgary, 1997.

X.Y. Zhang, S.B. Lambert, R. Sutherby, and A. Plumtree, *Transgranular Stress Corrosion Cracking of X-60 Pipeline Steel in Simulated Ground Water*, Corrosion 55(3), pp.297-305, (1999).

B. Zhang, J. Fan, Y. Gogotsi, A. Chudnovsky, A. Teitsma, *Theoretical and Experimental Study of Stress Corrosion Cracking of Pipeline Steel in Near*

Neutral pH Environment, 2000 International Pipeline Conference, Vol. 2, pp. 1013 – 1020, ASME, (2000A).

B. Zhang, J. Fan, Y. Gogotsi, A. Chudnovsky, A. Teitsma, *Statistical and Thermodynamic Modeling of Stress Corrosion Cracking in Steel Gas Pipes,* Failures 2000 – Proceedings of the Fourth International Symposium on Risk, Economy and Safety, Failure Minimisation and Analysis, (2000B).

Z-Y. Zhang, *Corrosion and Hydrogen Permeation Characteristics of Pipeline Steel in Synthetic Near-neutral Ph Environments and Development of Cracking Environments*, M.Sc. thesis, University of Alberta, 2003.

W. Zheng, F.A. MacLeod, R.W. Revie, W.R. Tyson, G. Shen, D. Kiff, M. Skaff, E.-W. Wong, *Recent Progress in the Study of Transgranular SCC in Line Pipe Steels*, International Conference on Corrosion Deformation Interaction, Nice, France, (1996A).

W. Zheng, R.W. Revie, W.R. Tyson, G. Shen, F.A. MacLeod, D. Kiff, *Pipeline SCC in Near-Neutral pH Environment: Results of Full-Scale Tests*, Corrosion/96, NACE Conference, Paper 253, (1996B).

W. Zheng, R.W. Revie, F.A. MacLeod, O. Dinardo, D. Kiff and J. McKinnon, *Low pH SCC: Environmental Effects on Crack Propagation*, CANMET-MTL Report MTL 98-41, prepared for PRCI Project PR-230 9413 (1998)

W. Zheng, R. Sutherby, R.W. Revie, W.R. Tyson and G. Shen, *Stress Corrosion of Linepipe Steel in Near-Neutral pH Environment: A Review of the Effect of Stress*, in ASTM Special Technical Publication 1401, Environmentally Assisted Cracking - Predictive Methods for Risk Assessment and Evaluation of Materials, Equipment and Structures, R. Kane Ed., ASTM, (2000).

W. Zheng, *Stress Corrosion Cracking of Pipelines: an Overview of Key Factors*, Proc. of the Second International Conference on Environment Sensitive Cracking and Corrosion Damage, (2001).

APPENDIX A

Results of Hydrogen Content Determination Tests, including Blank Determination and Standard Calibration Runs

Test #	ID Code	H2 (ppm)	Weight (g)	Calib	Blank	Time	Peak
184	blank-1	1.03	5.0000	0.7369	0.00367	299	295
185	blank-1	0.206	5.0000	0.7369	0.00367	250	55
186	blank-1	0.094	5.0000	0.7369	0.00367	250	40
187	blank-1	0.147	5.0000	0.7369	0.00367	250	42
188	blank-1	0.206	5.0000	0.7369	0.00367	250	51
189	blank-1	0.074	5.0000	0.7369	0.00367	250	13
190	blank-1	0.07	5.0000	0.7369	0.00367	250	14
191	501-529	6.08	1.0010	0.7369	0.08280	1186	174
192	blank-1	-0.065	5.0000	0.7369	0.08280	250	12
193	blank-1	-0.064	5.0000	0.7369	0.08280	246	9
194	blank-1	-0.081	5.0000	0.7369	0.08280	250	5
195	501-529	5.47	1.0010	1.5222	0.01273	505	43
196	501-529	5.75	1.0010	1.5222	0.01273	250	157
197	501-529	4.98	1.0010	1.5222	0.01273	430	43
198	**X-52 air**	**0.628**	**0.9132**	**1.5222**	**0.01273**	**250**	**13**
199	**x-52 air**	**0.736**	**0.8302**	**1.5222**	**0.01273**	**250**	**31**
200	**x-52 air**	**0.346**	**0.9703**	**1.5222**	**0.01273**	**250**	**11**
201	**x-52 C2 pot**	**9.08**	**0.7627**	**1.5222**	**0.01273**	**250**	**233**
202	**std n2**	**5.5**	**1.0010**	**1.5222**	**0.01273**	**517**	**41**
203	**x-52 C2 pot**	**8.46**	**0.6324**	**1.5222**	**0.01273**	**250**	**273**
204	**x-52 C2 pot**	**3.41**	**1.2453**	**1.5222**	**0.01273**	**250**	**460**
205	**w x-52 C2pot**	**2.01**	**0.4222**	**1.5222**	**0.01273**	**250**	**53**
			New testing day				
206	blank-1	-0.013	5.0000	1.3051	0.01273	250	5
207	blank-1	0.014	5.0000	1.3051	0.01273	250	9
208	blank-1	0.025	5.0000	1.3051	0.01273	250	16
209	501-529	5.11	0.9982	1.3051	0.02267	504	43
210	501-529	5.61	1.0014	1.3051	0.02267	485	56
211	501-529	5.49	1.0014	1.3051	0.02267	527	49
212	**X-52 C2**	**10.2**	**1.2245**	**1.3051**	**0.02267**	**250**	**924**
213	**x-52 C2**	**2.45**	**0.7783**	**1.3051**	**0.02267**	**250**	**153**
214	**x-52 C2**	**6.22**	**0.5811**	**1.3051**	**0.02267**	**250**	**206**
215	**x-52 C2**	**0.31**	**0.4410**	**1.3051**	**0.02267**	**250**	**13**
			New testing day				
216	blank-1	-0.01	5.0000	1.1087	0.02267	250	20
217	blank-1	-0.045	5.0000	1.1087	0.02267	250	9
218	blank-1	-0.009	5.0000	1.1087	0.02267	250	7
219	501-529	4.61	1.0014	1.1087	-0.00282	475	51
220	501-529	5.44	1.0014	1.1087	-0.00282	572	53
221	501-529	6.15	0.9969	1.1087	-0.00282	670	55
222	**x-52 C2**	**11.1**		**1.1087**	**-0.00282**	**250**	**882**

223	**x-52 C2**	**4.87**		**1.1087**	**-0.00282**	**250**	**413**
224	**x-52 C2**	**4.83**		**1.1087**	**-0.00282**	**250**	**417**
225	**W x-52 C2**	**1.24**		**1.1087**	**-0.00282**	**250**	**70**
New testing day							
226	blank-1	0.087	5	1.3927	-0.00282	250	
227	blank-1	0.021	5	1.3927	-0.00282	250	12
228	blank-1	0.028	5	1.3927	-0.00282	250	5
229	501-529	5.34	1.0008	1.3927	-0.00282	524	41
230	501-529	5.15	1.0014	1.3927	0.03335	520	40
231	501-529	5.72	1.0014	1.3927	0.03335	588	48
232	**x-52 C2 gl**	**88.7**	**0.4826**	**1.3927**	**0.03335**	**250**	**1497**
233	**x-52 C2 gl**	**9.5**	**0.633**	**1.3927**	**0.03335**	**250**	**470**
234	**x-52 C2 gl**	**3.1**	**0.6434**	**1.3927**	**0.03335**	**250**	**116**
235	**x-52 C2 gr**	**52.3**	**2.0132**	**1.3927**	**0.03335**	**250**	**3764**
236	**x-52 C2 gr**	**8.6**	**1.6656**	**1.3927**	**0.03335**	**251**	**777**
237	**x-52 C2 gr**	**2.7**	**1.5722**	**1.3927**	**0.03335**	**250**	**269**

APPENDIX B

Controlled Pit Growth Method

Corrosion pits were grown on a small area of X-52 steel. The pits were created electrochemically using potential control in a dilute carbonate- bicarbonate solution.

A small piece of steel, approximately 1 cm long, was cut from the grip section of one of the cylindrical samples illustrated in Figure 21. This piece was mounted in epoxy so that the circular cross section with a diameter of 7 mm was exposed. The exposed surface of the steel was polished to a 600-grit finish.

A Gamry DC105 potentiostatic controller was used to carry out a potentiodynamic polarization scan of the test steel. A schematic of the setup is shown in Figure B-1. The solution used for the scan was 0.05 mol/L $NaHCO_3$ and 0.005 mol/L NaCl in deionized water. This same solution composition was also used to electrochemically grow pits on the sample. The sample of the test steel mounted in epoxy was used as the working electrode. A platinum wire immersed in the solution was used as the counter electrode, and a saturated calomel electrode (SCE) was used as the reference electrode. To reduce the solution resistance and the contamination of the testing solutions, a salt bridge was used at the tip of the reference electrode.

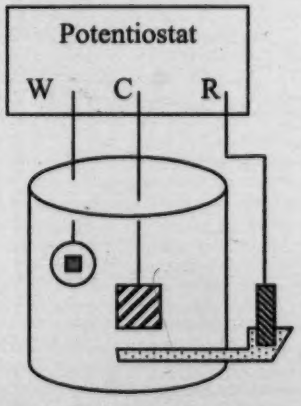

Figure B-1 - Schematic of potentiostatic controller setup for potentiodynamic polarization scan and electrochemically controlled pit growth

The purpose of the potentiodynamic polarization scan was to determine the pitting potential for the X-52 sample in the carbonate/bicarbonate solution. This information was needed in order to grow pits on the test sample using electrochemical methods.

Following the potentiodynamic polarization scan, one of the cylindrical steel samples was covered with tape and a plastic film, leaving only a 2 mm long band around the gauge length exposed. Acetone was used to clean the exposed surface, and then the sample was placed in the solution and hooked up as the working electrode for the pit growth process. The sample was left in solution for roughly 45 minutes to allow it to stabilize at its open circuit potential (OCP). The potential was considered to have stabilized if varied by less than 5 mV over half an hour. Once the sample had stabilized, a potential slightly more anodic than the pitting potential was applied to the sample. The corrosion current detected in the cell increased during this time, and after approximately two minutes, the imposed potential was reduced to be slightly more cathodic than the pitting potential. At this potential, initiation of new pits is suppressed while further growth of existing pits is possible. The decreasing corrosion current was monitored, and the pitting procedure was stopped and the sample removed from solution after twelve hours.

After the pit growth procedure, the entire surface was once again cleaned using both acetone and ultrasonic cleaning. The pits were observed and documented with micrographs.

Controlled Pit Growth Results

A potentiodynamic scan was conducted on a small polished cross-section of one of the X-52 cylindrical tensile samples. A scan rate of 1 mV/s was used, and the scan was started at a potential of -1100 mV SCE. The potential was increased to +300 mV and then decreased to -400 mV SCE, at which point the scan was completed.

The resulting potential versus current data is shown in Figure B-2. Using this information, the pitting and protection potentials were found, and are included on the figure below. The pitting and protection potentials for this sample of X-52 in a $NaHCO_3$/NaCl solution are 40 mV SCE and -234 mV SCE respectively. The open circuit potential is -795 mV SCE.

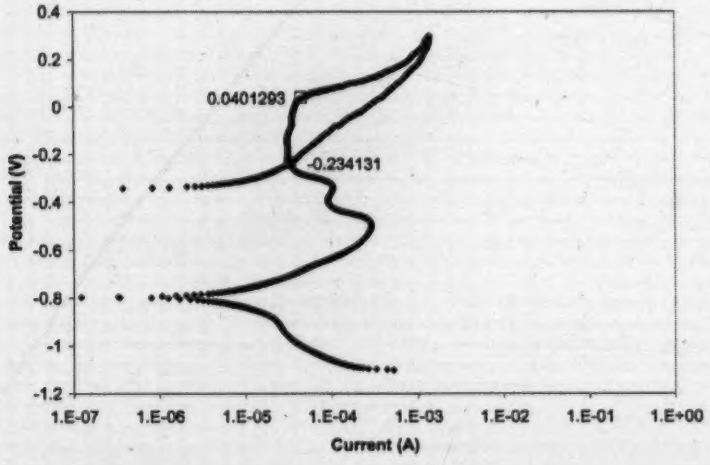

Figure B-2 - Potentiodynamic scan of X-52 in $NaHCO_3$ + NaCl solution

Using the identified pitting and protection potentials, pits were grown on a small exposed area of the gauge length of a cylindrical tensile sample. The data monitored and collected during the pitting process is plotted below. Figure B-3 shows how the cell potential decreased towards a stable open circuit potential. The data from the last half hour of the stabilization time is plotted as a heavier line, and the highest and lowest potentials recorded during this time are included on the plot. This sample was judged to be at a satisfactorily stable potential after a total stabilization time of 48 minutes.

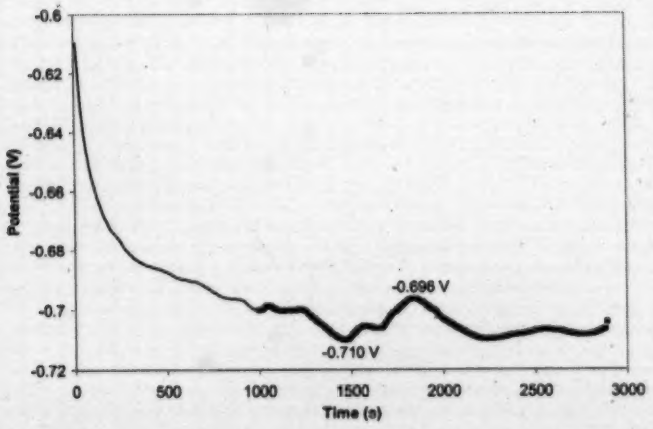

Figure B-3 - Stabilization of sample potential at open circuit before pitting procedure

After the time for stabilization, the sample was held at a potential of 45 mV SCE to cause pit initiation. During this time, the measured current in the electrochemical cell was observed to increase. After several minutes, when the current was no longer increasing rapidly, the potential was decreased to a passivation potential of -30 mV which was selected because it is between the pitting and protection potentials. At this potential, the initiation of new pits is suppressed, but the continued growth of existing pits is possible.

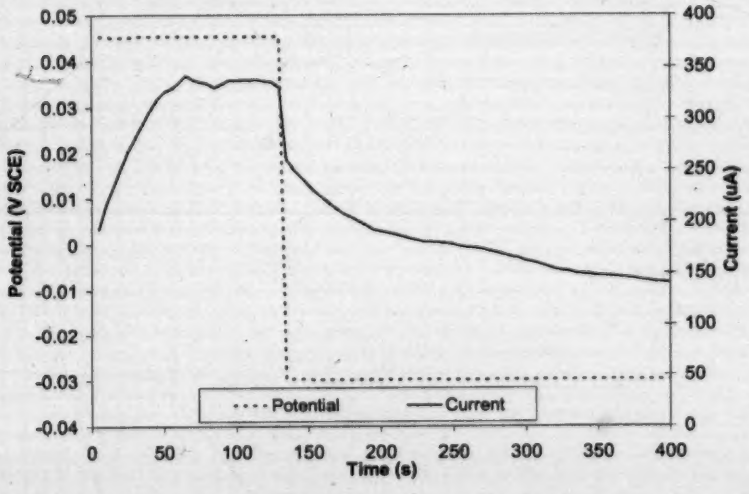

Figure B-4 - Imposed potential and measured current at the start of a pitting procedure

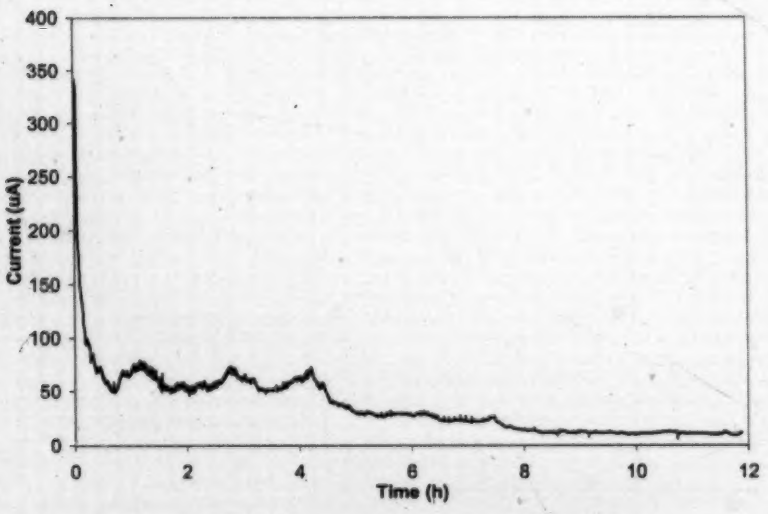

Figure B-5 - Measured current during a pitting procedure

Figures B-4 and B-5 both show the data recorded during the pitting procedure. Figure B-4 shows the data from the first several minutes of the procedure, while the potential was held at pitting potential and then switched to the passivation potential. The current recorded throughout the 12-hour test is shown in Figure B-5. The current can be seen to drop very quickly once the potential was changed to -30 mV SCE, and then to decay more slowly towards much lower values by the end of the pit growth period.

After the pitting procedure using the Gamry potentiostat was completed, the sample were removed from the cell, cleaned both ultrasonically and with solvents, and then examined using a microscope to document the size and shape of pits that were created on each sample.

Photographs of six representative pits created with this electrochemical pitting process are shown in Figure B-6. The vertically oriented lines on the sample surface in these images are due to the machining process on a lathe to make these tensile samples. These lines run circumferentially around the samples. It is

interesting to note that the pits have a tendency to be longer in the direction perpendicular to the machining scratches than in the parallel direction.

Both smooth pits and jagged, irregularly shaped pits were created by this pitting process. All six pictures included in Figure B-6 are of the same scale; the bar in the bottom right hand corner of the images shows 50 μm in length in comparison to the pit sizes.

Larger pits, requiring composites of multiple photographs in order to be captured were also observed during the microscopic examination of the pitted area. For example, one large pit was estimated to be 350 μm by 300 μm. Due to the curvature of the cylindrical samples and the shallow depth of focus allowed by the microscope at higher magnifications, the quality of the photographs of these larger pits is poor. For that reason, those photographs are not included here.

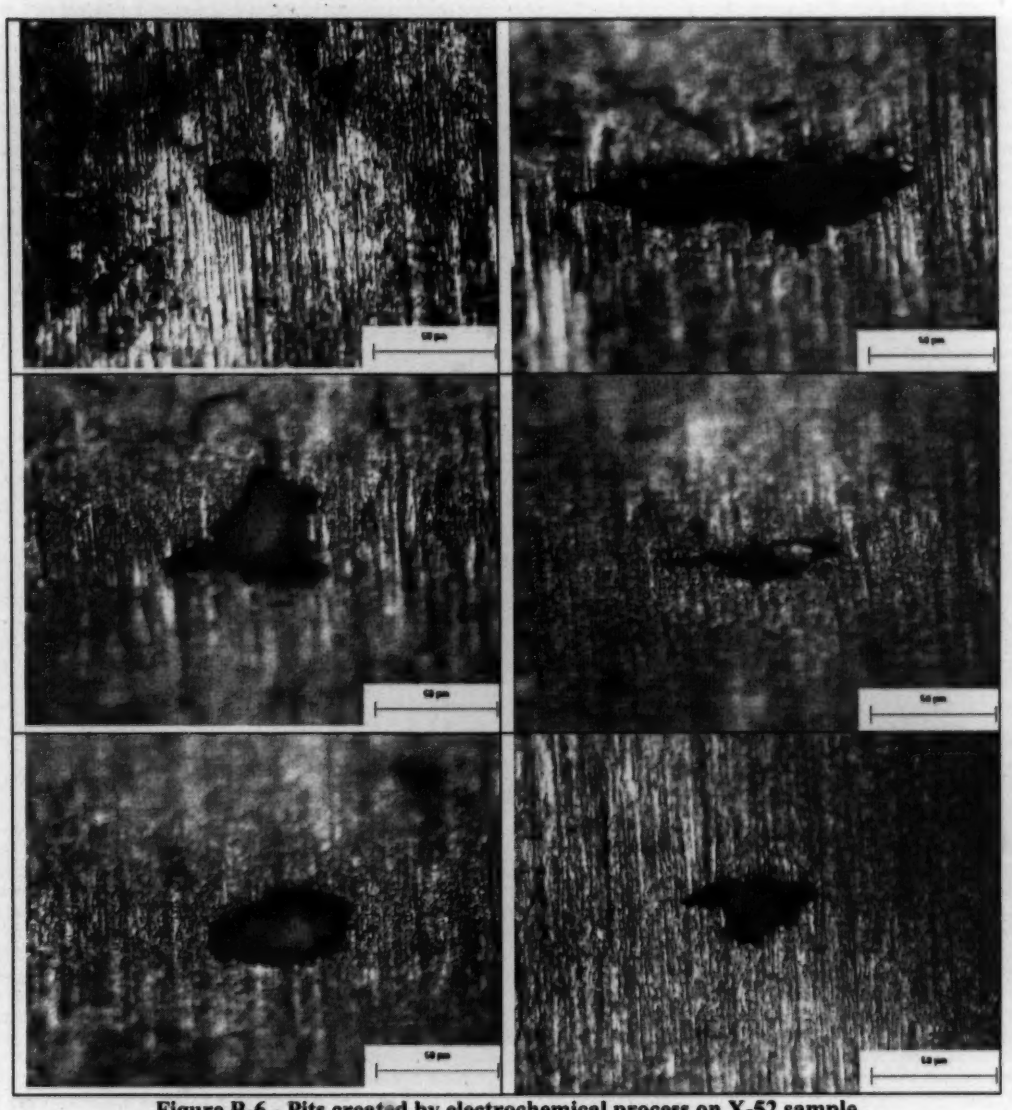

Figure B-6 - Pits created by electrochemical process on X-52 sample